Photonic Crystal Bragg Lasers: Design, Fabrication, and Characterization

Thesis by
Lin Zhu

In Partial Fulfillment of the Requirements
for the degree of
Doctor of Philosophy

CALIFORNIA INSTITUTE OF TECHNOLOGY
Pasadena, California

2008

(Defended May 15, 2008)

Acknowledgment

I am grateful for all the people who have helped and inspired me during my doctoral studies at Caltech. I would like to thank my advisor, Professor Amnon Yariv, for making my studies at Caltech possible. His keen physical intuition and consistent enthusiasm in research have inspired and motivated all his students, including me. I also owe my gratitude to Professor Axel Scherer, for welcoming me as a member of his group and for generously providing access to his laboratory facilities. I thank Professors Bruno Crosignani, Kerry Vahala, and Changhuei Yang for being part of my thesis committee.

I would like to thank everyone in our group. I am fortunate to have them as my labmates and have learned a lot from them. Especially, I want to thank Professor Joyce Poon, who helped me solve a lot of research problems in my project, and Dr. Will Green, who gave me the first lesson in fabrication and trained me in this field. I would like to express my appreciation to the post-docs and visiting scholars for their discussions and support: Dr. Philip Chak, T. R. Chen, Professor Yanyi Huang, Dr. Reg Lee, Professor Koby Scheuer, and Professor Yong Xu. Yangyi introduced me to the world of the optical experiment, while Philip showed me the deep understanding and precise thinking of the theory. I would like to thank all the students that I have worked with over the years: Dr. John Choi, Ali Ghaffari, Hsi-Chun Liu, Dr. Wei Liang, Dr. George Paloczi, James Raftery, Naresh Satyan, Christos Santis, Jacob Sendowski, and Xiankai Sun. John and Xiankai helped me a lot with the laser measurement setup and packaging. Also, I would like to acknowledge the staff in our group: Kevin Cooper, Irene Loera, and Connie Rodriguez.

Additionally, I want to thank the support of many outside the group. I would like to express my gratitude to Dr. Guy A. DeRose, who trained me in electron beam lithography.

I am grateful for Dr. Zhaoyu Zhang, who helped me a lot in dry etching process. At nLight Corporation, I am especially grateful to Dr. Paul Crump and Dr. Paul Leisher for their support of our collaboration.

I would also like to acknowledge the agencies that have provided support for this work: the IEEE Laser & Electro-Optics Society (LEOS Graduate Student Fellowship), the China Scholarship Council (China National Award for Outstanding Overseas Students), the Defense Advanced Research Projects Agency (SHEDS), and the Office of Naval Research.

Finally, I owe a great deal of thanks to my family, my parents and my sisters, on whose constant encouragement and love I have relied throughout my life.

Abstract

On-chip, single mode semiconductor lasers are usually fabricated using conventional distributed feedback (DFB) structures. Due to the limitation of index guiding in the transverse direction, the width of these lasers has to be less than a few microns. Meanwhile, the laser output power is limited by catastrophic optical damage (COD) at the facets and thus large optical cavities are necessary for high power semiconductor lasers. Therefore, high power, single mode applications are challenging, due to the conflicting requirements for large modal volume (to prevent COD by reducing optical power density) and narrow width (to obtain the single mode operation). Increasing the width of single mode semiconductor lasers is fundamentally important for obtaining high spectral and spatial optical power densities.

This thesis reports on achieving the single mode operation of large area, edge emitting semiconductor lasers, using the photonic crystal Bragg structure (two dimensional distributed feedback structure). Both theoretical and experimental results are presented. Two dimensional coupled mode approaches and transfer matrix methods are developed to analyze and design the photonic crystal Bragg structure. It is shown that the single mode lasing can be obtained by satisfying both the transverse and longitudinal Bragg conditions and a single lobe, diffraction limited far field can be obtained by optimizing the coupling coefficient of the photonic crystal.

Electrically pumped, large-area (100 μm x 500 μm), single mode semiconductor photonic crystal Bragg lasers are experimentally demonstrated in pulsed and continuous wave conditions with single lobe, diffraction limited far fields. Two dimensional lasing wavelength tuning is demonstrated, which proves that the lasing mode is truly defined by

the photonic crystal lattice. Furthermore, a wavelength tuning sensitivity about 80 times smaller than a conventional DFB laser is also achieved, allowing for more accurate control of the lasing wavelength.

Photonic crystal lasers based on effective index guiding are also studied. Single mode operation is achieved by combining the transverse confinement provided by an effective index guiding mechanism with the longitudinal mode selection provided by the Bragg reflection from the photonic crystal cladding. These devices represent an important first step toward using photonic crystals in a different way for the modal control of semiconductor lasers in planar optical circuits.

Contents

List of Figures

List of Tables

Chapter 1

Introduction

The invention of the semiconductor laser is considered to be a breakthrough that has revolutionized industry. Semiconductor lasers have a lot of applications in telecommunication, data storage, sensing, material processing, and medical science. Advances in device design concepts, crystal growth technologies, micro/nano fabrications and packing technologies have all contributed to the development of semiconductor lasers in the last half century. The performance of semiconductor lasers, such as thresholds, emission frequencies, linewidths, and beam qualities, is associated with the modal properties of the laser cavity [1–4]. Thus the modal control of the semiconductor laser has always been a key issue in developing new types of semiconductor lasers.

Waveguiding mechanism based on total internal reflection (TIR) is commonly used for the modal control of semiconductor lasers. For example, in a typical Fabry-Perot (FP) cavity laser, the lasing modes are guided by the epitaxially grown separate confinement heterostructure (SCH) in the vertical direction [5] and the buried waveguide structure in the transverse direction [6]. (For edge emitting lasers, we define the wafer growth direction as the vertical direction, the light emitting direction as the longitudinal direction, and the last direction as the transverse direction.) Through the appropriate design of the SCH and the buried waveguide structures, single vertical and transverse mode operation of a FP laser can be obtained. However, single longitudinal mode operation cannot be

obtained, since two cleaved facets in the longitudinal direction provide the feedback mechanism and thus support multiple longitudinal modes [2–4].

By using periodic Bragg gratings in the longitudinal direction, the single longitudinal mode operation of semiconductor lasers was demonstrated in the 1970s [7, 8]. These semiconductor lasers are generally referred as the distributed feedback (DFB) lasers. As shown in Fig. 1.1(a), the Bragg grating of a DFB laser is designed to only reflect a narrow band of wavelengths, so single longitudinal mode operation can be obtained. Combining with the single vertical and transverse mode distribution, we can realize the single mode operation of semiconductor lasers.

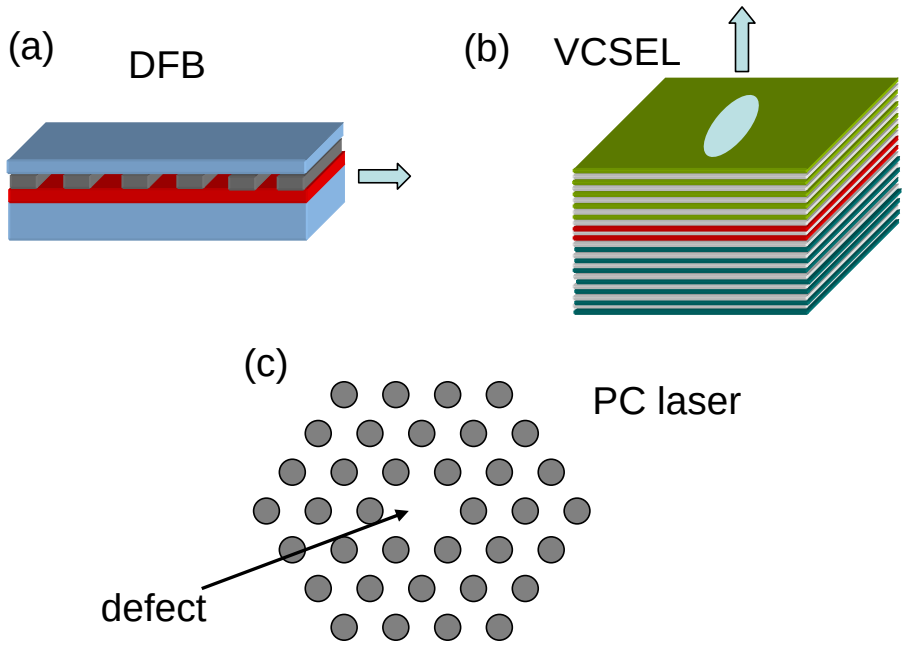

Figure 1.1: Schematic illustration of (a) a DFB laser, (b) a VCSEL laser, (c) a two-dimensional photonic crystal defect laser

Since then, Bragg reflections from periodic structures have been widely used for the laser cavity designs. As shown in Fig. 1.1(b), there are two Bragg gratings below and above the active region in a vertical cavity surface emitting laser (VCSEL) [9, 10]. These two Bragg reflectors are epitaxially grown to serve as high reflectivity mirrors. This high

reflectivity is important to compensate the loss associated with a short cavity in the vertical direction. As shown in Fig. 1.1(c), in a surface emitting photonic crystal defect laser [11], the in-plane confinement is fully provided by the Bragg reflections from the photonic crystal.

In contrast to the DFB and VCSEL lasers, the transverse Bragg resonance (TBR) laser is a type of the edge emitting semiconductor laser which includes a periodic Bragg grating in the transverse direction [12–14]. TBR structures use the Bragg reflection from the grating rather than total internal reflection to confine light in the transverse direction. In the vertical direction, light is still confined by the wafer epitaxial structure for the TBR lasers. In the same way that the DFB structure fixes the longitudinal wavevector, the transverse grating selects a single wavevector in the transverse direction. The TBR structure is very important for designing single mode, high power semiconductor lasers.

In the index-guided single mode DFB laser (using a ridge waveguide or a buried waveguide), the refractive index difference between the core and the cladding is usually around 1e-2 [3]. Thus, the transverse laser width has to be less than a few microns in order to obtain single transverse mode operation. Meanwhile, due to catastrophic optical damage (COD) at the end facets, the laser output power is limited by the device transverse size [15]. Ultimately, we need to increase the width of the semiconductor laser to obtain high power operation.

However, if we simply increase the laser width, we cannot maintain the single transverse mode operation. First, the refractive index difference between the core and the cladding needs to be very small to keep the single transverse mode operation if the laser width is large. The current injection will then change the refractive index profile due to the carrier distribution [2, 3]. In this way, the single transverse mode operation will not hold any more. Second, there are some spots with higher material gain along the facet if the laser width is large. This is because the material is not perfectly uniform. Since the waveguiding is very weak, these high gain spots will eventually become filaments above

the lasing threshold [16].

In contrast, the TBR waveguide can be designed to support only a single transverse mode regardless of the transverse width of the device [17]. This gives the TBR laser two attractive features for high power applications: good beam quality without filamentation, as defined by a single transverse mode, and a large emitting aperture for high power output. It is also feasible to design a single mode, broad-area, high power semiconductor laser by incorporating a longitudinal grating into a TBR waveguide. We define such a structure as the two dimensional TBR structure or the photonic crystal Bragg structure. In a photonic crystal Bragg laser, the longitudinal and transverse wavevectors of the lasing mode are both selected by the Bragg reflections from the photonic crystal. Thus the single mode operation can be achieved by the appropriate design of the photonic crystal and the lasing wavelength can be tuned by changing either the longitudinal or transverse lattice constant of the photonic crystal [18].

1.1 Distributed feedback structures

The DFB laser is the first example where the periodic structure is used for the modal control of semiconductor lasers. Here we briefly review the basic concepts of the DFB structure. The results will also help understand the TBR and photonic crystal Bragg structures discussed in the following chapters.

Figure 1.2 shows the schematic illustrations of a DFB laser and its longitudinal Bragg grating. For a typical DFB laser, the waveguiding mechanism is provided by the epitaxial structure in the vertical direction (y) and the buried waveguide structure in the transverse direction (x). The Bragg grating is along the longitudinal direction (z) and is usually placed inside the cladding layer away from the active region. This is because direct etching of the active layer can introduce defects and thus increase the nonradiative recombination rate, which leads to a high lasing threshold [3]. Since the grating only

interacts with part of the optical mode, the grating exact location and the corrugation depth are critical in determining the grating strength (effectiveness).

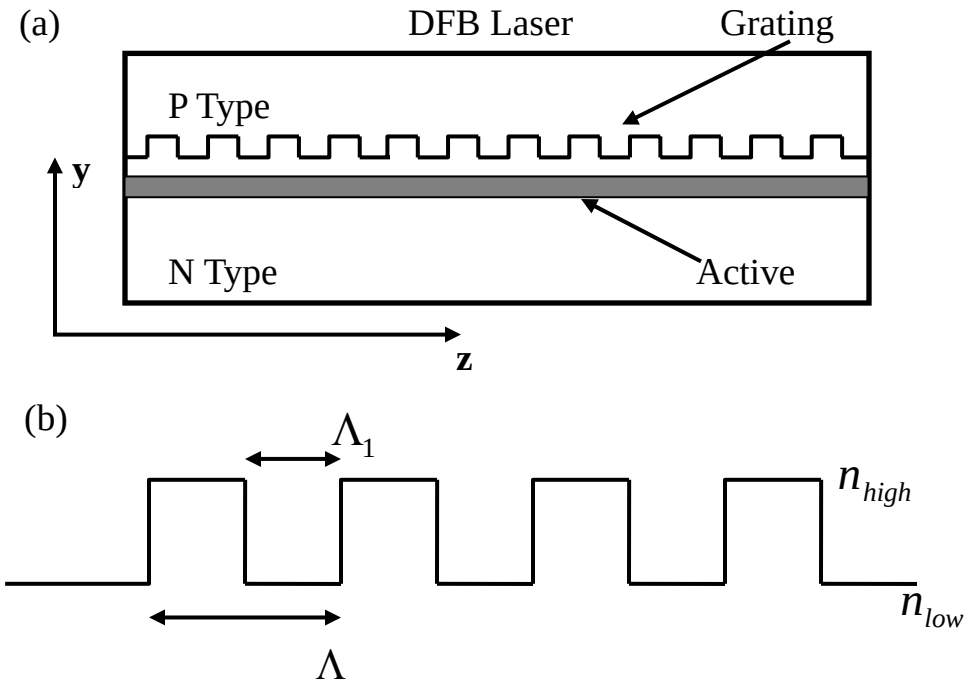

Figure 1.2: (a) Schematic illustration of a DFB semiconductor laser, (b) schematic illustration of the longitudinal Bragg grating

We usually use the parameter κ_l (the longitudinal grating coupling coefficient) to evaluate the grating strength. From the coupled mode analysis [3], we have

$$\kappa_l = \frac{k_0^2}{2\beta} \frac{\iint \Delta\varepsilon_m(x,y) U^2(x,y) dxdy}{\iint U^2(x,y) dxdy} \tag{1.1}$$

$$k_0 = 2\pi / \lambda \tag{1.2}$$

where λ is the wavelength, k_0 is the wavevector, β is the propagation constant (the longitudinal wavevector), $U(x,y)$ is the optical modal distribution without the grating, and $\Delta\varepsilon_m(x,y)$ is the m*th* order index perturbation of the grating. Given the wafer structure in the vertical direction and the waveguide structure in the transverse direction,

we can numerically solve for the optical modal distribution $U(x, y)$ and the effective index n_{eff} of the waveguide mode without the grating. Then we can calculate the propagation constant as

$$\beta = n_{eff} k_0 . \tag{1.3}$$

Appling the well-known Bragg condition, we can determine the grating period

$$\Lambda = m\pi / \beta . \tag{1.4}$$

Using the grating profile in Fig. 1.1(b), we have

$$\Delta\varepsilon_m(y) = (n_h^2 - n_l^2)\frac{\sin(\pi m \Lambda_1 / \Lambda)}{\pi m} \tag{1.5}$$

$$\kappa_l = \frac{k_0^2}{2\beta}(n_h^2 - n_l^2)\frac{\sin(\pi m \Lambda_1 / \Lambda)}{\pi m}\frac{\int_{grating} U^2(x, y)dxdy}{\iint U^2(x, y)dxdy} = \frac{k_0^2}{2\beta}(n_h^2 - n_l^2)\frac{\sin(\pi m \Lambda_1 / \Lambda)}{\pi m}\Gamma \tag{1.6}$$

$$\Gamma = \frac{\int_{grating} U^2(x, y)dxdy}{\iint U^2(x, y)dxdy} \tag{1.7}$$

where Λ is the grating period and Γ is the confinement factor. The confinement factor can be calculated from the optical modal distribution and it represents how much of the optical mode interacts with the grating.

In Fig. 1.3, we plot the index profile of a typical wafer design and the associated optical modal distribution in the vertical direction. The transverse direction is assumed to be uniform without any optical confinement. The peak of the modal profile is located at the quantum well region of the wafer. Due to the limitation of the fabrication, the corrugation depth of the grating is usually less than 50 nm. Thus the relative distance from the grating to the quantum well region has a strong impact on the confinement

factor, as shown in Fig. 1.3.

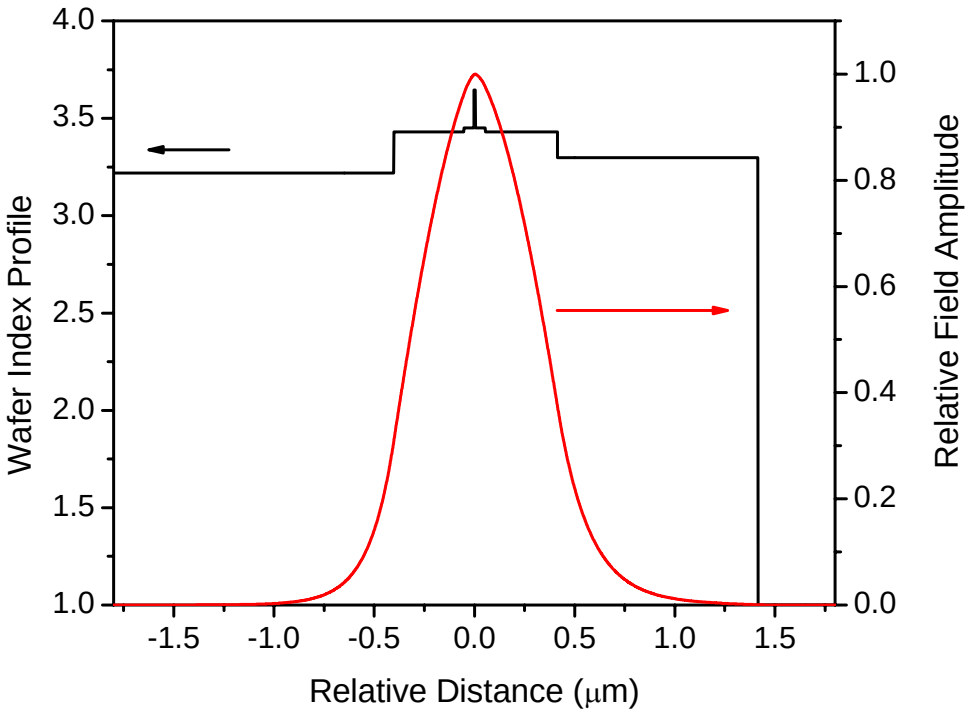

Figure 1.3: The index profile of a typical wafer design and the associated optical modal distribution in the vertical direction

The reflectance of a Bragg grating with the length L is given by [1]

$$R = \left| \frac{E_{in}}{E_{reflected}} \right|^2 = \frac{|\kappa|^2 \sinh^2(sL)}{s^2 \cosh^2(sL) + \Delta\beta^2 \sinh^2(sL)} \tag{1.8}$$

$$s = \sqrt{|\kappa|^2 - \Delta\beta^2} \tag{1.9}$$

$$\Delta\beta = \beta(\omega) - m\pi / \Lambda . \tag{1.10}$$

Maximum reflectance occurs at $\Delta\beta = 0$, where the reflectance is

$$R = \tanh^2(\kappa L) . \tag{1.11}$$

Figure 1.4 shows the simulated reflectance of a Bragg grating with the length of 500

μm. It is clear that the coupling coefficient has an impact on both the reflectance and the spectral bandwidth of the grating. It can also be approximately estimated that the grating bandwidth is equivalent to the coupling coefficient κ, since significant contradirectional coupling only occurs in the spectral regime where $-\kappa < \Delta\beta < \kappa$. Because the Bragg grating only reflects light in a narrow bandwidth, it can be used to select a single longitudinal mode of semiconductor lasers.

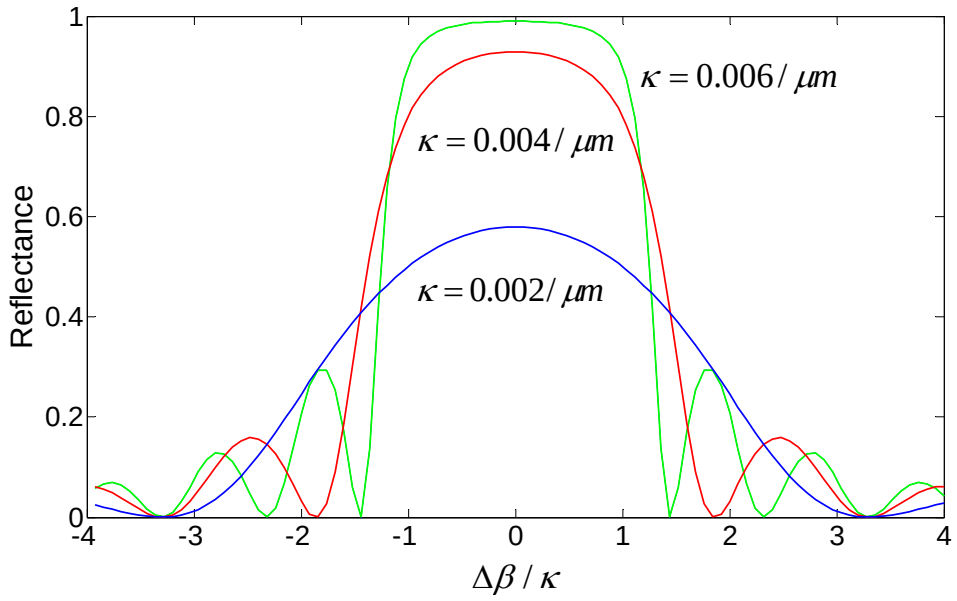

Figure 1.4: Simulated reflectance for a 500 μm long Bragg grating with different coupling coefficients

1.2 Transverse Bragg resonance structures

The concept of optical waveguiding by Bragg reflection has attracted a lot of attention due to the recent progress in photonic crystal fibers [19–21] and planar photonic crystal waveguides [13, 22]. The main applications focus on guiding light in a low-index region [23] or through a sharp waveguide bend [24]. As a generalization of these photonic crystal structures, the TBR waveguide was proposed and analyzed using the coupled mode theory [13]. In Ref. [13], the analysis was applied for the two dimensional periodic

structures but the coupling in the longitudinal direction was ignored for simplicity. In the following sections, we will start with a full coupled mode analysis of two dimensional periodic structures and then apply the results for the TBR waveguides.

1.2.1 Coupled mode analysis of two dimensional periodic structures

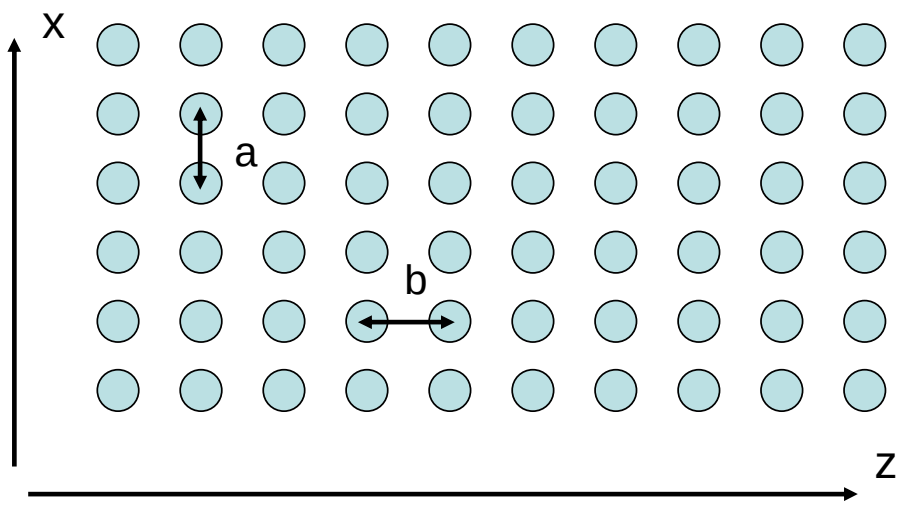

Figure 1.5: Schematic of the planar two dimensional periodic structures

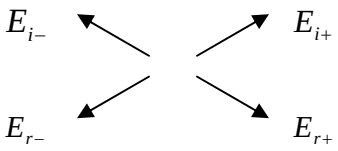

Figure 1.6: Schematic illustration of the four plane waves in the two dimensional periodic structures

Figure 1.5 shows the schematic of the planar two dimensional periodic structures. a is the transverse lattice constant and b is the longitudinal lattice constant. In the limit of small index perturbation, the electrical field satisfies the time-independent wave equation

[13]

$$\nabla^2 E + \varepsilon(x,y,z)k_0^2 E = 0 \tag{1.12}$$

$$\varepsilon(x,y,z) = \bar{\varepsilon}(x,y,z) + \Delta\varepsilon(x,y,z) \tag{1.13}$$

where $\bar{\varepsilon}(x,y,z)$ is the average value of ε and $\Delta\varepsilon(x,y,z)$ is the small index perturbation.

First, we consider the unperturbed situation with $\Delta\varepsilon = 0$. Eq. (1.12) is satisfied by either harmonic or plane wave solutions. We take the solution to be the form of four intersecting plane waves propagating at an equal angle relative to the z axis, as shown in Fig. 1.6

$$\begin{aligned} E(x,y,z) = U(y)[&E_{i+}\exp(-i(k_\perp x + \beta z)) + E_{r+}\exp(-i(-k_\perp x + \beta z)) + \\ &E_{i-}\exp(-i(k_\perp x - \beta z)) + E_{r-}\exp(-i(-k_\perp x - \beta z))] \end{aligned} \tag{1.14}$$

where $k_\perp$ is the transverse wavevector and β is the longitudinal wavevector. Then we substitute this solution form into the wave equation, and we have

$$\frac{d^2U}{dy^2} + (\bar{\varepsilon}(y)k_0^2 - k_\perp^2 - \beta^2)U = 0. \tag{1.15}$$

For a specific index distribution along the vertical direction y, which is determined by the wafer epitaxial layer structure, we can solve for the modal distribution U(y) and the effective index n_{eff}. We also have the dispersion relation

$$k_\perp^2 + \beta^2 = n_{eff}^2 k_0^2. \tag{1.16}$$

Now we consider the structure with the index perturbation. This problem deals with the four waves coupling into each other ($E_{i+}(x,z)$, $E_{r+}(x,z)$, $E_{i-}(x,z)$, and $E_{r-}(x,z)$), assuming the modal profile in the vertical direction U(y) is unaffected. We express the optical field in the medium as

$$E(x,y,z) = U(y)E(x,z) \tag{1.17}$$

$$\begin{aligned} E(x,z) &= E_{i+}(x,z)\exp(-i(k_\perp x + \beta z)) + E_{r+}(x,z)\exp(-i(-k_\perp x + \beta z)) + \\ &E_{i-}(x,z)\exp(-i(k_\perp x - \beta z)) + E_{r-}(x,z)\exp(-i(-k_\perp x - \beta z)). \end{aligned} \tag{1.18}$$

We also define

$$K_{i+} \equiv k_\perp \vec{x} + \beta \vec{z} \quad K_{r+} \equiv -k_\perp \vec{x} + \beta \vec{z} \quad K_{i-} \equiv k_\perp \vec{x} - \beta \vec{z} \quad K_{r-} \equiv -k_\perp \vec{x} - \beta \vec{z} \tag{1.19}$$

$$\begin{aligned} E(x,z) &= E_{i+}(x,z)\exp(-iK_{i+}\cdot\vec{r}) + E_{r+}(x,z)\exp(-iK_{r+}\cdot\vec{r}) + \\ &E_{i-}(x,z)\exp(-iK_{i-}\cdot\vec{r}) + E_{r-}(x,z)\exp(-iK_{r-}\cdot\vec{r}). \end{aligned} \tag{1.20}$$

$E_{i+}(x,z)$, $E_{r+}(x,z)$, $E_{i-}(x,z)$, and $E_{r-}(x,z)$ are all assumed to have slowly varying amplitude. We then put the field expression Eq. (1.20) into the wave equation, we have

$$\begin{aligned} &\frac{d^2U}{dy^2}E(x,z) + \bar{\varepsilon}(y)k_0^2UE(x,z) + \\ &U[(\frac{\partial^2 E_{i+}(x,z)}{\partial x^2} + (-2ik_\perp)\frac{\partial E_{i+}(x,z)}{\partial x} + (-ik_\perp)^2 E_{i+}(x,z))\exp(-iK_{i+}\cdot\vec{r}) + \\ &(\frac{\partial^2 E_{r+}(x,z)}{\partial x^2} + (2ik_\perp)\frac{\partial E_{r+}(x,z)}{\partial x} + (ik_\perp)^2 E_{r+}(x,z))\exp(-iK_{r+}\cdot\vec{r}) + \\ &(\frac{\partial^2 E_{i-}(x,z)}{\partial x^2} + (-2ik_\perp)\frac{\partial E_{i-}(x,z)}{\partial x} + (-ik_\perp)^2 E_{i-}(x,z))\exp(-iK_{i-}\cdot\vec{r}) + \\ &(\frac{\partial^2 E_{r-}(x,z)}{\partial x^2} + (2ik_\perp)\frac{\partial E_{r-}(x,z)}{\partial x} + (ik_\perp)^2 E_{r-}(x,z))\exp(-iK_{r-}\cdot\vec{r})] + \\ &U[(\frac{\partial^2 E_{i+}(x,z)}{\partial z^2} + (-2i\beta)\frac{\partial E_{i+}(x,z)}{\partial z} + (-i\beta)^2 E_{i+}(x,z))\exp(-iK_{i+}\cdot\vec{r}) + \\ &(\frac{\partial^2 E_{r+}(x,z)}{\partial z^2} + (-2i\beta)\frac{\partial E_{r+}(x,z)}{\partial z} + (-i\beta)^2 E_{r+}(x,z))\exp(-iK_{r+}\cdot\vec{r}) + \\ &(\frac{\partial^2 E_{i-}(x,z)}{\partial z^2} + (2i\beta)\frac{\partial E_{i-}(x,z)}{\partial z} + (i\beta)^2 E_{i-}(x,z))\exp(-iK_{i-}\cdot\vec{r}) + \\ &(\frac{\partial^2 E_{r-}(x,z)}{\partial z^2} + (2i\beta)\frac{\partial E_{r-}(x,z)}{\partial z} + (i\beta)^2 E_{r-}(x,z))\exp(-iK_{r-}\cdot\vec{r})] = -k_0^2\Delta\varepsilon(x,y,z)UE(x,z). \end{aligned} \tag{1.21}$$

Using the slowly varying amplitude assumption, we can ignore all the high order terms in

Eq. (1.21)

$$
\begin{aligned}
&[\frac{d^2U}{dy^2}+(\bar{\varepsilon}(y)k_0^2-k_\perp^2-\beta^2)U]E(x,z)+\\
&U[(-2ik_\perp)\frac{\partial E_{i+}(x,z)}{\partial x}\exp(-iK_{i+}\cdot\vec{r})+(2ik_\perp)\frac{\partial E_{r+}(x,z)}{\partial x}\exp(-iK_{r+}\cdot\vec{r})+\\
&(-2ik_\perp)\frac{\partial E_{i-}(x,z)}{\partial x}\exp(-iK_{i-}\cdot\vec{r})+(2ik_\perp)\frac{\partial E_{r-}(x,z)}{\partial x}\exp(-iK_{r-}\cdot\vec{r})]+\\
&U[(-2i\beta)\frac{\partial E_{i+}(x,z)}{\partial z}\exp(-iK_{i+}\cdot\vec{r})+(-2i\beta)\frac{\partial E_{r+}(x,z)}{\partial z}\exp(-iK_{r+}\cdot\vec{r})+\\
&(2i\beta)\frac{\partial E_{i-}(x,z)}{\partial z}\exp(-iK_{i-}\cdot\vec{r})+(2i\beta)\frac{\partial E_{r-}(x,z)}{\partial z}\exp(-iK_{r-}\cdot\vec{r})]=-k_0^2\Delta\varepsilon(x,y,z)UE(x,z).
\end{aligned}
\tag{1.22}
$$

Using Eq. (1.15), we can further simplify the above equation

$$
\begin{aligned}
&U[((-2ik_\perp)\frac{\partial E_{i+}(x,z)}{\partial x}+(-2i\beta)\frac{\partial E_{i+}(x,z)}{\partial z})\exp(-iK_{i+}\cdot\vec{r})+\\
&((2ik_\perp)\frac{\partial E_{r+}(x,z)}{\partial x}+(-2i\beta)\frac{\partial E_{r+}(x,z)}{\partial z})\exp(-iK_{r+}\cdot\vec{r})+\\
&((-2ik_\perp)\frac{\partial E_{i-}(x,z)}{\partial x}+(2i\beta)\frac{\partial E_{i-}(x,z)}{\partial z})\exp(-iK_{i-}\cdot\vec{r})+\\
&((2ik_\perp)\frac{\partial E_{r-}(x,z)}{\partial x}+(2i\beta)\frac{\partial E_{r-}(x,z)}{\partial z})\exp(-iK_{r-}\cdot\vec{r})]=-k_0^2\Delta\varepsilon(x,y,z)UE(x,z).
\end{aligned}
\tag{1.23}
$$

Multiplying the above equation with U(y) and integrating over y, we obtain

$$
\begin{aligned}
&((-2ik_\perp)\frac{\partial E_{i+}(x,z)}{\partial x}+(-2i\beta)\frac{\partial E_{i+}(x,z)}{\partial z})\exp(-iK_{i+}\cdot\vec{r})+\\
&((2ik_\perp)\frac{\partial E_{r+}(x,z)}{\partial x}+(-2i\beta)\frac{\partial E_{r+}(x,z)}{\partial z})\exp(-iK_{r+}\cdot\vec{r})+\\
&((-2ik_\perp)\frac{\partial E_{i-}(x,z)}{\partial x}+(2i\beta)\frac{\partial E_{i-}(x,z)}{\partial z})\exp(-iK_{i-}\cdot\vec{r})+\\
&((2ik_\perp)\frac{\partial E_{r-}(x,z)}{\partial x}+(2i\beta)\frac{\partial E_{r-}(x,z)}{\partial z})\exp(-iK_{r-}\cdot\vec{r})=-\Gamma k_0^2\Delta\varepsilon(x,z)E(x,z)
\end{aligned}
\tag{1.24}
$$

where Γ is the confinement factor.

We take advantage of the two dimensional periodicity of the index refraction to write it as

$$\Delta\varepsilon(x,z)=\sum_{l,m}\Delta\varepsilon_{l,m}\exp(iK_{l,m}\cdot\vec{r})\qquad K_{l,m}=l\frac{2\pi}{a}\vec{x}+m\frac{2\pi}{b}\vec{z} \tag{1.25}$$

$$\Delta\varepsilon_{l,m}=\frac{1}{ab}\int_{-b/2}^{b/2}\int_{-a/2}^{a/2}\Delta\varepsilon(x,z)\exp(-iK_{l,m}\cdot\vec{r})dxdz\,. \tag{1.26}$$

Thus, we have

$$\begin{aligned}
&((-2ik_{\perp})\frac{\partial E_{i+}(x,z)}{\partial x}+(-2i\beta)\frac{\partial E_{i+}(x,z)}{\partial z})\exp(-iK_{i+}\cdot\vec{r})+\\
&((2ik_{\perp})\frac{\partial E_{r+}(x,z)}{\partial x}+(-2i\beta)\frac{\partial E_{r+}(x,z)}{\partial z})\exp(-iK_{r+}\cdot\vec{r})+\\
&((-2ik_{\perp})\frac{\partial E_{i-}(x,z)}{\partial x}+(2i\beta)\frac{\partial E_{i-}(x,z)}{\partial z})\exp(-iK_{i-}\cdot\vec{r})+\\
&((2ik_{\perp})\frac{\partial E_{r-}(x,z)}{\partial x}+(2i\beta)\frac{\partial E_{r-}(x,z)}{\partial z})\exp(-iK_{r-}\cdot\vec{r})=-\Gamma k_0^2\sum_{l,m}\Delta\varepsilon_{l,m}\exp(iK_{l,m}\cdot\vec{r})\\
&[E_{i+}(x,z)\exp(-iK_{i+}\cdot\vec{r})+E_{r+}(x,z)\exp(-iK_{r+}\cdot\vec{r})+\\
&E_{i-}(x,z)\exp(-iK_{i-}\cdot\vec{r})+E_{r-}(x,z)\exp(-iK_{r-}\cdot\vec{r})].
\end{aligned} \tag{1.27}$$

This equation shows that each plane wave can couple into the other three waves through different Fournier components of $\Delta\varepsilon(x,z)$, given the condition

$$\beta=m\frac{\pi}{b},k_{\perp}=l\frac{\pi}{a},\quad(l\neq0,m\neq0). \tag{1.28}$$

For example, we consider the first order Fournier component coupling in both directions. Eq. (1.27) becomes

$$
\begin{aligned}
-k_{\perp}\frac{\partial E_{i+}(x,z)}{\partial x}-\beta\frac{\partial E_{i+}(x,z)}{\partial z} &= -\frac{i\Gamma k_0^2}{2}[\Delta\varepsilon_{0,1}E_{r+}(x,z)+\Delta\varepsilon_{1,0}E_{i-}(x,z)+\Delta\varepsilon_{1,1}E_{r-}(x,z)]\\
k_{\perp}\frac{\partial E_{r+}(x,z)}{\partial x}-\beta\frac{\partial E_{r+}(x,z)}{\partial z} &= -\frac{i\Gamma k_0^2}{2}[\Delta\varepsilon_{0,-1}E_{i+}(x,z)+\Delta\varepsilon_{1,-1}E_{i-}(x,z)+\Delta\varepsilon_{1,0}E_{r-}(x,z)]\\
-k_{\perp}\frac{\partial E_{i-}(x,z)}{\partial x}+\beta\frac{\partial E_{i-}(x,z)}{\partial z} &= -\frac{i\Gamma k_0^2}{2}[\Delta\varepsilon_{-1,0}E_{i+}(x,z)+\Delta\varepsilon_{-1,1}E_{r+}(x,z)+\Delta\varepsilon_{0,1}E_{r-}(x,z)]\\
k_{\perp}\frac{\partial E_{r-}(x,z)}{\partial x}+\beta\frac{\partial E_{r-}(x,z)}{\partial z} &= -\frac{i\Gamma k_0^2}{2}[\Delta\varepsilon_{-1,-1}E_{i+}(x,z)+\Delta\varepsilon_{-1,0}E_{r+}(x,z)+\Delta\varepsilon_{0,-1}E_{i-}(x,z)].
\end{aligned}
\tag{1.29}
$$

The coupling relationship is illustrated in Fig. 1.7.

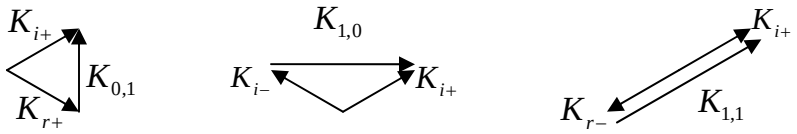

Figure 1.7: Coupling relationships between K_{r+}, K_{i-}, K_{r-}, and K_{i+}

1.2.2 One dimensional TBR waveguides

For one dimensional TBR waveguides, light is guided by Bragg reflection only in the transverse direction. Thus, we can design one dimensional TBR waveguides by using one dimensional Bragg gratings in the transverse direction. In Ref. [13], although two dimensional periodic structures were used, the longitudinal feedback was not taken into account in the analysis. So the structure analyzed in Ref. [13] is essentially an example of one dimensional TBR waveguides.

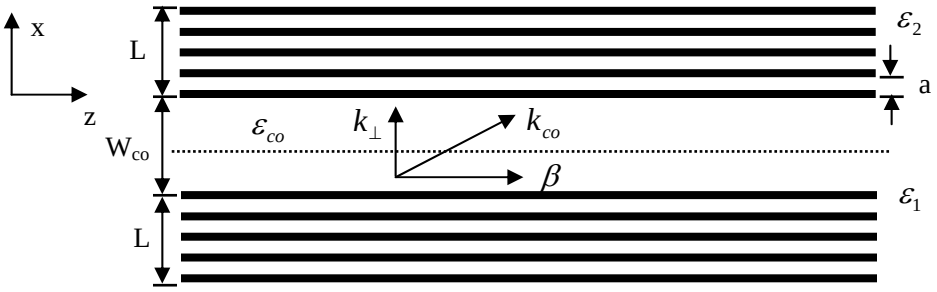

Figure 1.8: Schematic of a one dimensional TBR waveguide

Figure 1.8 shows the schematic of a one dimensional TBR waveguide. As shown in Fig. 1.8, the TBR waveguide consists of a slab guiding channel (with dielectric constant ε_{co} and width W_{co}) sandwiched between two Bragg reflectors. The Bragg reflectors alternate between a high-index layer with dielectric constant ε_1 and a low-index layer with dielectric constant ε_2. The Bragg grating period is a.

The electrical fields in the guiding channel and grating region can be, respectively, written as

$$E_{GC}(x,z) = E_{i+}\exp(-i(k_\perp x + \beta z)) + E_{r+}\exp(-i(-k_\perp x + \beta z)) \tag{1.30}$$

$$E_{grating}(x,z) = E_{i+}(x)\exp(-i(k_\perp x + \beta z)) + E_{r+}(x)\exp(-i(-k_\perp x + \beta z)). \tag{1.31}$$

Using Eq. (1.16), (1.28), and (1.29), we can obtain the coupled wave equation for the transverse Bragg grating region

$$\begin{aligned}\frac{\partial E_{i+}(x)}{\partial x} &= \frac{i\Gamma k_0^2}{2k_\perp}\Delta\varepsilon_1 E_{r+}(x) = \kappa_\perp E_{r+}(x)\\ \frac{\partial E_{r+}(x)}{\partial x} &= -\frac{i\Gamma k_0^2}{2k_\perp}\Delta\varepsilon_{-1} E_{i+}(x) = -\kappa_\perp E_{r+}(x)\end{aligned} \tag{1.32}$$

$$\kappa_\perp = \frac{i\Gamma k_0^2}{2k_\perp}\Delta\varepsilon_{-1} \tag{1.33}$$

$$k_{\perp} = l\pi / a \tag{1.34}$$

$$k_{\perp}^2 + \beta^2 = n_{eff}^2 k_0^2 . \tag{1.35}$$

We can write the solution for Eq. (1.32) as

$$\begin{aligned} r_{upper} &= \left.\frac{E_{r+}(x)}{E_{i+}(x)}\right|_{x=W_{co}/2} = i\tanh(|\kappa_{\perp}|L) \\ r_{lower} &= \left.\frac{E_{i+}(x)}{E_{r+}(x)}\right|_{x=-W_{co}/2} = i\tanh(|\kappa_{\perp}|L). \end{aligned} \tag{1.36}$$

Using Eq. (1.30), we have

$$\begin{aligned} r_{upper} &= \left.\frac{E_{r+}(x)}{E_{i+}(x)}\right|_{x=W_{co}/2} = \frac{E_{r+}\exp(ik_{\perp}W_{co}/2)}{E_{i+}\exp(-ik_{\perp}W_{co}/2)} \\ r_{lowwer} &= \left.\frac{E_{i+}(x)}{E_{r+}(x)}\right|_{x=W_{co}/2} = \frac{E_{r+}\exp(ik_{\perp}W_{co}/2)}{E_{i+}\exp(-ik_{\perp}W_{co}/2)}. \end{aligned} \tag{1.37}$$

Then, we can obtain

$$r^2\exp(-i2k_{\perp}W_{co}) = 1, \quad r = i\tanh(|\kappa_{\perp}|L) . \tag{1.38}$$

Focusing on the phase condition part of Eq. (1.38), we have

$$2k_{\perp}W_{co} = m\pi , \quad m = 1,3,5,7.... \tag{1.39}$$

Using Eq. (1.30) and assuming the first order Bragg condition, we have

$$W_{co} = ma/2 , \quad m = 1,3,5,7.... \tag{1.40}$$

It is clear that the width of the guiding channel has to satisfy Eq. (1.40) to support a guided optical mode.

For a particular optical wave its transverse wavevector has to match the transverse Bragg grating vector to satisfy the phase matching condition. The transverse Bragg

grating limits the allowed transverse wavevectors in a narrow band defined by the grating reflection spectrum, similar to the situation where the DFB structure limits the longitudinal wavevectors. Meanwhile, the device has a limited size in the transverse direction. Thus, we can engineer the grating to support only one low loss mode while all the other high order modes experience significant diffraction losses. This low loss mode spreads out the entire width of the device and can be as wide as hundreds of microns. In terms of laser applications, this feature will allow us to design the single transverse mode, large-area semiconductors laser [25].

1.2.3 Asymmetric TBR waveguides

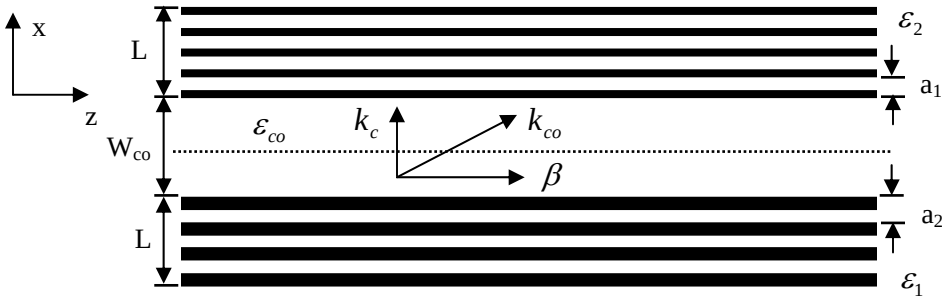

Figure 1.9: Schematic of the asymmetric one dimensional TBR waveguide

In principle, two Bragg reflectors of the one dimemnsional TBR waveguide do not have to be the same. As shown in Fig. 1.9, the asymmetric TBR waveguide consists of a slab (with dielectric constant ε_{co} and width W_{co}) sandwiched by two different Bragg reflectors. Similar to the symmetric TBR waveguide, the Bragg reflectors alternate between a high-index layer with dielectric constant ε_1 and a low-index layer with dielectric constant ε_2. Here, we also consider the gain of the medium, represented by the dielectric constant $i\varepsilon_I$. For simplicity, we assume that two Bragg reflectors have the same index perturbation profile, total length L and duty cycle of 50%. But the upper Bragg grating has a period of a_1 and the lower one has a period of a_2.

Similar to Eq. (1.30) and (1.31), we can express the electrical field in the grating region as

$$E(x,z) = A(x)\exp(-ik_{\perp}x - i\beta z) + B(x)\exp(ik_{\perp}x - i\beta z) \tag{1.41}$$

$$\beta = \beta_R + i\beta_I \tag{1.42}$$

$$\omega^2\mu\bar{\varepsilon} = \beta_R{}^2 + k_{\perp}{}^2 \qquad \bar{\varepsilon} = (\varepsilon_1 + \varepsilon_2)/2\,. \tag{1.43}$$

Using the coupled-wave formalism proposed in Ref. [13, 17, 25], we can describe the coupling relationship in the grating region using the following equation

$$\begin{aligned} \frac{\partial A(x)}{\partial z} &= \gamma A + i\kappa\exp(i2\Delta k_m)B(x) \\ \frac{\partial B(x)}{\partial z} &= -\gamma B - i\kappa\exp(-i2\Delta k_m)A(x) \end{aligned} \tag{1.44}$$

$$\kappa = \frac{\omega^2}{2\pi k_{\perp}c^2}(\varepsilon_1 - \varepsilon_2) \tag{1.45}$$

$$\Delta k_m = k_{\perp} - \frac{\pi}{b_m} \tag{1.46}$$

$$\gamma = \frac{\omega^2\mu\varepsilon_I}{2k_{\perp}} - \frac{\beta_R\beta_I}{k_{\perp}} \tag{1.47}$$

where m = 1, 2 correspond to the upper grating and lower grating, respectively.

From Eq. (1.44), we can obtain the field distribution in the grating region subject to the condition that at the outer edges of the grating there is no reflected wave

$$B(L) = 0 \quad \text{and} \quad A(-W_{co} - L) = 0$$

$$\begin{aligned} E^{(clad)}_{0<x\le L}(x) = F\Big\{ & \exp(-i\pi x/b_1)\frac{(\gamma - i\Delta k_1)\sinh[S_1(L-x)] - S_1\cosh[S_1(L-x)]}{(\gamma - i\Delta k_1)\sinh(S_1L) - S_1\cosh(S_1L)} \\ & + \exp(+i\pi x/b_1)\frac{\kappa\sinh[S_1(L-x)]}{(\gamma - i\Delta k_1)\sinh(S_1L) - S_1\cosh(S_1L)} \Big\} \end{aligned} \tag{1.48}$$

$$E^{(clad)}_{-L-W_{co}\le x<-W_{co}}(x) = G\Big\{\ \exp(-i\pi x/b_2 - i\pi W_{co}/b_2)\frac{\kappa\sinh[S_2(L+x+W_{co})]}{(\gamma-i\Delta k_2)\sinh(S_2L)-S_2\cosh(S_2L)} + \exp(i\pi x/b_2 + i\pi W_{co}/b_2)\frac{(\gamma-i\Delta k_2)\sinh[S_2(L+x+W_{co})]-S_2\cosh[S_2(L+x+W_{co})]}{(\gamma-i\Delta k_2)\sinh(S_2L)-S_2\cosh(S_2L)}\ \Big\} \tag{1.49}$$

$$S_1 = \sqrt{|\kappa|^2-(\gamma-\Delta k_1)^2} \qquad S_2 = \sqrt{|\kappa|^2-(\gamma-\Delta k_2)^2} \tag{1.50}$$

where F and G are scale factors that will be needed for matching the fields at the boundaries ($x=0$ and $x=-W_{co}$).

Assuming $\bar{\varepsilon}=\varepsilon_{co}$, we can also use Eq. (1.44) to describe the field in the core region with $\kappa=0$. We write the confined field in the core region as

$$E(x,z) = \Big\{\ A\exp[-ik_c(x+W_{co}/2)] \pm B\exp[ik_c(x+W_{co}/2)]\ \Big\}\exp(-\beta z) \tag{1.51}$$

$$k_c = k_\perp + i\gamma\,. \tag{1.52}$$

For an asymmetric TBR waveguide, A and B are not real numbers, which is different from a symmetric TBR waveguide. Thus, the corresponding field distribution in the core region is not symmetric to the core center ($x=-W_{co}/2$).

Using the boundary conditions in Ref. [25], we have

$$\begin{aligned} &A\exp(-ik_cW_{co}/2) = F \\ &B\exp(ik_cW_{co}/2) = \frac{\pm\kappa F}{(\gamma-i\Delta k_1)-S_1\coth(S_1L)} \quad \text{at} \quad x=0 \end{aligned} \tag{1.53}$$

$$\begin{aligned} &A\exp(ik_cW_{co}/2) = \frac{\kappa G}{(\gamma-i\Delta k_2)-S_2\coth(S_2L)} \quad \text{at} \quad x=-W_{co}\,. \\ &B\exp(-ik_cW_{co}/2) = \pm G \end{aligned} \tag{1.54}$$

It follows that

$$\exp(2ik_cW_{co}) = \frac{\kappa^2}{[(\gamma-i\Delta k_1)-S_1\coth(S_1L)][(\gamma-i\Delta k_2)-S_2\coth(S_2L)]}\,. \tag{1.55}$$

This condition can be written in terms of the magnitude and phase as

$$\exp(-2\gamma W_{co}) = \left| \frac{\kappa^2}{[(\gamma - i\Delta k_1) - S_1 \coth(S_1 L)][(\gamma - i\Delta k_2) - S_2 \coth(S_2 L)]} \right| \tag{1.56}$$

$$2k_{\perp} W_{co} = 2m\pi + phase\left[\frac{\kappa^2}{[(\gamma - i\Delta k_1) - S_1 \coth(S_1 L)][(\gamma - i\Delta k_2) - S_2 \coth(S_2 L)]} \right]. \tag{1.57}$$

For a passive and sufficiently wide ($L >> 1$) waveguide, we have

$$\gamma = 0 \quad \coth(S_1 L) = \coth(S_1 L) = 1. \tag{1.58}$$

Eq. (1.56) automatically satisfies when $\left|\Delta k_{1,2}\right| < \kappa$.

Therefore, assuming $b_2 > b_1$ and $\kappa < \pi / b_{1,2}$, for a guided mode we have

$$\pi / b_1 - \kappa \le k_{\perp} \le \pi / b_2 + \kappa. \tag{1.59}$$

Using the analysis in Ref. [17], we can obtain the total number of the guided modes

$$N_{\mathrm{mod}e} \cong \frac{\pi / b_2 - \pi / b_1 + 2\kappa}{\Delta k_{diff}} = \frac{\pi / b_2 - \pi / b_1 + 2\kappa}{\pi / W_{co}} = (1/b_2 - 1/b_1 + 2\kappa/\pi) W_{co} \tag{1.60}$$

$$W_{co}^{\ sig} = 1/(1/b_2 - 1/b_1 + 2\kappa/\pi) = b_1 b_2 /(b_1 - b_2 + 2b_1 b_2 \kappa/\pi). \tag{1.61}$$

$W_{co}^{\ sig}$ is defined as the largest core width of a TBR waveguide that can support only one mode. By carefully selecting b_1 and b_2, we can significantly increase this width, as shown in Fig. 1.10.

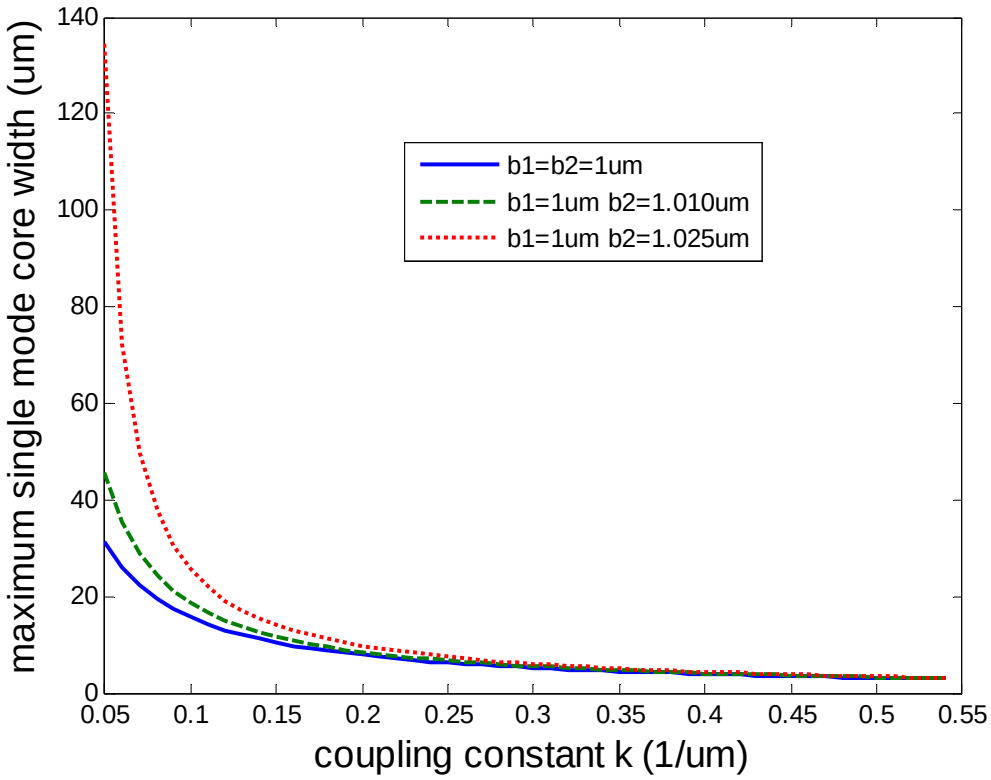

Figure 1.10: Dependence of W_{co}^{sig} on the coupling constant κ for different symmetric and asymmetric TBR waveguides

Chapter 2

Modal gain analysis of TBR waveguides and lasers

In Chapter 1, we have introduced the coupled mode analysis of the one dimensional TBR waveguide with a "defect" guiding channel. The coupled mode approach solves for the Bragg-guided modes but does not account for other optical modes in the structure, such as the effective index-guided and gain-guided modes. In this chapter, we use a transfer matrix method (TMM) to analyze the modal gain/loss of all the possible modes supported by the one dimensional TBR waveguide with and without a "defect". We compare different low loss optical modes for these two structures. We show that gain modulation in the transverse direction can also guide TBR modes. We conclude by suggesting three possible feedback mechanisms that can be used to ensure the lasing of Bragg-guided modes only.

2.1 Introduction

Total internal reflection (TIR) is the most common waveguiding mechanism for the semiconductor lasers. In these structures, the single transverse mode operation at a particular wavelength can be achieved by controlling the refractive index difference between the waveguide core and cladding. For a large-area (> 20 μm modal width) single mode operation, a very small index contrast ($\Delta n < 10^{-4}$) is needed. The weak index difference makes the laser sensitive to fluctuations in its operating conditions that alter its

refractive index profile. Filamentation also often occurs for large-area semiconductor lasers, which leads to the multiple transverse mode operation and broad, multi-lobe far field.

In order to overcome these problems, waveguiding structures that use the Bragg reflection from a periodic structure rather than total internal reflection to confine light in the direction transverse to the propagation direction have been proposed and used for large-area, edge emitting lasers [14, 25–30]. These structures do not require very small index contrast and can be designed to have a single lateral mode that is distributed throughout the entire width of the laser for efficient and stable operation even at relatively high powers.

One example of these structures is the angled-grating distributed feedback (α-DFB) semiconductor laser proposed by Lang et al., in which a uniform transverse grating provides the waveguiding mechanism and the angle facet selects the desired mode [14, 26]. Another example proposed by Yariv uses a guiding channel sandwiched between two gratings [13, 25]. The guiding channel is a “defect” in the grating and can suppress the radiation loss. In these grating waveguide structures, a resonance condition needs to be satisfied in the transverse direction to support a low loss optical mode. Here, we generalize these two examples as the transverse Bragg resonance (TBR) structures, and we refer to the modes that depend on the transverse grating resonance as the TBR modes.

However, in these structures, optical modes which are not guided by the transverse Bragg grating can also lase when the gain is provided. First, effective index-guided mode can exist when the cladding index is smaller than the low index region of the transverse grating. Second, low loss leaky modes due to incomplete TIR (gain-guided modes) can exist in these wide waveguide structures regardless of the cladding index. Thus, we need a formalism that accounts for all the optical modes of the structure as well as their losses. For the practical laser design based on the transverse Bragg reflection, we also need to engineer the Bragg-guided modes to be the preferred lasing modes.

2.2 Transverse Bragg Resonance waveguides with and without a defect

2.2.1 Transfer Matrix Method

Figure 2.1 shows the TBR structure without and with a defect. In Fig. 2.1(a), the TBR structure consists of uniform Bragg reflectors in the transverse direction. In Fig. 2.1(b), a defect core (with refractive index n_{co} and width W_d) is present at the center of the grating. The Bragg reflectors consist of alternating high- and low- index layers with refractive indices n_h and n_l, respectively. The refractive index outside the waveguide region is n_{out}. The grating has N layers, a period *a* and a duty cycle *d*. We define the average index of the grating n_{avg} as: $n_{avg} = n_h \cdot d + n_l \cdot (1-d)$. The refractive index of the defect core n_{co} is assumed to be n_h or n_l. In accordance with the round-trip resonance condition and the phase of reflection from the grating, for a mode to be supported by the defect, we have $W_d = (m+1/2)a$, where m is an integer (Eq. (1.40)).

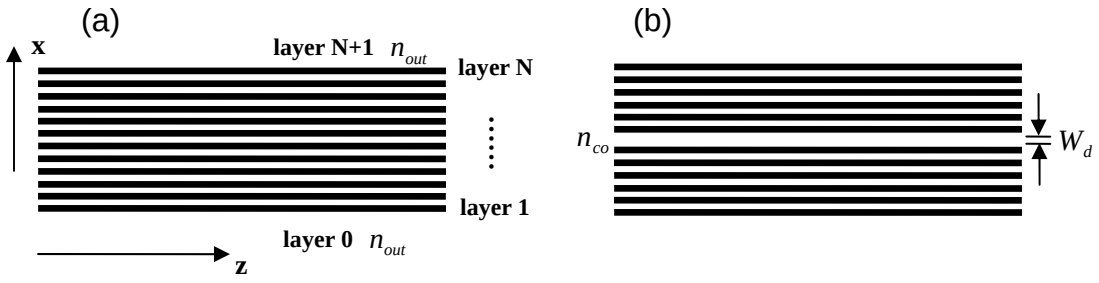

Figure 2.1: Transverse Bragg resonance structures (a) without a defect core, (b) with a defect core

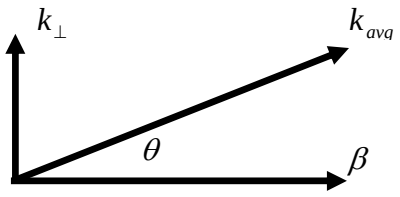

Figure 2.2: Schematic definition of the modal angle

Using the plane wave approximation, we can define an important parameter—the modal angle θ for the optical mode of the TBR structures, as shown in Fig. 2.2

$$\theta = \cos^{-1}(\beta / k_{avg}) = \sin^{-1}(k_{\perp} / k_{avg}). \tag{2.1}$$

According to the coupled-mode analysis in Chapter 1, light can be confined by the transverse Bragg grating when its transverse wavevector matches the Bragg grating vector. Therefore we define the corresponding modal angle as the transverse resonance angle for both structures. Using Eq. (1.34), (1.35) and (2.1), we have

$$\theta_{res} = \cos^{-1}[\sqrt{(2\pi n_{avg} / \lambda)^2 - (\pi / b)^2} / (2\pi n_{avg} / \lambda)]. \tag{2.2}$$

The grating coupling coefficient around the resonance condition can be calculated using Eq. (1.33) and (1.5)

$$\kappa_{index} = (2b / \lambda^2)(n_h^2 - n_l^2)\sin(\pi d). \tag{2.3}$$

Our analysis is based on the transfer matrix method proposed in Ref. [14]. In this approach, the structure is considered to consist of a series of dielectric layers, each characterized by a label n=0,1,…,N, N+1 (see Fig. 2.1). We assume that an optical mode propagating in the positive z direction has a spatial dependence $\exp(-i\beta z)$, where β is a real or complex constant. It should be pointed out that β needs to be a real number for a regular waveguide mode in most situations. Thus, when the corresponding optical mode

propagates through the structure, there is no diffraction loss. However, the structure here is for the laser applications and we want to include the radiation (leaky) modes in the discussion. The complex propagation constant accounts for the leaky mode. The imaginary part of a complex β is the propagation loss of the corresponding leaky mode. In the following analysis, we are going to show that some leaky modes can have small propagation losses and thus can lase when the gain is provided.

In each layer, the electrical field can be written as the sum of the forward going ($E_{f,n}$, +x) and backward going waves ($E_{b,n}$, -x)

$$E(x) = E_{f,n}\exp(-ik_n(x-x_n)) + E_{b,n}\exp(ik_n(x-x_n)) \tag{2.4}$$

$$k_{s,n} = {2\pi n_n}\big/{\lambda} + ig_n \tag{2.5}$$

$$k_n = \sqrt{k_{s,n}^2 - \beta^2} \tag{2.6}$$

where $k_{s,n}$ is the wavevector for the plane wave in each layer with gain g_n and x_n is the x coordinate of the start of the nth layer. We can express the field and its derivative within one layer in the following format using a matrix

$$\begin{pmatrix} E_n(x) \\ E_n'(x) \end{pmatrix} = T_n(x-x_n)\cdot\begin{pmatrix} E_{f,n} \\ E_{b,n} \end{pmatrix} \tag{2.7}$$

$$T_n(x) = \begin{pmatrix} \exp(-ik_n x) & \exp(ik_n x) \\ -ik_n\exp(-ik_n x) & ik_n\exp(ik_n x) \end{pmatrix}. \tag{2.8}$$

Since β is the same for all the layers, we can match the field and its derivative at every interface and propagate the field from layer 0 to layer N+1. We self-consistently solve for the field distribution where the field outside the cladding layers is purely outgoing. The corresponding boundary condition for the transfer matrix method is $E_{f,0} = 0$ and $E_{b,N+1} = 0$. Thus, we can start with the field in the layer 0

$$\begin{pmatrix} E_{f,0} \\ E_{b,0} \end{pmatrix} = \begin{pmatrix} 0 \\ 1 \end{pmatrix}. \tag{2.9}$$

Using Eq. (2.7), we have

$$\begin{pmatrix} E_0(0) \\ E_0^{'}(0) \end{pmatrix} = T_0(0) \cdot \begin{pmatrix} E_{f,0} \\ E_{b,0} \end{pmatrix}. \tag{2.10}$$

Matching the field and its derivative at the boundary, we have

$$\begin{pmatrix} E_1(0) \\ E_1^{'}(0) \end{pmatrix} = \begin{pmatrix} E_0(0) \\ E_0^{'}(0) \end{pmatrix} = T_0(0) \cdot \begin{pmatrix} E_{f,0} \\ E_{b,0} \end{pmatrix}. \tag{2.11}$$

Using Eq. (2.7) again， we have

$$\begin{pmatrix} E_{f,1} \\ E_{b,1} \end{pmatrix} = T_1^{-1}(0) \cdot T_0(0) \cdot \begin{pmatrix} E_{f,0} \\ E_{b,0} \end{pmatrix}. \tag{2.12}$$

Keeping matching the fields and derivatives through each boundary of the waveguide, we can obtain the expression for the layer N+1

$$\begin{pmatrix} E_{f,N+1} \\ E_{b,N+1} \end{pmatrix} = T_{N+1}^{-1}(0) \cdot T_N(d_N) \ldots\ldots T_2^{-1}(0) \cdot T_1(d_1) \cdot T_1^{-1}(0) \cdot T_0(0) \cdot \begin{pmatrix} E_{f,0} \\ E_{b,0} \end{pmatrix}. \tag{2.13}$$

Satisfying the boundary condition at layer N+1, $E_{b,N+1} = 0$, gives a series of β.

A lossless optical mode corresponds to a real β. In our structures, the lossless mode is the effective index-guided mode. A complex β corresponds to a leaky mode and it experiences an exponential decay of the field amplitude in the propagation direction and an exponential increase in the transverse direction of the cladding region [31]. This means that a complex β is not a physical solution of Maxwell's equations because the field amplitude increases to infinity in the transverse direction. However, when the gain is provided for the grating region to exactly compensate the decay of the field, β becomes real and the field amplitude remains constant in the propagation direction. Thus, in our approach, the imaginary part of β corresponds to the gain required to support a lossless optical mode with its propagation constant equal to the real part of β. So we define the real part of β as the phase propagation constant and the imaginary part as the modal

gain and regard the corresponding field distribution as the mode for the waveguide. Negative modal gain is equivalent to the modal loss. Using Eq. (2.1), we also define the modal angle as

$$\theta = \cos^{-1}(\mathrm{Re}(\beta)/(2\pi n_{avg}/\lambda)). \tag{2.14}$$

Using this transfer matrix method, we can account for both lossless modes and leaky modes in the TBR structure.

2.2.2 Optical modes of transverse Bragg resonance waveguides

First, to compare the performance of the TBR structures with and without a defect, we calculate the modal gain for each mode as a function of the modal angle for three different passive structures in Fig. 2.3. We assume: $n_h = 3.25$; $n_l = 3.245$; $d = 0.5$; $n_{out} = 3.25$; $b = 1$ μm; $W_d = 0.5$ μm; $N = 100$; $\lambda = 1.55$ μm. Therefore, the resonance angle calculated from Eq. (2.2) is 13.8° and the coupling constant calculated from Eq. (2.3) is 270/cm.

In Fig. 2.3, the y coordinate is the modal loss, which is the imaginary part of β; the x coordinate is the modal angle, which is determined by the real part of β. Thus, each point in Fig. 2.3 corresponds to a β, essentially an optical mode. As shown in Fig. 2.3, in all the structures considered, the optical modes with small modal angles experience zero or very low radiation loss. We define these modes as the small modal angle (SMA) modes. SMA modes include both lossless effective index-guided modes and low loss leaky modes. They are almost parallel to the grating and do not radiate significantly. SMA modes will be discussed in detail later.

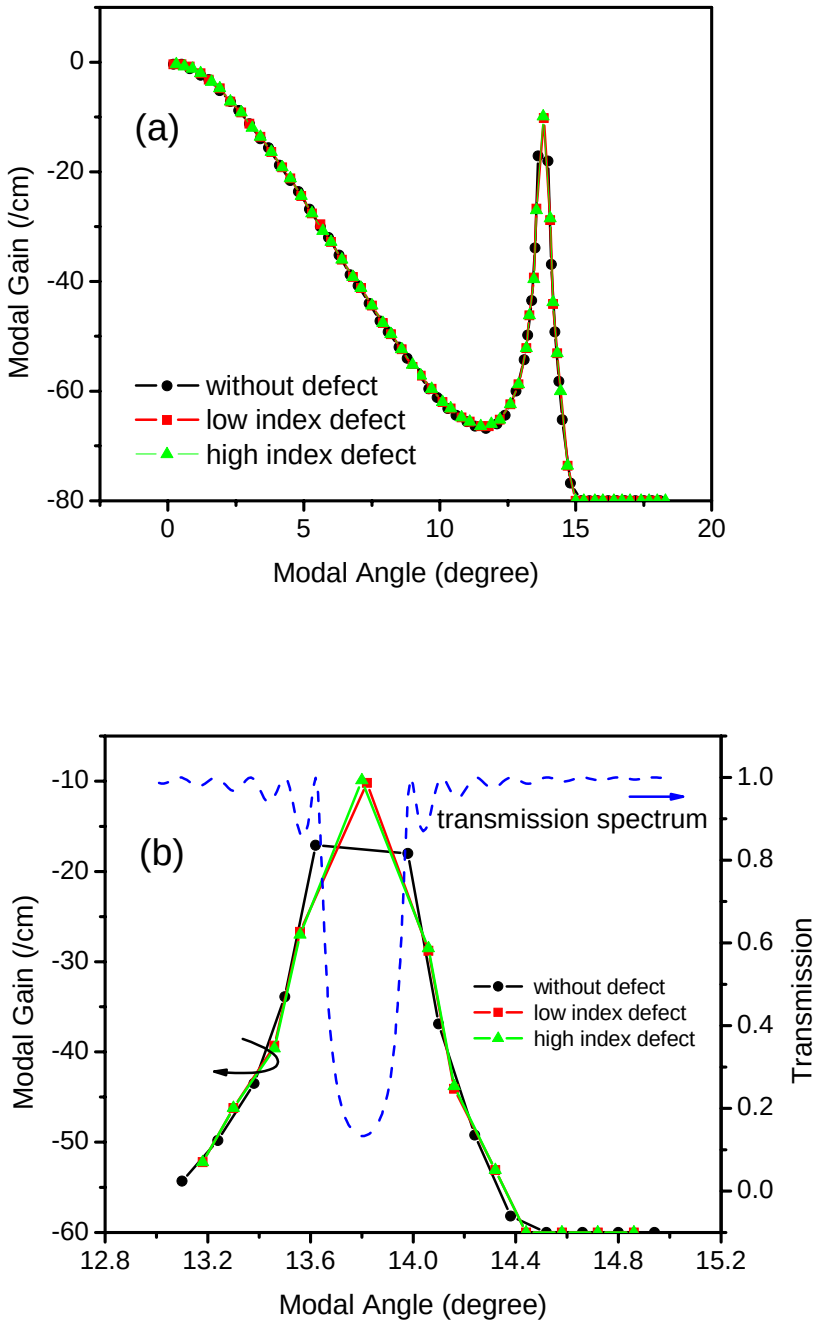

Figure 2.3: (a) Modal gain (loss) versus modal angle for passive TBR waveguides with and without a defect. (b) Modal gain of TBR modes near the resonance angle (solid lines) and the transmission spectrum of the grating (the dashed line)

As the modal angle increases, all the modes experience higher radiation loss. However, around the transverse resonance angle of 13.8°, low loss modes exist. These modes are supported by the transverse grating and are therefore the TBR modes. For a finite structure, TBR modes are leaky due to non-unity grating reflectivity. Compared to the SMA modes, TBR modes have much larger intermodal discrimination between the lowest loss and the next lowest loss modes, which is the key in realizing the single transverse mode operation.

Figure 2.3(b) shows the modal gain for the modes near the transverse Bragg resonance. We also plot the transmission spectrum of the grating at different modal angles to illustrate the relationship between the location of TBR modes and the stop band of the grating. For the TBR waveguide without a defect (the line with circles), the two lowest loss modes are located on either side of the stop band of the grating, similar to a longitudinal DFB structure. While for the TBR waveguide with a defect (the lines with squares and triangles), the lowest loss mode is in the middle of the stop band of the grating, similar to a longitudinal DFB structure with a π phase slip [32]. The defect TBR modes experience about 7/cm less radiation loss than the lowest loss modes for the same TBR waveguide without a defect. The modal losses are similar between the TBR waveguide with a low-index defect and a high-index defect. For these two structures, the modal angles of the lowest loss TBR modes are both 13.8°, which match the prediction from the coupled-mode analysis.

In Fig. 2.3(b), the allowed modal angles of the TBR modes correspond to the discrete transmission peaks (without a defect) and dips (with a defect) of the grating spectrum. TBR structures with and without defects both support multiple Bragg-guided modes because the finite device width imposes a second transverse resonance condition and thus leads to the mode splitting. For all the three cases we discussed, the gain difference between the lowest loss TBR modes and the next lowest loss TBR modes is as high as 17/cm.

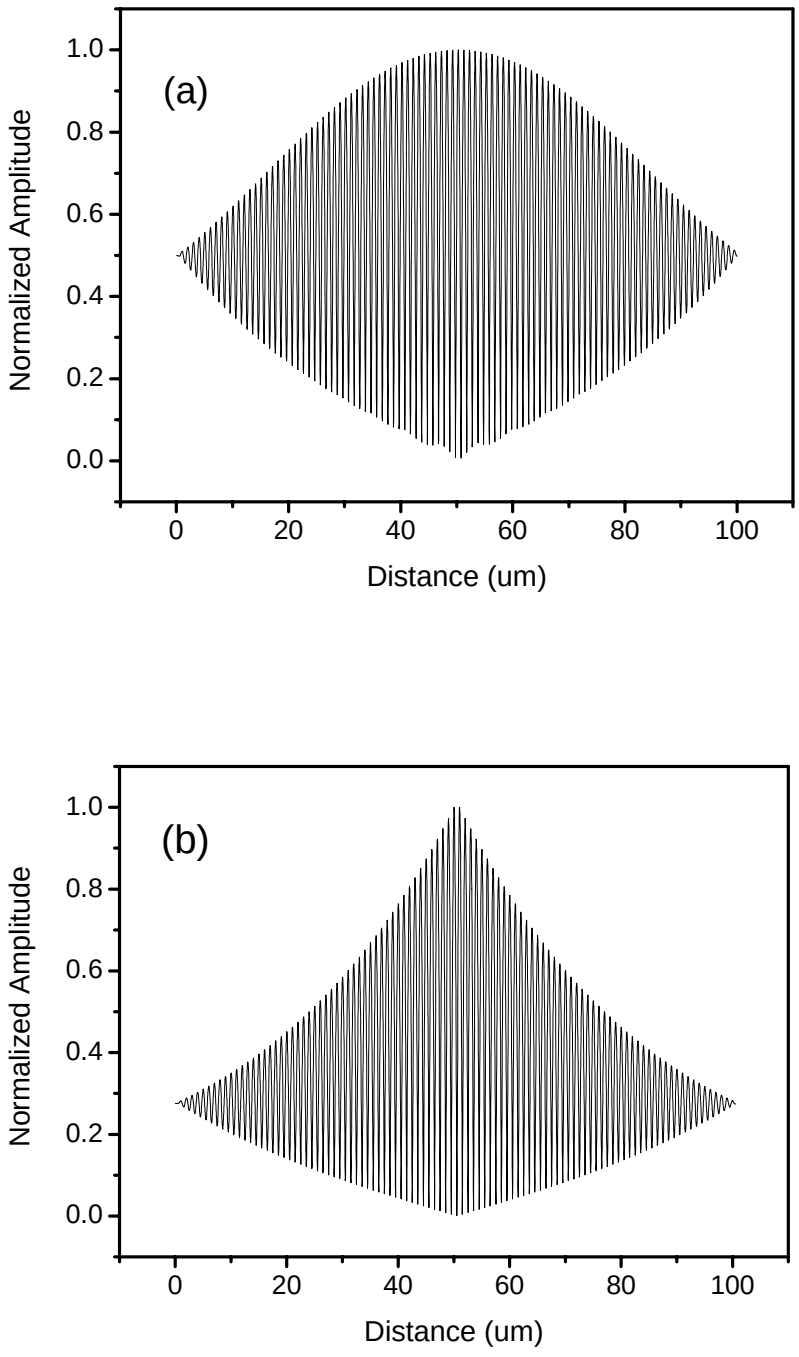

Figure 2.4: The normalized field amplitude. (a) Lowest loss TBR mode (no defect) with 13.63° modal angle and 16.88/cm loss. (b) Lowest loss TBR mode (high-index defect) with 13.80° modal angle and 9.94/cm loss

Figure 2.4 shows the normalized electric field amplitudes for different lowest loss TBR modes. The modes possess a "fast" spatial oscillation due to the grating. Since the field in the cladding is assumed to be purely outgoing, the energy leaks out at two boundaries (x = 0 and x = 100 μm). In Fig. 2.4, it is clear that the more confined mode has relatively smaller amplitude at the boundary.

We can reduce the loss of TBR modes to be almost zero through the grating design. In Fig. 2.5, we show the modal gain and the field profile of the lowest loss TBR mode for such a design. The design is for the TBR waveguide with a high-index defect and all the parameters are the same as in Fig. 2.3 except that $n_l = 3.24$. The coupling constant of this grating is about 540/cm, much higher than the one in Fig. 2.3. Thus we can obtain a more confined TBR mode. In Fig. 2.5, the radiation loss for the lowest loss TBR mode is about 1 dB/cm.

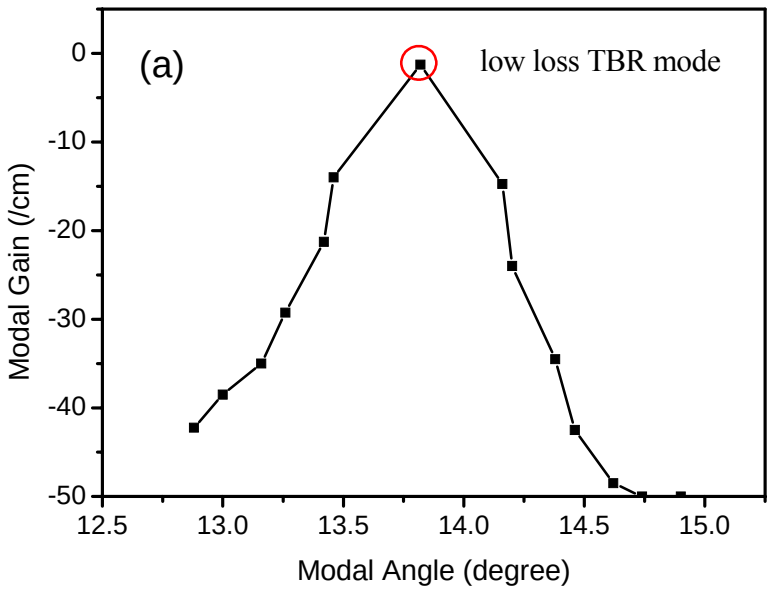

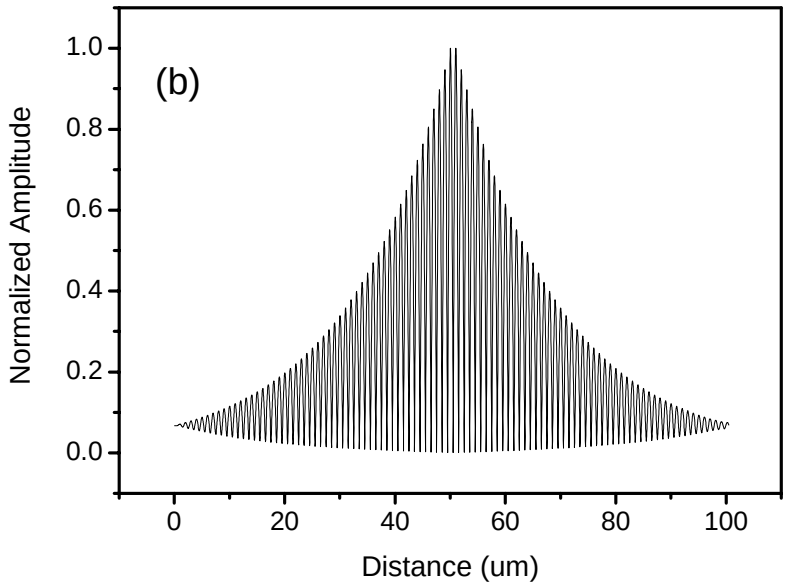

Figure 2.5: (a) Modal gain (loss) versus modal angle for the TBR waveguide with a high-index defect. (b) The electric field amplitude of the corresponding lowest loss TBR mode. All the simulation parameters are the same as in Fig. 2.3 except for $n_l = 3.24$.

2.2.3 Gain-guided transverse Bragg resonance waveguides

Periodic gain (loss) modulation in the transverse direction can also support TBR modes. For the transverse gain-modulated grating structure, we assume that the refractive index is the same everywhere and the grating alternates between a high gain layer with g_h and a low gain layer with g_l. There is no defect in this gain grating. The grating, as in the above example, has N layers, a period *b*, and a duty cycle *d*. We calculate the modal gain of all the modes for this transverse gain-modulated structure in Fig. 2.6. The simulation parameters are as follow: $g_h = 50/cm$; $g_l = 0$; $n_{background} = 3.2475$; $d = 0.5$; $b = 1$ μm; $N = 100$; $\lambda = 1.55$ μm.

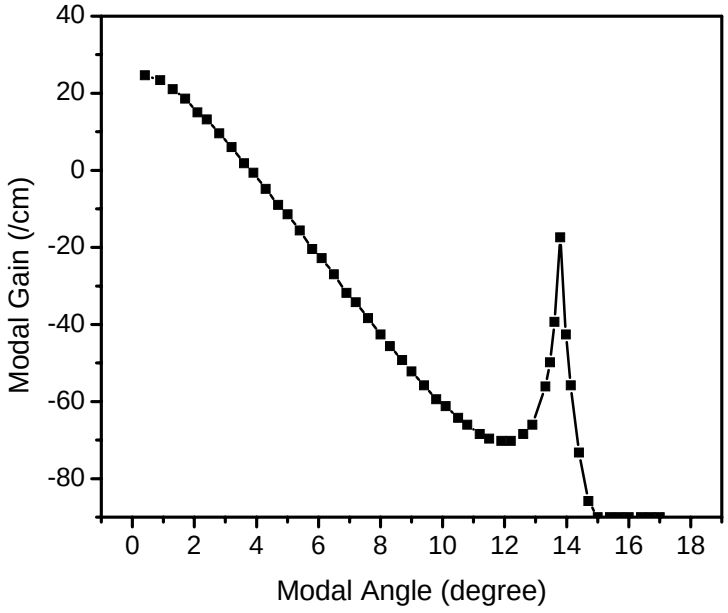

Figure 2.6: Modal gain versus modal angle for a gain-guided TBR waveguide

We obtain both SMA modes and TBR modes for the gain coupled TBR waveguide as well. The lowest loss mode of TBR modes is exactly located at the 13.8° transverse resonance angle predicted by the coupled mode theory, similar to a pure gain coupled DFB structure [33]. Since gain is provided for the waveguide, SMA modes possess positive modal gain. On the contrary, the lowest loss TBR mode still experiences about 20/cm radiation loss. This means that the confinement for this gain coupled grating is not very strong. The coupling constant for the gained coupled grating can be calculated as: $\kappa_{gain} = (2b/\lambda)(g_h - g_l)\sin(\pi d)/\pi$ [33]. In the example above, the gain coupling constant is about 20.5/cm, which is much weaker than the coupling constant of the index coupled grating in Fig. 2.3.

2.2.4 Small modal angle modes

SMA modes possess zero or very small radiation losses and compete with the desired TBR modes when the gain is provided. The layers outside the grating strongly interact

with SMA modes since they propagate almost parallel to the grating. In Fig. 2.7, we show the modal gain of both the SMA and TBR modes for a high-index defect TBR waveguide with different values of n_{out}. The three lines correspond to the situation when the cladding index is smaller than, equal to, and larger than the average index of the grating, respectively. When the cladding index is the same as the average index of the grating, the SMA modes experience the most radiation loss.

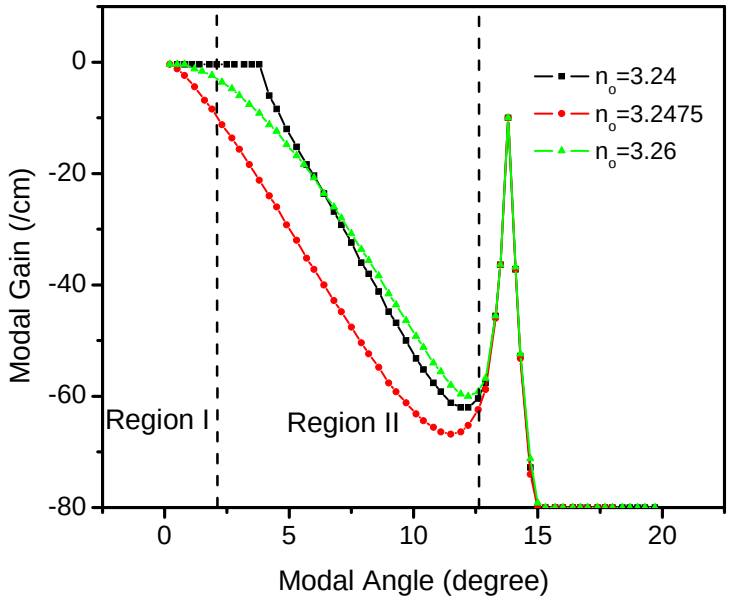

Figure 2.7: Modal gain (loss) versus modal angle for the passive defect TBR waveguide with different outside claddings. All simulation parameters are the same as in Fig. 2.3 except n_{out}.

There are several origins for the SMA modes. First, lossless effective index-guided waveguide modes can exist when the cladding index is less than the low-index region of the grating (n_l). In this case ($n_{out} = 3.24$, Fig. 2.7), the propagation constant β is a real number and satisfies the condition $2\pi n_l / \lambda < \beta < 2\pi n_h / \lambda$. Thus the field is guided in the high-index regions of the grating and is evanescent in the low-index regions of the grating and the cladding. In Fig. 2.8, we plot such fields for three different situations: no defect, high-index defect, and low-index defect. The field distribution has a strong

dependence on the defect. In contrast to the TBR modes shown in Fig. 2.4 and Fig. 2.5, the field profiles of the effective index-guided SMA modes only have very small amplitude oscillations corresponding to the grating period on top of the overall slowly varying envelope.

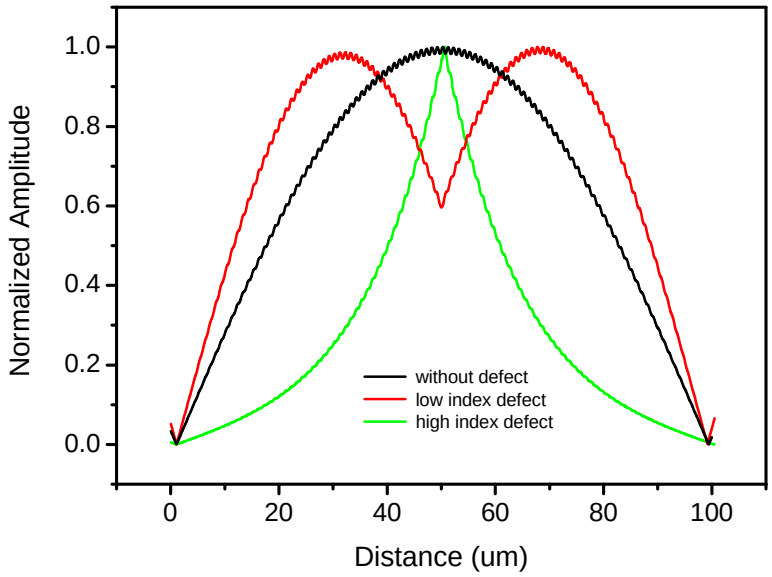

Figure 2.8: The electrical field amplitudes of the lossless effective index-guided modes when the outside cladding index $n_{out} = 3.24$. Other simulation parameters are the same as in Fig. 2.3.

As the cladding index increases ($n_{out} = 3.2475$ and $n_{out} = 3.26$, Fig. 2.7), these modes become leaky and their propagation constants become complex numbers. If the condition $2\pi n_l / \lambda < \mathrm{Re}(\beta) < 2\pi n_h / \lambda$ is satisfied (Region I in Fig. 2.7), the radiation loss for these modes is very small. This is because that the Fresnel reflectivity at the interfaces approaches unity when the angle of incidence reaches 90° (0° modal angle). Thus, the losses due to incomplete TIR from the dielectric interfaces are expected to be small when the light is at grazing incidence. In Ref. [31], it is also shown that the radiation loss for these modes become smaller as the total waveguide width increases. The field distribution of the lowest loss (order) leaky SMA modes is similar to the corresponding

lossless effective index-guided modes in Fig. 2.8. When the modal angle is larger than this range (Region II, $\mathrm{Re}(\beta) < 2\pi n_l / \lambda$), the radiation loss increases unless the mode can be guided by the grating.

Now, it is clear that TBR structures support two kinds of modes: TBR modes and SMA modes. TBR modes are supported by the transverse grating. The loss difference between the lowest loss (order) and the next lowest loss TBR modes is high. SMA modes include lossless effective index-guided modes and leaky modes with small modal angles. The existence of lossless effective index-guided waveguide modes depends on the cladding index, while leaky modes with small modal angles exist regardless of the cladding index. The loss difference among all the SMA modes is small. In Fig. 2.9, we plot the dispersion relation of the lowest loss TBR mode and six lowest loss (order) SMA modes for a passive TBR waveguide. The loss for the TBR mode is about 1dB/cm, and losses for the SMA modes are all less than 2dB/cm.

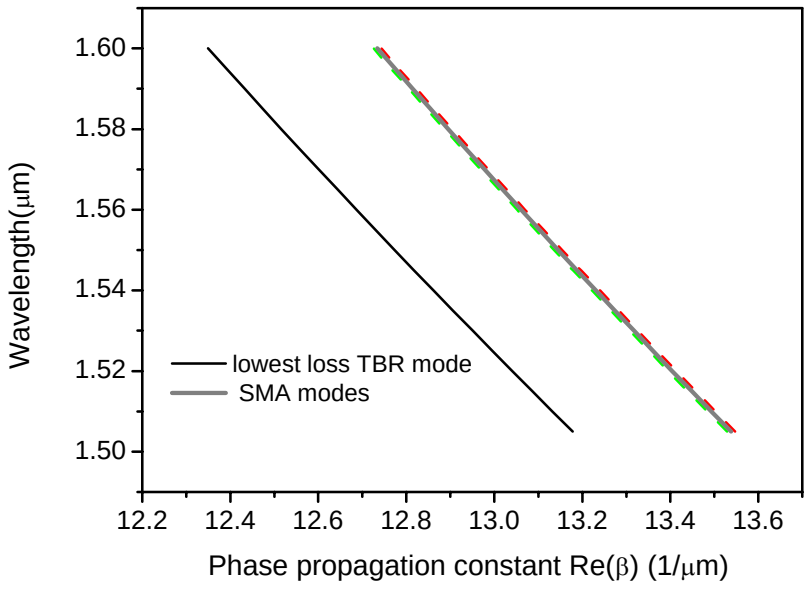

Figure 2.9: Dispersion relation of the lowest loss TBR mode (the black line) and SMA modes (the gray region). There are six lines in the gray region, and each of them is corresponding to one particular SMA mode. All simulation parameters are the same as in Fig. 2.5.

When the gain is provide for a TBR waveguide, the lowest loss TBR mode and SMA modes have similar gain. Thus, the TBR modes and SMA modes compete with each other and both of them can lase.

2.3 Feedback mechanisms for the transverse Bragg resonance lasers

Thus far, we have only discussed TBR waveguides. To analyze lasers, we must include the effect of the feedback mechanism that defines the resonator. To ensure a single transverse mode operation near the Bragg resonance, the feedback mechanism needs to be tailored. Compared to SMA modes, TBR modes have a much "faster" spatial oscillation in the transverse direction. Thus, if we can integrate a spatial filter at the facet to favor the fast spatial oscillation, TBR modes can be preferred. Angled facets were proposed in Ref. [14] to realize this goal. The angled facets act exactly like a spatial filter and the feedback from the facet will only be provided for the mode whose modal angle is very close to the tilt angle.

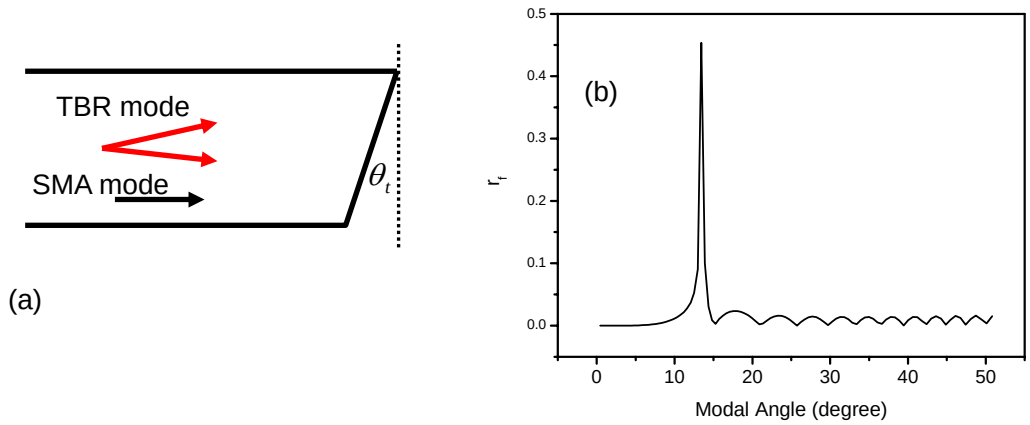

Figure 2.10: (a) An angled facet with a tilt angle θ_t. (b) r_f for all the modes with different modal angles

The reflectivity of different modes at an angled facet can be calculated using the model in Ref. [34]:

$$R = R_f(\theta_t) \cdot A \cdot r_f \quad \text{with} \quad r_f = \mathrm{Re}(\beta)\int_{-\infty}^{+\infty} |E|^2 e^{i2\theta\,\mathrm{Re}(\beta)x} dx \tag{2.15}$$

where x is the transverse coordinate, θ_t is the tilt angle for the facet (see. Fig. 9) and $R_f(\theta_t)$ is the Fresnel reflection coefficient of the dielectric interface between semiconductor and air. A is a constant. In Fig. 2.10, we calculate r_f in Eq. (2.15) for all the normalized modes with different modal angles of the TBR waveguide described in Fig. 2.5. The tilt angle is assumed to be 13.8° in the calculation. r_f in Eq. (2.15) possesses a maximum value for the mode with a modal angle same as the tilt angle. The reflectivity for TBR modes can thus be designed to be maximum by choosing the tilt angle θ_t to be the same as the resonance angle θ_{res}. While for SMA modes, r_f in Eq. (2.15) is almost zero. Thus, these modes are not reflected by the facet. Indeed, the angled facet is a spatial filter which gives the strongest reflection for the mode with the modal angle same as the tilt angle.

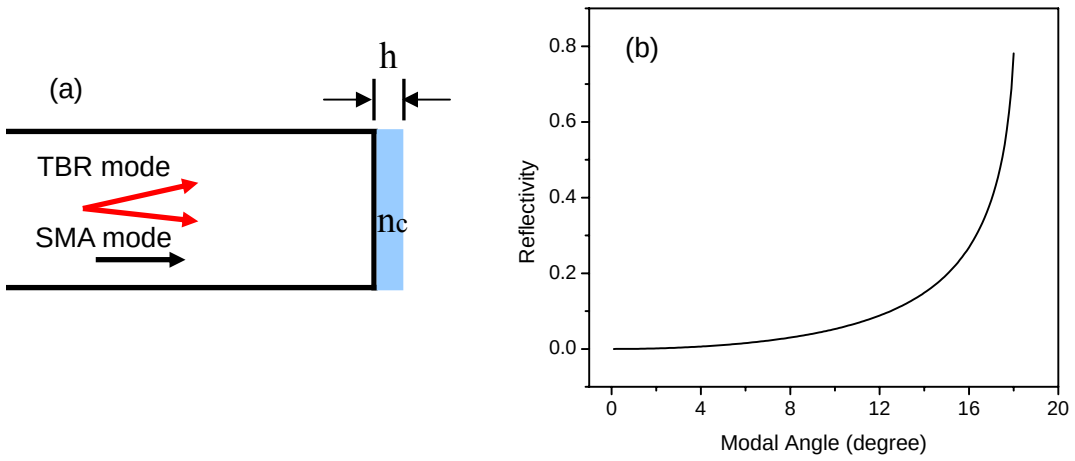

Figure 2.11: (a) A coated facet design. The coating layer has a refractive index n_c and thickness h. (b) The reflectivity for all the modes with different modal angles

A second approach is to coat the facet in a way such that the reflection for the modes

with small modal angles is almost zero while the reflection for the modes around the transverse resonance angle is high. Thus, a similar selection mechanism can be achieved as an angled facet design. Since the modal angle difference between the SMA modes and TBR modes are large, a typical single layer antireflection coating can achieve this goal, as shown in Fig. 2.11.

In Fig. 2.11 (a), the laser facet is coated with a dielectric layer with a refractive index n_c and thickness h. Details of the antireflection coating design can be found in Ref. [35]. Here, we optimize our design for the mode with 0° modal angle. Thus, we have

$$n_c = \sqrt{n_{avg} n_{air}} \ , \quad h = \lambda / 4 n_c \tag{2.16}$$

where n_{air} is the refractive index of air and λ is the wavelength. Given $n_{air} = 1$, $n_{avg} = 3.245$, and $\lambda = 1.55$ μm, we calculate the reflectivity for the modes with different modal angles in Fig. 2.11 (b). When the modal angle is less than 2°, the reflectivity of all the calculated modes is smaller than 2*10-3. Thus the SMA modes can not obtain enough feedback from the facet. While for the TBR modes (modal angle ~ 13.8°), the reflectivity is around 0.18, two orders higher than the SMA modes. Since the SMA modes and TBR modes are the only low loss modes supported by the structure, the coating layer can effectively discriminate against the SMA modes and ensure the lasing in the TBR modes.

The third way is to introduce a second grating in the longitudinal direction to select the propagation constant corresponding to the TBR mode [27, 28, 36, 37]. It should be pointed out that the angled facet design was also used to suppress the SMA modes and provide a single lobe far field output. However, the facet reflection is not the feedback mechanism. Thus the tilt angle does not need to be the transverse resonance angle and the exact value is not critical, which is different from the first approach.

Chapter 3

Design of photonic crystal Bragg lasers

3.1 Introduction

In the past chapters, we show that one dimensional TBR structures can support only one low loss Bragg-guided transverse mode. Combining with an angled facet design to suppress gain-guided modes, the TBR structure can be used to make the large-area, edge emitting semiconductor laser with a single transverse mode. However, these structures still support multiple longitudinal modes since the feedback is provided by the end facets [39–41].

In order to obtain a stable single mode operation, we incorporate an additional longitudinal grating into the one dimensional TBR structure. There are essentially two methods to integrate the longitudinal grating: (1) The transverse and longitudinal Bragg gratings are located at the different layers in the vertical direction and we refer this structure as the double-layer two dimensional grating structure; (2) The transverse and longitudinal Bragg gratings are located at the same layer. Thus we obtain a two dimensional photonic crystal structure， and we refer this structure as the photonic crystal Bragg structure. For simplicity, we do not consider the defects in these structures.

Due to the fabrication limitation, we can not process the semiconductor regrowth. Since the double-layer two dimensional grating structure requires the regrowth process, we only discuss the basic concepts of this structure. We will focus on the design of the

photonic crystal Bragg structure in this chapter. In order to avoid the regrowth process, the photonic crystal is fabricated on the surface of the semiconductor wafer. Unlike conventional two dimensional photonic crystal lasers [11, 42, 43], which use a large refractive index perturbation to confine light in a plane, the two dimensional periodic structures described here selectively control the longitudinal and transverse wavevector components using a weak index perturbation. Thus, the optical modes confined by the grating in these laser designs will spread out into the periodic active medium, allowing for high power operation.

The angled facet design prevents gain-guided modes from lasing. Thus, we can use the coupled mode analysis for the design of the photonic crystal Bragg structure since it works well with Bragg-guided modes and provides analytic solutions. We will show that the photonic crystal Bragg structure is theoretically identical to the double-layer two dimensional grating structure by ignoring the cross coupling terms in the coupled mode analysis.

3.2 From one dimensional TBR structures to two dimensional TBR structures

Figure 3.1 shows the schematic of the one dimensional TBR laser based on the analysis developed in Chapter 2. The Bragg grating in the transverse direction provides the waveguiding mechanism and supports a single transverse mode operation [44]. The angled facets are used to suppress gain-guided modes. If the facet tilt angle is the same as the mode angle of the Bragg-guided mode, the facets can provide the feedback for the Bragg-guided mode. However, it is difficult to obtain a single longitudinal mode operation due to this kind of feedback mechanism. In order to obtain the single mode operation, we need both the single transverse mode and single longitudinal mode.

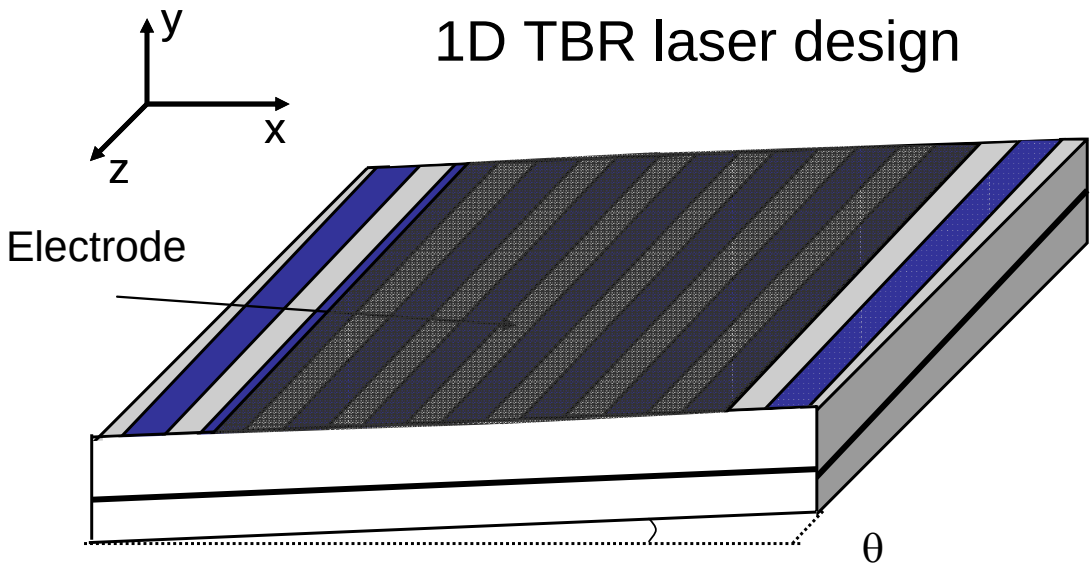

Figure 3.1: Schematic illustration of a one dimensional TBR laser structure

It is well known that we can use the DFB structure to control the longitudinal mode of semiconductor lasers. Thus, we can incorporate a longitudinal DFB structure into the one dimensional TBR laser to obtain the single mode operation of large-area, edge emitting semiconductor lasers. First, we can put two orthogonal one dimensional gratings along the vertical direction. One grating is for the transverse mode control and the other grating is for the longitudinal mode control. We refer this structure as the double-layer two dimensional grating structure. The drawback of this approach is that we need a semiconductor regrowth process in fabrication. Second, we can use a photonic crystal structure in the wafer plane for the modal control of both the transverse and longitudinal directions, since the photonic crystal structure can provide the distributed feedback in both directions [45]. We can also fabricate the photonic crystal structure on the surface of the semiconductor wafer in order to avoid the regrowth process. We refer this structure as the photonic crystal Bragg structure. In the following sections, we discuss both structures in detail.

3.3 Double-layer two dimensional Bragg grating lasers

Figure 3.2 shows the schematic of a double-layer two dimensional grating laser structure. The laser has two orthogonal gratings, each in a different layer. One grating is for the longitudinal mode control and the other is for the transverse mode control. The active quantum well region below the gratings provides the optical gain. In the limit of weak index perturbation, the optical mode for this structure can be separated into transverse (x), vertical (y), and longitudinal (z) components.

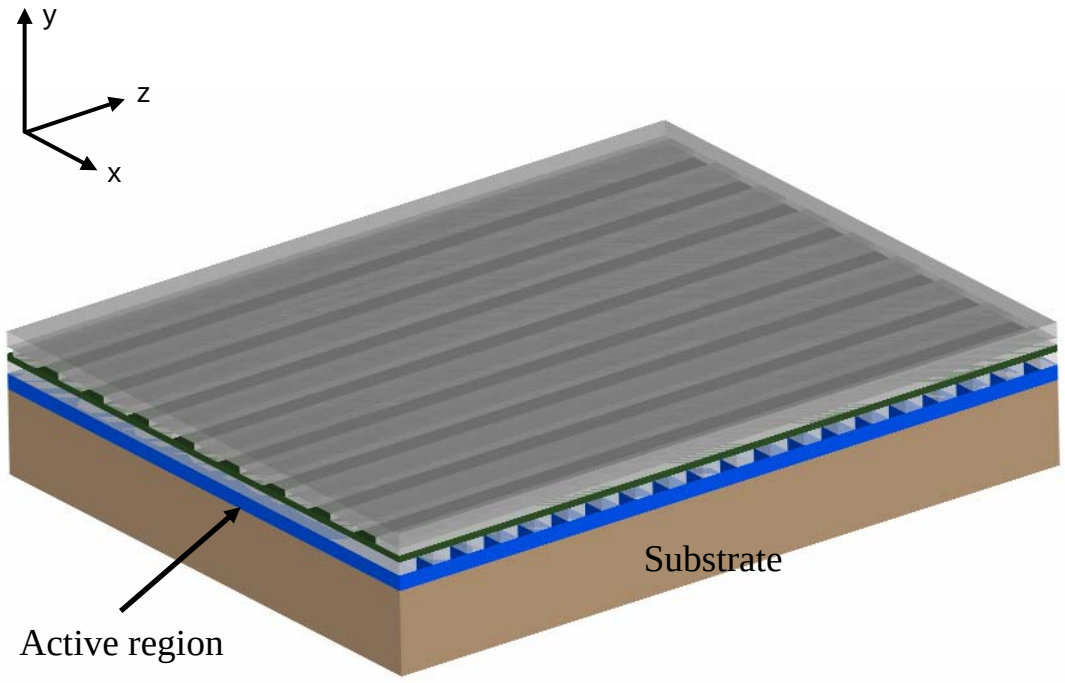

Figure 3.2: Schematic illustration of a double-layer two dimensional Bragg grating laser structure

Using a similar analysis to Chapter 1's, we begin with the wave equation

$$\nabla^2 E + \varepsilon(x,y,z)k_0^2 E = 0 \tag{3.1}$$

$$\varepsilon(x,y,z) = \bar{\varepsilon}(y) + \Delta\varepsilon_{\substack{transverse \\ grating}} + \Delta\varepsilon_{\substack{longitudinal \\ grating}} \tag{3.2}$$

where $\bar{\varepsilon}(y)$ is for the unperturbed structure without two gratings.

First we consider the unperturbed situation with $\Delta\varepsilon = 0$; the general solution takes the form

$$E(x,y,z) = U(y)E_{//}\exp(-i(k_x x + k_z z)) \tag{3.3}$$

where k_x is the transverse wavevector, k_z is the longitudinal wavevector, and $E_{//}$ is a constant. Then we substitute this solution form into the wave equation, we have

$$\frac{d^2U(y)}{dy^2} + (\bar{\varepsilon}(y)k_0^2 - k_x^2 - k_z{}^2)U(y) = 0\,. \tag{3.4}$$

For a specific index distribution along y, we can obtain the modal distribution U(y) and the effective index n_{eff}. Then we include the index perturbation, assuming the U(y) is unaffected. We express the field as

$$E(x,y,z) = U(y)E(x,z)\,. \tag{3.5}$$

Putting the field expression into the wave equation, we have

$$\frac{d^2U}{dy^2}E(x,z) + \bar{\varepsilon}(y)k_0^2 UE(x,z) + U\left(\frac{d^2E(x,z)}{dx^2} + \frac{d^2E(x,z)}{dz^2}\right) = -k_0^2(\Delta\varepsilon_{tg} + \Delta\varepsilon_{\lg})UE(x,z) \tag{3.6}$$

$$Un_{eff}^2 k_0^2 E(x,z) + U\left(\frac{d^2E(x,z)}{dx^2} + \frac{d^2E(x,z)}{dz^2}\right) = -k_0^2(\Delta\varepsilon_{tg} + \Delta\varepsilon_{\lg})UE(x,z)\,. \tag{3.7}$$

We assume $\Delta\varepsilon_{tg}$ and $\Delta\ \varepsilon_{\ \lg}$ are uniform along y in the grating region (straight sidewalls). Multiplying the above equation with U(y) and integrating over y, we obtain

$$\frac{d^2E(x,z)}{dx^2}+\frac{d^2E(x,z)}{dz^2}=-k_0^2(n_{eff}^2+\Gamma_t\Delta\varepsilon(x)+\Gamma_l\Delta\varepsilon(z))E(x,z) \tag{3.8}$$

$$\Gamma_t=\frac{\int_{tg}U^2(y)dy}{\int_{-\infty}^{+\infty}U^2(y)dy} \tag{3.9}$$

$$\Gamma_l=\frac{\int_{lg}U^2(y)dy}{\int_{-\infty}^{+\infty}U^2(y)dy} \tag{3.10}$$

where Γ_t is the transverse grating confinement factor and Γ_l is the longitudinal grating confinement factor. Eq. (3.8) describes the field distribution in the transverse and longitudinal directions.

We can also assume

$$E(x,z)=E(x)E(z)\,. \tag{3.11}$$

Substituting Eq. (3.11) into Eq. (3.8) and separating the equation into x terms and z terms, we have

$$\frac{d^2E(x)}{dx^2}+k_0^2\Gamma_t\Delta\varepsilon(x)E(x)=-k_0^2n_1^2E(x) \tag{3.12}$$

$$\frac{d^2E(z)}{dz^2}+k_0^2\Gamma_l\Delta\varepsilon(z)E(z)=-k_0^2n_2^2E(z) \tag{3.13}$$

$$n_1^2+n_2^2=n_{eff}^2\,. \tag{3.14}$$

It shows that we can treat the index perturbation as two independent, one dimensional gratings, each with a different confinement factor. At this stage, we can take advantage of the general properties of a DFB laser and a TBR laser to analyze the double-layer two dimensional Bragg grating laser.

In principle, the double-layer two dimensional Bragg grating structure can control both the longitudinal and transverse wavevectors for single mode, high power semiconductor

laser applications. Since the two gratings are not coupled to each other, the analysis and design are also simple. However, the fabrication of this structure needs the semiconductor regrowth, which is beyond our capability. We only present the basic concepts of the double-layer two dimensional grating structure. Future work can explore more properties of this interesting structure.

3.4 Photonic crystal Bragg lasers

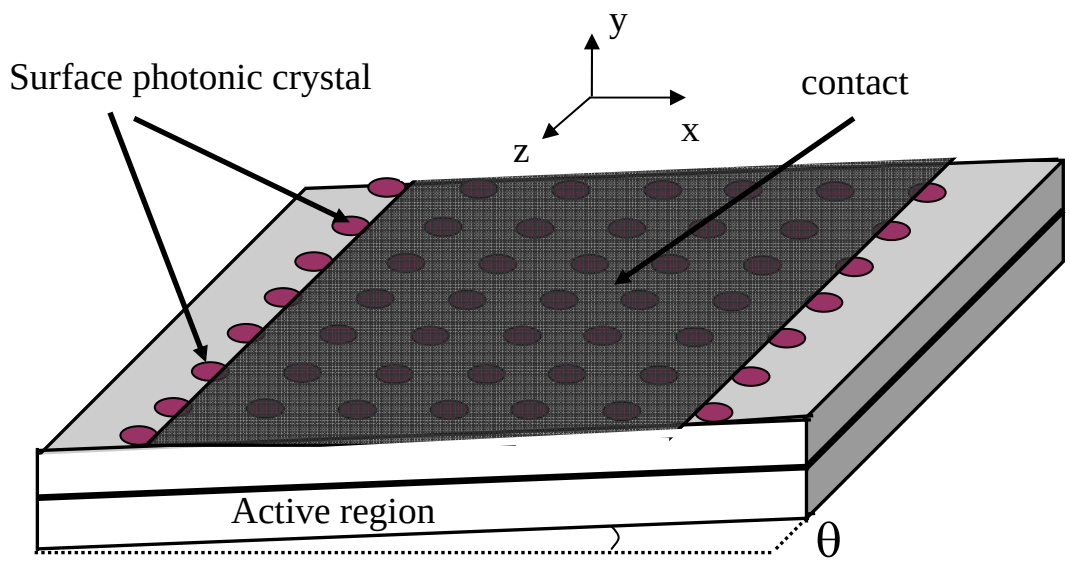

Figure 3.3: Schematic illustration of a photonic crystal Bragg laser structure

Figure 3.3 shows the schematic illustration of a photonic crystal Bragg laser structure. The surface photonic crystal controls the wavevectors of an optical mode in both the longitudinal and transverse directions, since we can think of the photonic crystal here as two one dimensional gratings on top of each other. Usually we do not etch through the active quantum well region since that could introduce the defects in the active region. Thus the distance from the quantum well region to the wafer surface and the etch depth of

the photonic crystal are critical in determining the effectiveness of the photonic crystal. The photonic crystal does not have to consist of circular holes. But other types of shapes, such as rectangles, have sharp corners, which can cause the optical nonlinearity. The end facts are tilted to suppress gain-guided modes. It should be pointed out that the laser operates at the band edge of the photonic crystal since the defect is not included in the design. Although the photonic crystal possesses a fourfold rotational symmetry, the laser can operate in a single mode due to additional perturbing reflections from the cleaved facets. This additional perturbation breaks the unwanted degeneracy as in regular DFB lasers with cleaved facets [3].

3.4.1 Wafer structures

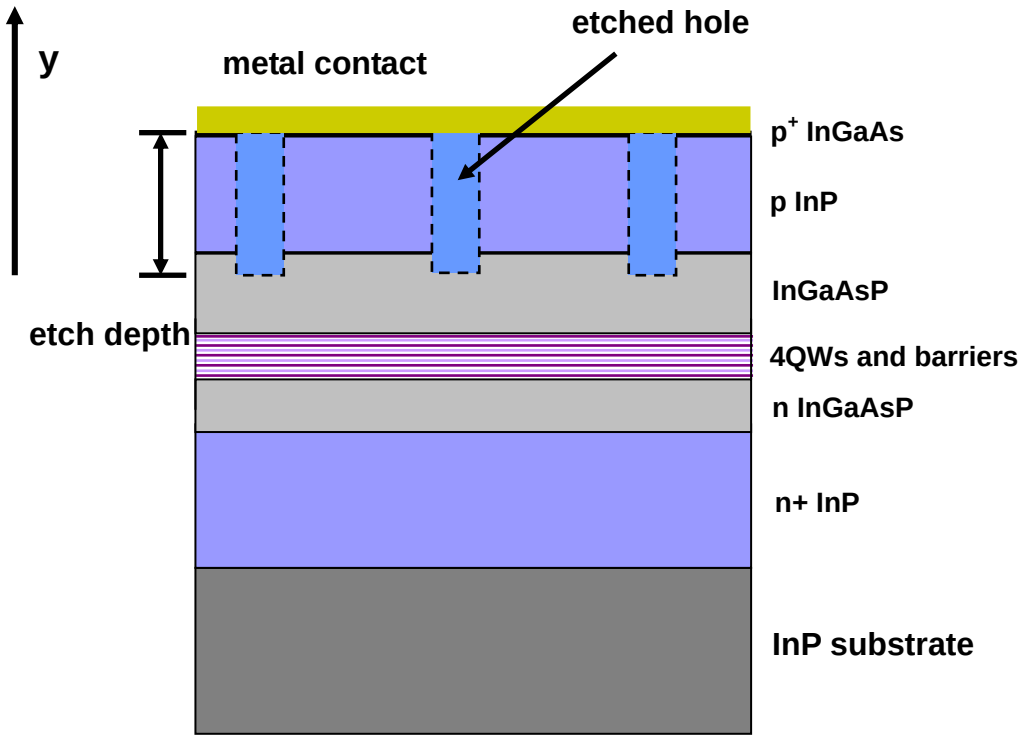

Figure 3.4: Schematic illustration of the cross section of a photonic crystal Bragg laser

Layer	Description	Material	Thickness(˚A)	Index	doping
0	Substrate	InP		3.1720	n
1	Buffer	InP	10000	3.1720	n+
2	Waveguide	InGaAsP	700	3.2911	n
3	Waveguide	InGaAsP	300	3.3203	undoped
4	Waveguide	InGaAsP	500	3.3755	undoped
5	QW	InGaAsP	85	3.5300	undoped
6	Barrier	InGaAsP	100	3.3755	undoped
7	QW	InGaAsP	85	3.5300	undoped
8	Barrier	InGaAsP	100	3.3755	undoped
9	QW	InGaAsP	85	3.5300	undoped
10	Barrier	InGaAsP	100	3.3755	undoped
11	QW	InGaAsP	85	3.5300	undoped
12	Waveguide	InGaAsP	500	3.3755	undoped
13	Waveguide	InGaAsP	400	3.3484	undoped
14	Cladding	InGaAsP	1300	3.3484	p
15	Cladding	InP	4000	3.1720	p
16	Contact layer	InGaAS	50	3.5550	p+

Table 3.1: Epitaxial wafer structure

Figure 3.4 shows the schematic illustration of the cross section of a photonic crystal Bragg laser. For each etched hole, we usually fill it with the planarization polymer so that the subsequently deposited metal will not fall into the hole. When fabricating the surface photonic crystal, we want to keep the etch depth less than 500 nm to ensure good etching profiles. Thus we should design the active quantum well region close to the wafer surface.

However, since the electrical contact will be directly put on the etched surface, the active region can not be too close to the surface. Otherwise, the metal contact will cause significant absorption losses and lead to a high threshold. With these two constricts, we come up with the wafer design in Table 3.1. In this design, the p+ contact layer is only 5 nm thick. This is because this wafer is also designed for other research projects and this InGaAs layer serves as a thin etch mask [46]. Ideally, the contact layer should be thicker than 50 nm.

Given this wafer structure, we can calculate the modal distribution in the vertical direction and the effective index n_{eff}. With this vertical modal profile, we can then calculate the confinement factor of the photonic crystal with different etched depths using Eq. (1.7).

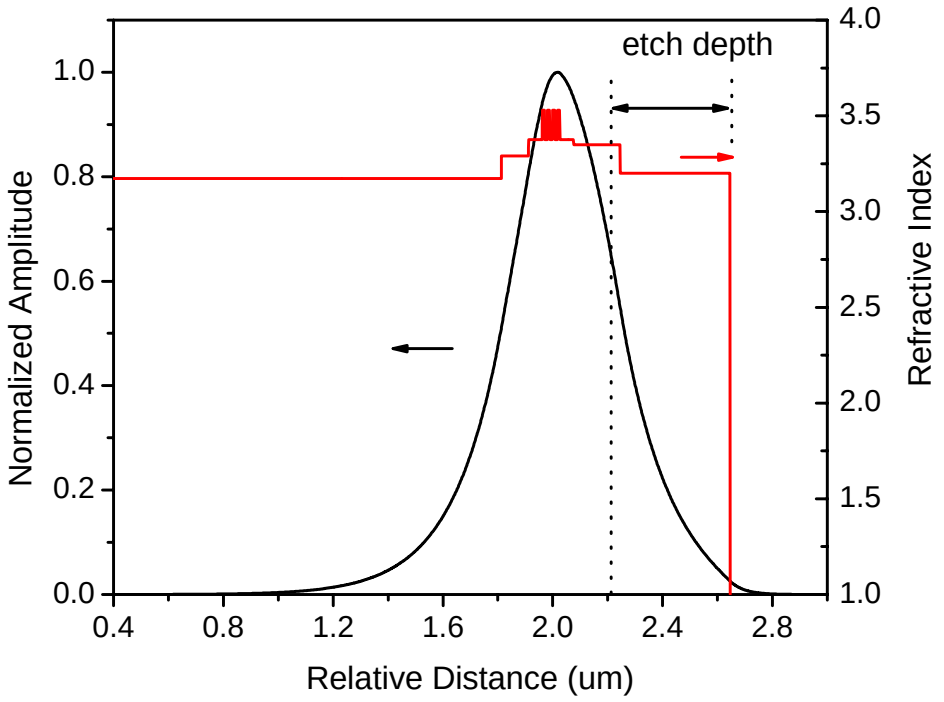

Figure 3.5: The index profile of the wafer epitaxial structure and the modal distribution in the vertical direction

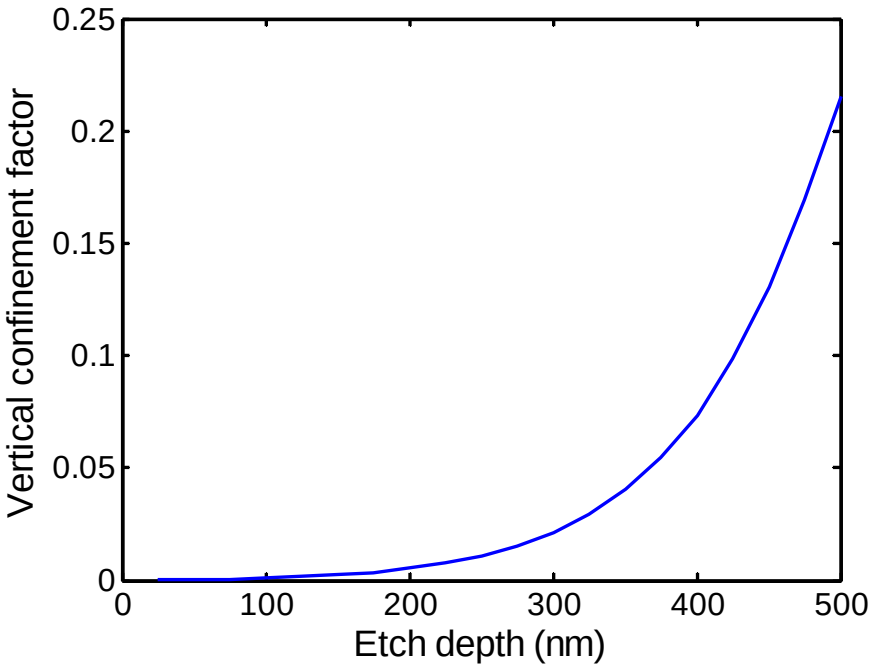

Figure 3.6: The vertical confinement factor as a function of the etch depth

Figure 3.5 shows the epitaxial wafer index profile and the mode distribution in the vertical direction. The modal profile is a little bit asymmetric relative to the position of the quantum well region since the upper cladding layer of the SCH structure is only about 500 nm thick. This also implies that the metal contact will introduce a small amount of absorption loss for the laser. As we mentioned before, this is the design compromise we have to take. It is clear that the etch depth and the modal profile will determine how much of the optical mode interacts with the photonic crystal, as shown in Fig. 3.5. We can also calculate the effective refractive index in the wafer plane $n_{eff} = 3.26$. Figure 3.6 shows the vertical confinement factor as a function of the etch depth. The vertical confinement factor is very sensitive to the etch depth in the range of 200 nm–500 nm. Thus the etch depth needs to be accurately controlled in this range.

3.4.2 Photonic crystal lattice constants

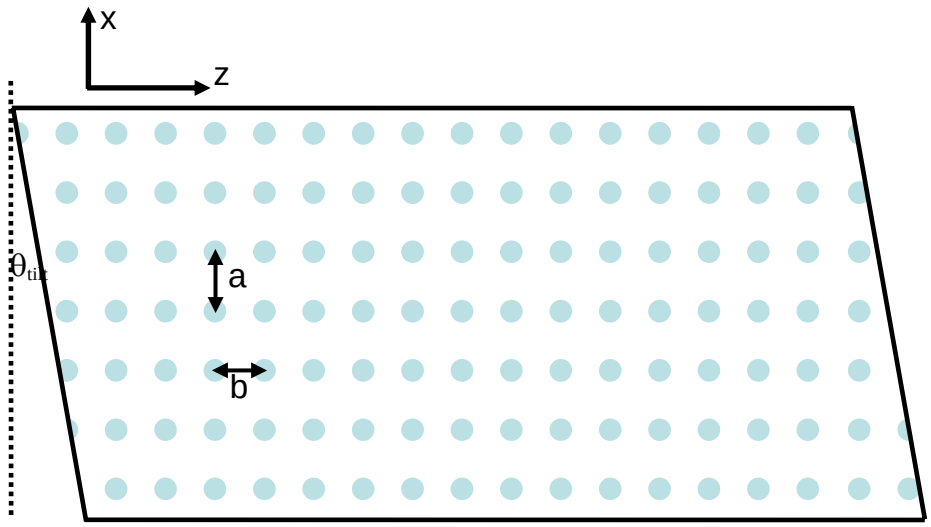

Figure 3.7: Schematic of a two-dimensional photonic crystal Bragg laser in the wafer plane. *a* is the transverse lattice constant, *b* is the longitudinal lattice constant, and θ_{tilt} is the facet tilt angle.

Using Eq. (1.25)–(1.29), we can design the photonic crystal Bragg structure. Figure 3.7 shows the photonic crystal structure in the wafer plane. It consists of a rectangular lattice array of polymer filled holes. *a* is the transverse lattice constant, *b* is the longitudinal lattice constant, and θ_{tilt} is the facet tilt angle. Here, we briefly review the basic concepts developed in Chapter 1. In the wafer plane (x-z), an optical mode that satisfies both transverse and longitudinal Bragg resonance conditions will be confined due to the Bragg reflections. This Bragg condition can be expressed as

$$k_x = l\frac{\pi}{a}, k_z = m\frac{\pi}{b} \quad (l \neq 0,\ j \neq 0), \tag{3.15}$$

where k_x is the transverse wavevector, k_z is the longitudinal wavevector, and *l*, *m* are the orders of the grating. Because the vertical wavevector k_y is determined by the wafer

epitaxial layer structure, k_x and k_z satisfy the dispersion relation

$$k_x^2 + k_z^2 = n_{eff}^2 k_0^2 . \tag{3.16}$$

Using Eq. (2.1) and (2.2), the resonance modal angle θ_{res} is given by

$$\theta_{res} = \cos^{-1}(k_z / n_{eff} k_0) = \sin^{-1}(k_x / n_{eff} k_0) = \tan^{-1}(k_x / k_z) . \tag{3.17}$$

The key here is to select a suitable resonance angle. If the resonance modal angle is small, we can not effectively discriminate against gain-guided modes; while if the modal angle is big, we need a strong grating to suppress radiation losses, and it is difficult for the fabrication. For practical designs, we choose the resonance modal angle in the range of 10^o to 20^o [13]. After the resonance angle is determined, we can calculate the transverse and longitudinal lattice constants using Eq. (3.15) and Eq. (3.16). Due to the fabrication limitation, we use the first order Bragg reflection in the transverse direction and the second order Bragg reflection in the longitudinal direction.

Using these design guidelines, we come up with the following design parameters for the photonic crystal lattice with a targeting wavelength of 1.55 μm

$$n_{eff} = 3.26 , \ \lambda = 1.55 \ \mu\text{m} \tag{3.18}$$

$$a = 1 \ \mu\text{m}, \ k_x = \pi / a = 3.14 / \mu m \tag{3.19}$$

$$b = 490 \ \text{nm}, \ k_z = 2\pi / b = 12.82 / \mu m \tag{3.20}$$

$$\theta_{res} = 13.8^o . \tag{3.21}$$

In our design, we have the facet tilt angle same as the resonance angle

$$\theta_{tilt} = 13.8^o . \tag{3.22}$$

3.4.3 Photonic crystal etch depths

In the next step, we will determine the etch depth and the hole radius of the photonic crystal. Both of them are relatedto the coupling coefficients of the photonic crystal and determine the field distribution inside the laser. In order to solve this problem, we use the two-dimensional coupled mode analysis developed in Chapter 1. Using Eq. (1.25)–(1.29), we write the index distribution of the photonic crystal as

$$\Delta\varepsilon(x,z)=\sum_{l,m}\Delta\varepsilon_{l,m}\exp(iK_{l,m}\cdot\vec{r}) \tag{3.23}$$

$$K_{l,m}=l\frac{2\pi}{a}\vec{x}+m\frac{2\pi}{b}\vec{z} \tag{3.24}$$

$$\Delta\varepsilon_{l,m}=\frac{1}{ab}\int_{-b/2}^{b/2}\int_{-a/2}^{a/2}\Delta\varepsilon(x,z)\exp(-iK_{l,m}\cdot\vec{r})dxdz\,. \tag{3.25}$$

For a rectangular lattice, inside a unit cell, we have

$$\Delta\varepsilon(x,z)=\begin{cases}\Delta\varepsilon & |r|\le r_h\\ 0 & else\end{cases}\qquad r_h \text{ is the radius of the hole} \tag{3.26}$$

$$\Delta\varepsilon_{l,m}=\frac{\Delta\varepsilon}{ab}\int_{hole}\exp(iK_{l,m}\cdot\vec{r})dxdz=2\Delta\varepsilon\frac{\pi r_h^{\,2}}{ab}\frac{J_1(Kr_h)}{Kr_h} \tag{3.27}$$

$$K=|K_{l,m}|=\sqrt{\left(l\frac{2\pi}{a}\right)^2+\left(m\frac{2\pi}{b}\right)^2}\,. \tag{3.28}$$

We can focus on the first order Bragg reflection in the transverse direction and the second order Bragg reflection in the longitudinal direction because other order combinations of the Bragg reflections correspond to the wavelengths far away from the gain spectrum peak. We have $\varepsilon_{1,0}$, $\varepsilon_{-1,0}$, $\varepsilon_{0,2}$, $\varepsilon_{0,-2}$, $\varepsilon_{1,2}$, $\varepsilon_{1,-2}$, $\varepsilon_{-1,2}$, and $\varepsilon_{-1,-2}$ as the index perturbation terms. The components $\varepsilon_{1,2}$, $\varepsilon_{1,-2}$, $\varepsilon_{-1,2}$, and $\varepsilon_{-1,-2}$ will cause the cross coupling between the transverse direction and the longitudinal direction. If we

ignore these components, we can get a simplified model similar to Eq. (3.12)–(3.14). We then have the expressions for the transverse and longitudinal coupling coefficients, using Eq. (1.6) and (1.33)

$$\kappa_x = \frac{k_0^{\,2}}{2k_x}\Delta\varepsilon_{1,0}\Gamma\,,\quad \kappa_z = \frac{k_0^{\,2}}{2k_z}\Delta\varepsilon_{0,2}\Gamma\,. \tag{3.29}$$

Using Eq. (3.27)–(3.29) and the results of Fig. 3.5, we can calculate the transverse and longitudinal coupling coefficients of the photonic crystal. The laser usually has a width W of 100 μm and a length L of 500 μm. The calculation results of $\kappa_x W$ and $\kappa_z L$ are shown in Fig. 3.8 and Fig. 3.9.

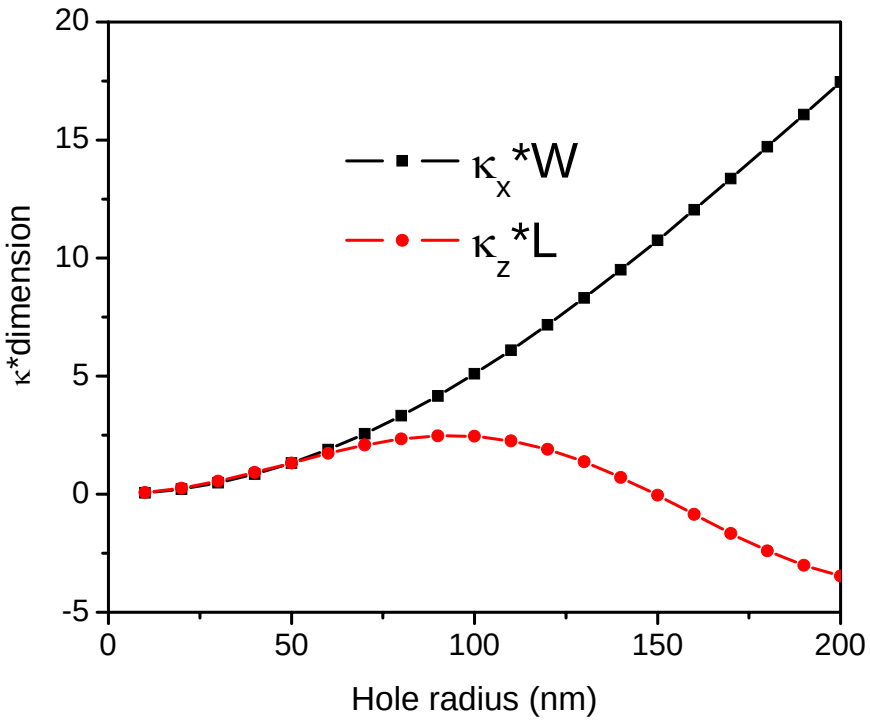

Figure 3.8: $\kappa_x W$ and $\kappa_z L$ as a function of the radius of etched holes with the etch depth of 350 nm

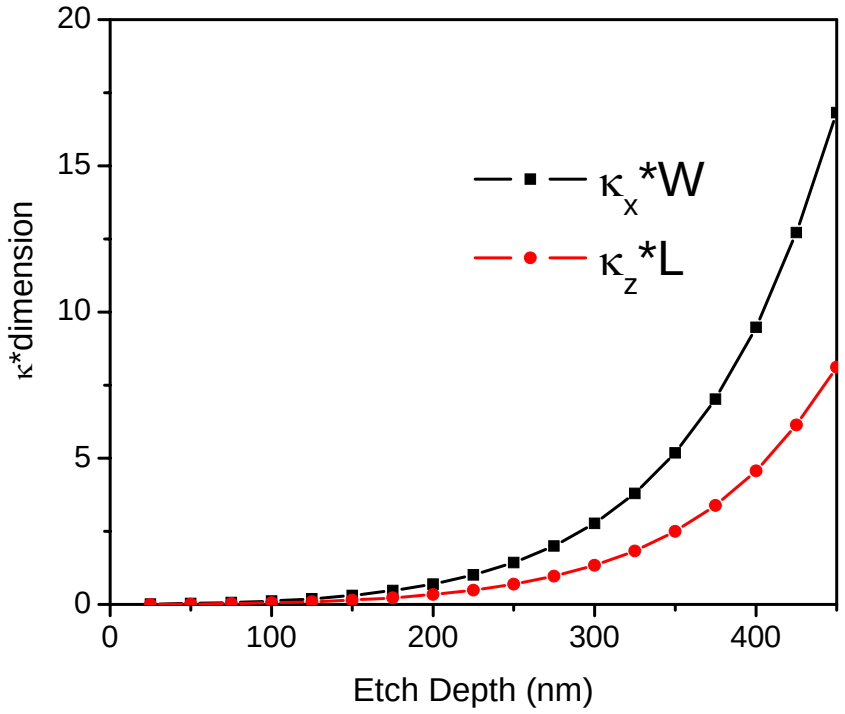

Figure 3.9: $\kappa_x W$ and $\kappa_z L$ as a function of the etch depth with 100 nm etched hole radius

The products of the coupling coefficients and the device dimensions, $\kappa_x W$ and $\kappa_z L$, are important for the design of the photonic crystal. If $\kappa_x W$ and $\kappa_z L$ are too small, the transverse confinement and the longitudinal feedback are not strong enough to support the lasing action with a low threshold. If $\kappa_x W$ and $\kappa_z L$ are too large, high order spatial modes supported by the photonic crystal can lase and spatial hole burning can occur. For practical designs, we have the condition

$$2 \le \kappa_x W, \kappa_z L \le 10 . \tag{3.30}$$

Due to the fabrication limitation, it is not practical to design the holes with the radius smaller than 20 nm or larger than 200 nm. We calculate the $|\kappa_x W|$ and $|\kappa_z L|$ product as a function of the hole radius in Fig. 3.8, assuming the etch depth is 350 nm. It is clear that the $|\kappa_x W|$ product increases as the etched hole radius increases, while the $|\kappa_z L|$ product

peaks around r_h = 100 nm and r_h = 200 nm. In order to obtain a large longitudinal coupling constant and a moderate transverse coupling constant, we choose the hole radius to be 100 nm.

In Fig. 3.9, we calculate the $\kappa_x W$ and $\kappa_z L$ products as a function of the etch depth with the etched hole radius of 100 nm. Both of them increase as the etch depth increases. In order to satisfy Eq. (3.30), we choose the etch depth to be in the range of 250 nm to 400 nm.

Chapter 4

Fabrication of photonic crystal Bragg lasers

4.1 Introduction

The challenge in the fabrication of two dimensional photonic crystal Bragg lasers in III-V compound semiconductor materials includes highly accurate electron-beam lithography, high quality dry etching techniques, and high quality metal contacts [47]. In our design, a single laser device has a relatively large area of about 0.5 mm x 0.1 mm consisting of about one hundred thousand holes each with a radius of only 100 nm. The large difference in scale between the device area and the grating feature size (i.e., the hole area), nearly 6 orders of magnitude, presents a fundamental challenge to the fabrication process.

The fabrication process can be roughly divided into lithography, etching, planarization, metallization, and packing. First, the photonic crystal pattern is defined by the electron beam lithography. Electron beam lithography is flexible for different designs and provides high resolution features, in comparison to the conventional UV photolithography [48, 49]. In the next step, the photonic crystal is transferred to a dielectric hard mask and then to the semiconductor surface. The etched holes in the semiconductor are then planarized with polymer in order to prevent the metal contact from falling into etched holes. After this, we thermally evaporate electrical contacts on the top and bottom side of the device. Finally, a single device is cleaved and packaged on a C-mount. The whole fabrication process is summarized in Fig. 4.1.

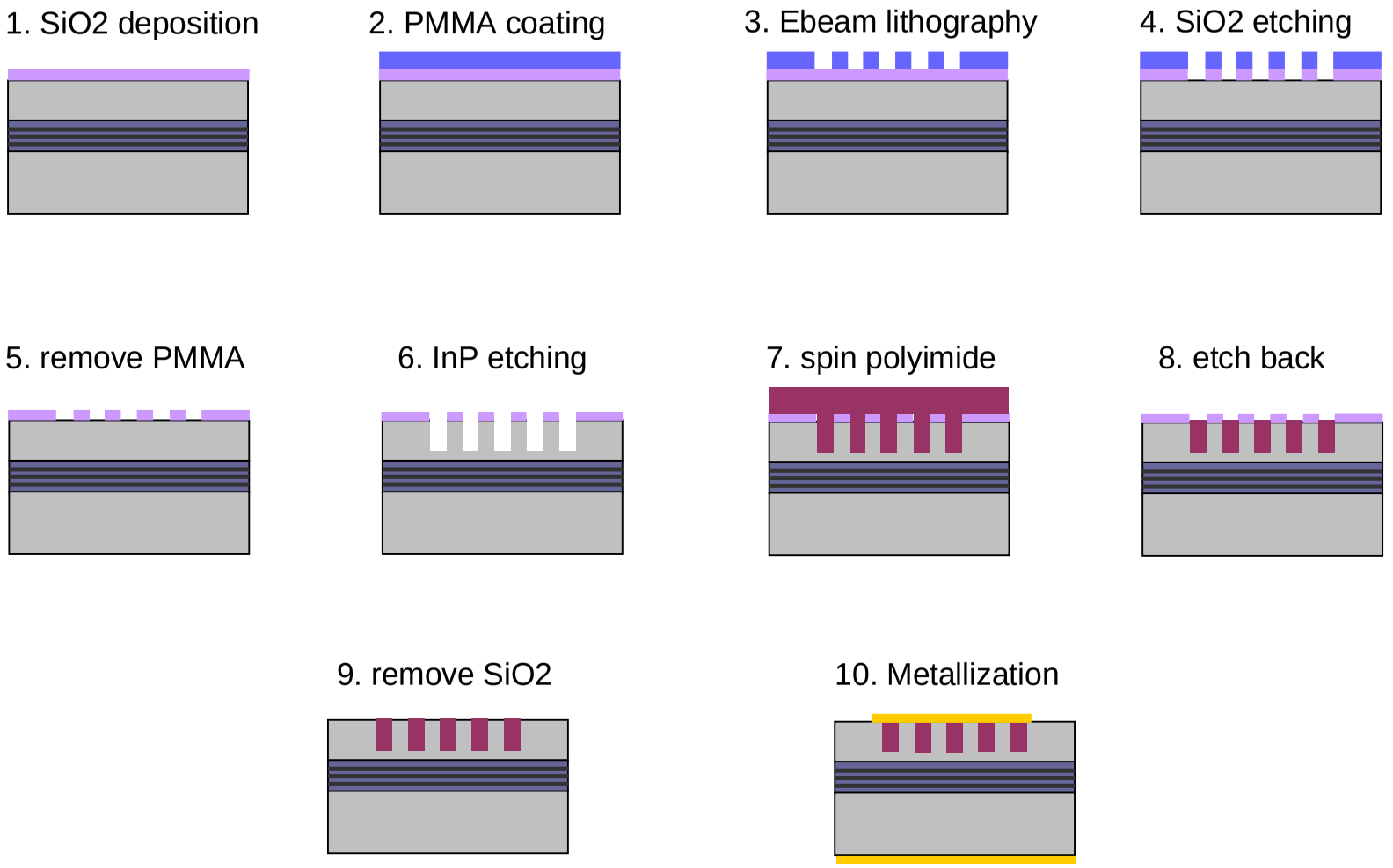

Figure 4.1: Fabrication process flow

4.2 Electron beam lithography

We start the fabrication by depositing a 120 nm thick SiO2 layer on the top of the semiconductor wafer by plasma enhanced chemical vapor deposition (PECVD). A suitable size semiconductor chip is then cleaved from the wafer. Before we spin the ebeam resist for the chip, we need to thoroughly clean the chip using acetone and IPA (isopropanol). Then, a 250 nm 495 K C4 PMMA (Microchem) resist layer is spun on the substrate at 4000 rpm and the chip is baked on a hotplate at 180 ºC for 3 minutes. We expose the PMMA resist in a Leica Microsystems EBPG 5000+ direct electron beam writer at an accelerating voltage of 100 kV and a beam current of 3.9 nA. Development of the patterned PMMA film is carried out in a solution of 1:3 MIBK (methyl-isobutyl ketone) : IPA for 60 seconds.

Photonic crystal Bragg lasers require highly uniform patterns defined by electron beam lithography over a large area, such that the holes for a single device should be nearly identical. A non-uniform index perturbation in our structures, which can be caused by the size variation of small holes, results in undesired chirp and variation in the grating period. Proximity effect correction in the electron beam lithography is required to obtain the desired uniformity [50, 51].

Proximity effect refers to the dependence of the actual electron beam exposure dosage on the density of local features, and it has been the major problem for obtaining fine resolution and large-area uniformity in electron beam lithography. The incident electrons experience forward and backward scattering in the resist. In addition to exposing the desired areas, the scattered electrons can also expose the areas beyond the designed patterns. A Monte Carlo simulation of this scattering of 100 kV electrons in the material stack used in the fabrication process is shown in Fig. 4.2, and illustrates that the scattered

electrons can expose the PMMA “from below” laterally outside of the beam spot. This deleterious scattering has a slight impact on isolated patterns, such as the holes near the edges of our structure. However, for dense patterns, such as the holes in the center region of our structure, this undesired exposure can be significant. Therefore, if a constant electron dosage is used over the pattern area, the actual, effective exposure dosage of the holes around the center will differ from that at the edge, manifesting in pattern distortion due to the proximity effect.

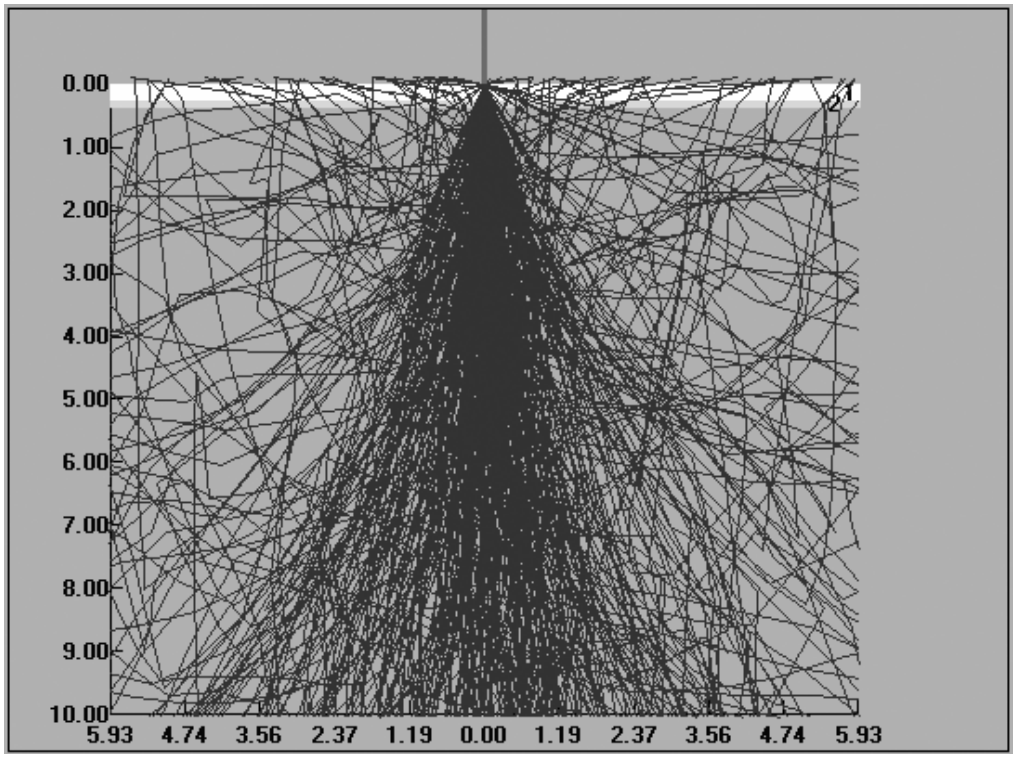

Figure 4.2: Monte Carlo simulation of 100 kV electrons scattering in the material stack. The top (white) layer is 250 nm of PMMA. The second layer (light grey) is 120 nm SiO_2, and the substrate (dark grey) is InP. The ordinate is the radial distance in μm from the incident beam spot, and the abscissa is penetration depth in μm into the material.

To characterize the extent of the proximity effect and to determine the degree of proximity effect correction required, we quantitatively compare the feature sizes at

various regions of the pattern with various degrees of correction. Our test pattern consists of a 96 μm x 96 μm square array of holes with a designed radius of 100 nm spaced at a period of 480 nm. The size of the test pattern is sufficient in modeling the lithography of the actual photonic crystal Bragg lasers which consists of a rectangular array of holes of the same radius but over a much larger area of ~ 500 μm x 100 μm.

The calculations to determine the dose variations required to compensate for the proximity effect fall into three stages. The first stage is a Monte Carlo simulation of the scattering of the incident electron beam as it passes through the various layers of the material "stack." We used a commercial numerical simulation package for this calculation called SCELETON (SCattering of ELECTrONs in matter) by PDF Solutions Aiss division (licensed by Synopsys Inc., to work with PROXECCO and CATS). This program takes a user defined resist substrate multilayer "stack" of components defined in a materials database and traces a specified number of electrons in the material. Monte Carlo simulation is carried out using a single scattering model, where the electron trajectory is followed through a series of scattering events in the resist/substrate stack. Elastic scattering events are described using the screened Rutherford formula. Energy dissipation due to inelastic scattering is modeled by Bethe's energy loss formula in the continuously slowing down approximation (CSDA). Typical calculation time for the stack used in this paper was 11 hours on a Linux-based Xeon processor system in which $1x10^7$ electrons were traced. The resulting calculated radial energy density distribution (point spread) can be used directly as input for PROXECCO.

The Monte Carlo simulation results are used as input for the program PARAPROX, which determined what is called the proximity function. The mathematical algorithm of PROXECCO uses a fast variant of the deconvolution method which describes the physics behind the proximity effect very well. The accuracy and efficiency is based on a separate treatment of pattern and correction. PROXECCO performs a determination of this proximity function in a plane of the resist specified by the user, and then calculates the

correction factors, or conditional frequency assignments (CFA), to apply when fracturing the pattern data. A particularly useful feature of this approach is that it treats the material stack and pattern data independently, which vastly improves both the flexibility of application and speed of computation.

The CFA data file is used by the fracturing program (CATS by Transcription Enterprises, now licensed by Synopsys, Inc.) by convolution with the proximity parameter file to prepare the pattern data for exposure with variable doses such that the effective dose over the pattern is uniform. The number of conditional frequency assignments determines how fine the variation of the dose is. The number of CFAs to use is something to be determined experimentally, as too few factors result in under-correction and too many factors result in excess computational and exposure time.

4.2.1 Electron beam lithography without proximity effect correction

We first characterize the electron beam lithography without any proximity effect correction. We find that at an electron beam dosage of 700 $\mu C/cm^2$, while the radius of the holes in the central region is closest to the designed value, the holes at the edge of the pattern are under-exposed, as shown in Fig. 4.3. However, when the holes near the edge are sufficiently exposed and closest to the designed size, the central region is over-exposed.

Figure 4.4 shows the relative error in the hole sizes as a function of the distance from the center of the pattern when the holes at the edges are closest to the designed size and are sufficiently exposed such that no PMMA remained. The relative error (R.E.) is defined as

$$R.E. = \left| \frac{r_d - r_c}{r_c} \right| \tag{4.1}$$

where r_c is the measured hole radius at the center of the pattern and r_d is the measured

hole radius at a particular distance from the center. The solid line in Fig. 4.4 shows the R.E. for the lithography without proximity effect correction with a dosage of 750 μC/cm^2. The sizes of the holes vary up to 10% over the test pattern area. This variation would be sufficient to result in chirped gratings that would modify the spectral properties of the photonic crystal lasers.

(a)

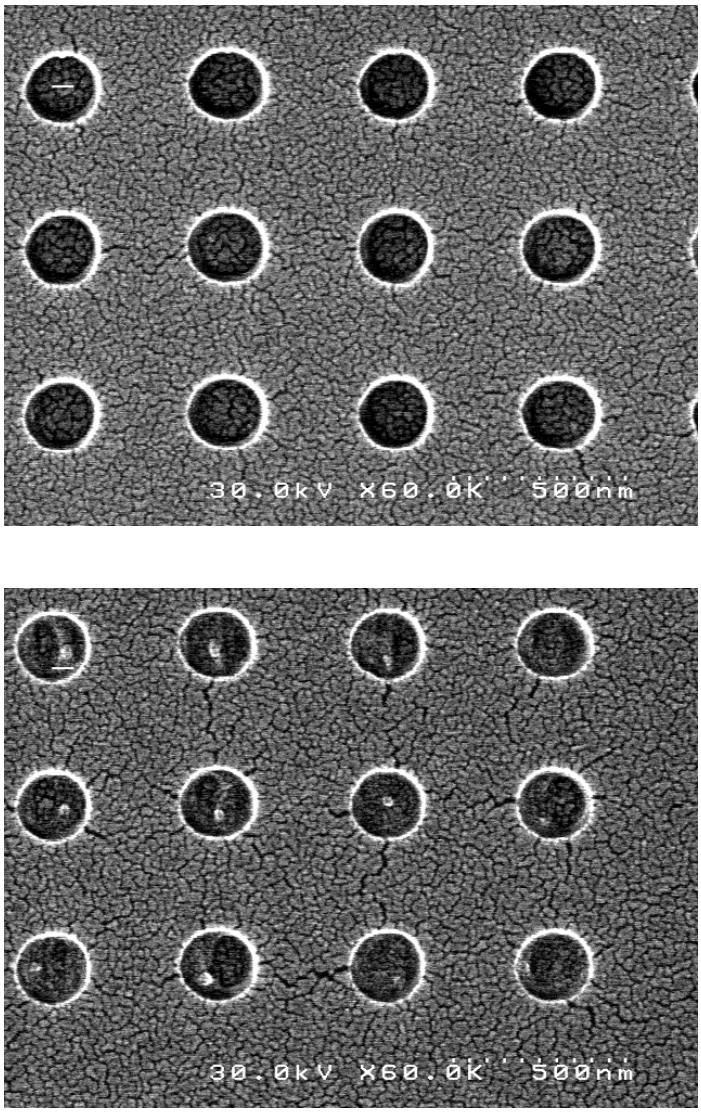

Figure 4.3: Scanning electron micrographs of the PMMA resist after uncorrected electron-beam lithography at a dosage of 700 μc/cm^2. At this dosage, the radius of the holes in the center region is closest to the designed value. (a) The holes at the center of the test pattern. (b) The holes at the edge of the test pattern

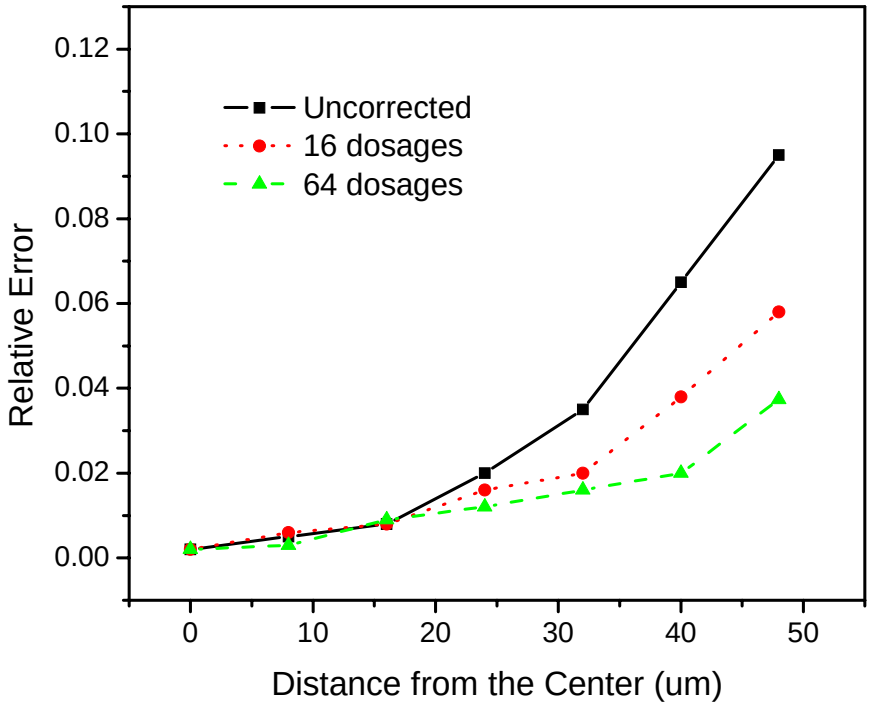

Figure 4.4: The relative error in the hole radius as a function of the distance from the center of the pattern for different degrees of proximity effect correction. The solid line is for the uncorrected lithography with a dosage of 750 μc/cm^2. The dotted line is for the corrected lithography using a set of 16 dosages centered at 260 μc/cm^2. The dashed line is for the corrected lithography using a set of 64 dosages centered at 230 μc/cm^2.

4.2.2 Electron beam lithography with proximity effect correction

To compensate for the proximity effect, we use CATS with proximity correction, as described above, which fractures the pattern into a large number of divisions and assigns one of the defined dosages to each division. The required dosage is calculated by the program from the pattern density while accounting for the resist and substrate electron scattering properties. We repeat the electron beam lithography with sets of 16 and 64 dosages in the proximity effect correction program.

The dashed and dotted lines in Figure 4.4 show the relative hole size errors for the two

cases. Again, the relative error is taken at the dosage range where the holes near the edges of pattern are closest to the designed size and are sufficiently exposed. As shown in Fig. 4.4, a set of 16 dosages result in a maximum relative size error of 6% at the edge region of the pattern. 64 dosages are required to limit the error to less than 5%, which is acceptable for our 2DBG laser designs. Therefore, for the fabrication of the photonic crystal Bragg lasers, we use 64 dosages in the proximity effect correction code to obtain sufficiently uniform patterns over the large area of the device.

4.3 Reactive ion etching

After the PMMA development, the photonic crystal patterns are transferred to the SiO_2 layer by reactive ion etching (RIE) using CHF_3 plasma [52]. This is because we could not directly use the PMMA layer as a mask to etch InP. In this SiO_2 etch process, the PMMA layer is a soft mask. So it is important to prevent the polymer redeposition. As shown in Fig. 4.5, there are a lot of particles in the etched region. This is mainly due to the polymer redeposition. These particles in the etched region would eventually cause the roughness of the photonic crystal pattern during the following fabrication process. The key here is to optimize the chamber pressure during the etching so that the etch product can be quickly removed from the main chamber. Figure 4.6 shows several scanning electron micro-spectroscopy (SEM) images of the etch results using an optimized etch recipe. The etched region is clean in both images. In the optimized recipe, we use a CHF_3 flow rate of 20 sccm, chamber pressure of 60 mTorr, and RF power of 110 W. The plasma DC self-bias is about 455 V, and the etch rate is around 40 nm/min.

The SiO_2 layer then serves as a hard mask to etch the semiconductor surface photonic crystal using an ICP-RIE with HI/Ar chemistry [53]. In this etch process, we do not have the redeposition problem since the SiO_2 layer is a hard mask. However, we still need to balance the chemical etching and the physical etching in order to obtain a smooth surface

and a straight sidewall. Figure 4.7 shows the etch results using both the nonoptimized and the optimized etch recipe. In the optimized etch recipe, the HI/Ar gas flow is 10/6 sccm, the chamber pressure is 5 mTorr, and the ICP and RF electrodes are driven with 650 W and 30 W, respectively. The plasma DC self-bias is around 104 V, and the etch rate is about 250 nm/min.

(a)

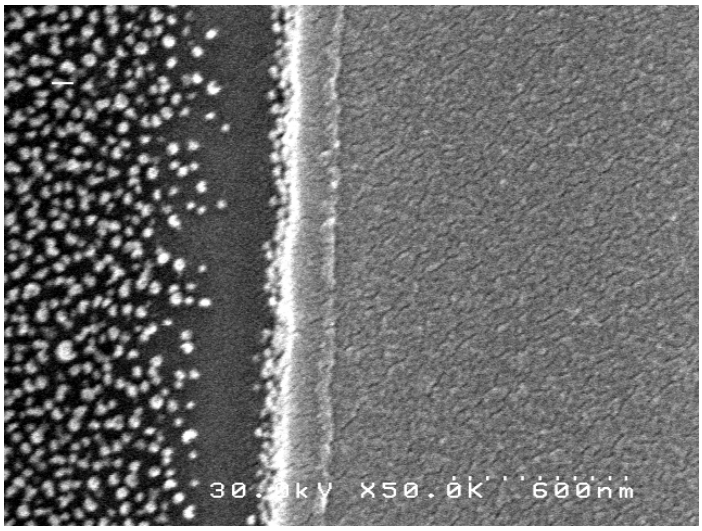

(b)

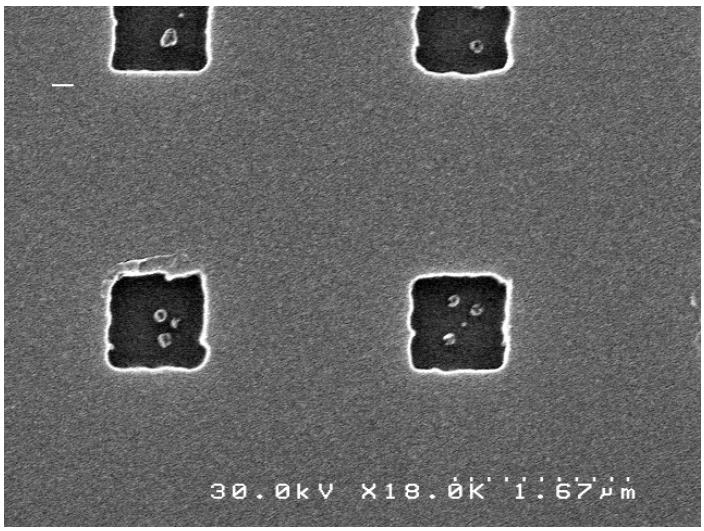

Figure 4.5: SEM images of non-optimized SiO_2 etch

(a)

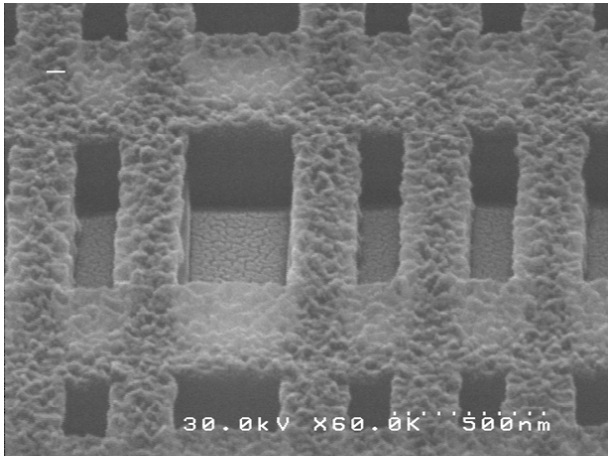

(b)

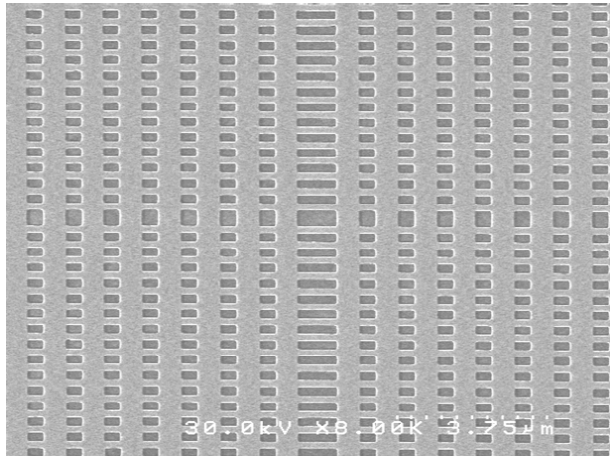

Figure 4.6: SEM images of SiO2 etch test with the improved etch recipe (a) with remaining PMMA (b) without PMMA

(a)

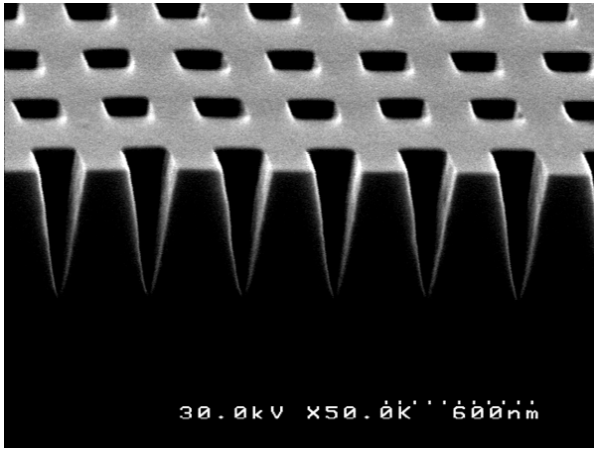

(b)

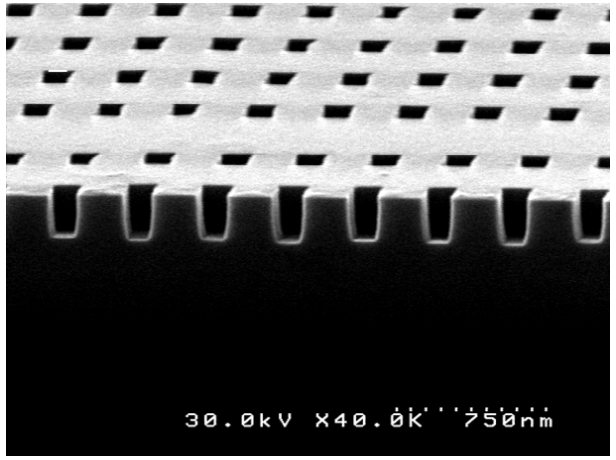

Figure 4.7: SEM images of InP etch test (a) non-optimized (b) optimized

4.4 Planarization and metallization

After the etch of InP, the remaining SiO_2 layer is about 80 nm thick. If we remove this leftover silica layer and directly deposit the metal contact at this stage, some of the metal will fall into the etched holes. This part of the metal will be very close to the quantum well region and introduce a lot of absorption losses. In order to prevent this, we coat the devices with a 2 μm thick polyimide (PI-2562, HD Microsystems) planarization layer. The polyimide is subsequently etched back to the SiO2 layer by an ICP-RIE using pure oxygen. Since the etch depth needs to be accurately controlled, the etch rate should be small. In the optimized etch recipe, the O_2 gas flow is 30 sccm, the chamber pressure is 10 mTorr, and the ICP and RF electrodes are driven with 200 W and 20 W, respectively. The plasma DC self-bias is around 200 V, and the etch rate is about 200 nm/min.

During this process, the sacrificial SiO_2 layer provides additional 80 nm tolerance for the polyimide etch-back process. After the etch-back, we strip off the remaining SiO_2 in buffered hydrofluoric (HF) acid solution, creating a polyimide post inside each etched semiconductor hole. In contrast to the regular planarization methods, we can obtain a clean semiconductor surface without any polymer residue due to the SiO2 isolation layer between the semiconductor and the polymer. Figure 4.8 shows several SEM images of this planarization process.

Next, the p-side electrical contact is deposited using a standard lift-off process. A 1.8 μm thick layer of 1813 resist (Microposit) is spun on and exposed photolithographically. The p-side contact, Cr/AuZn/Au 2 nm/6 nm/250 nm, is thermally evaporated, covering the photoresist and the areas where the photoresist has been cleared. During the actual lifting-off, the photoresist under the metal layer is removed with acetone, taking the metal with it. The chip is then mechanically thinned to about 100 μm thick, and the n-side contact, Cr/AuGe/Au 2 nm/6 nm/250 nm, is evaporated. Finally, the laser bars are

cleaved to lengths of about 500 μm, and the facets are left uncoated. Figure 4.9 illustrates the cross section of the laser after we put down the p-side electrode.

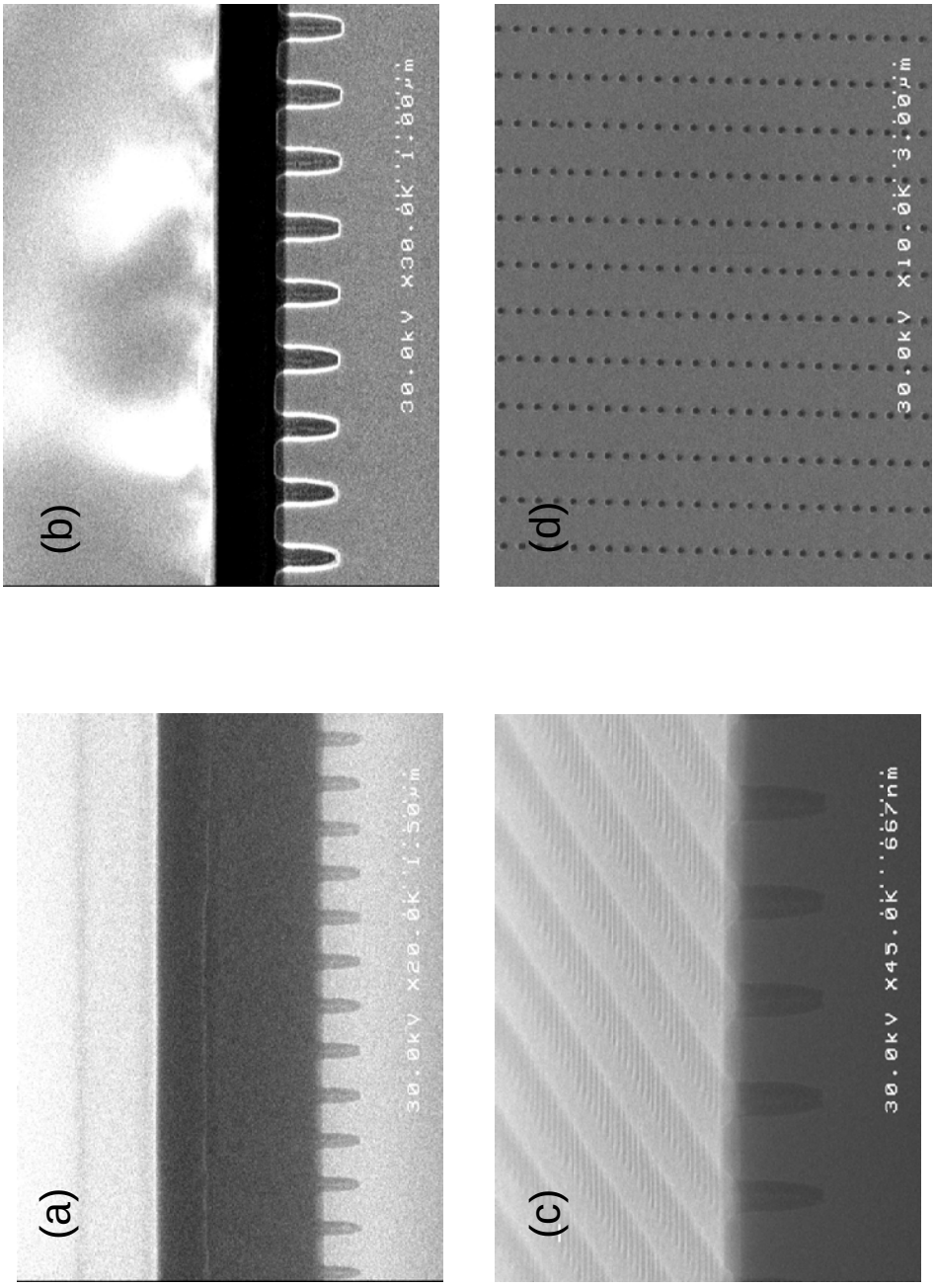

Figure 4.8: (a) spin on the polyimide (b) etch back the polyimide (c) etch to the SiO2 layer (d) the planarized sample

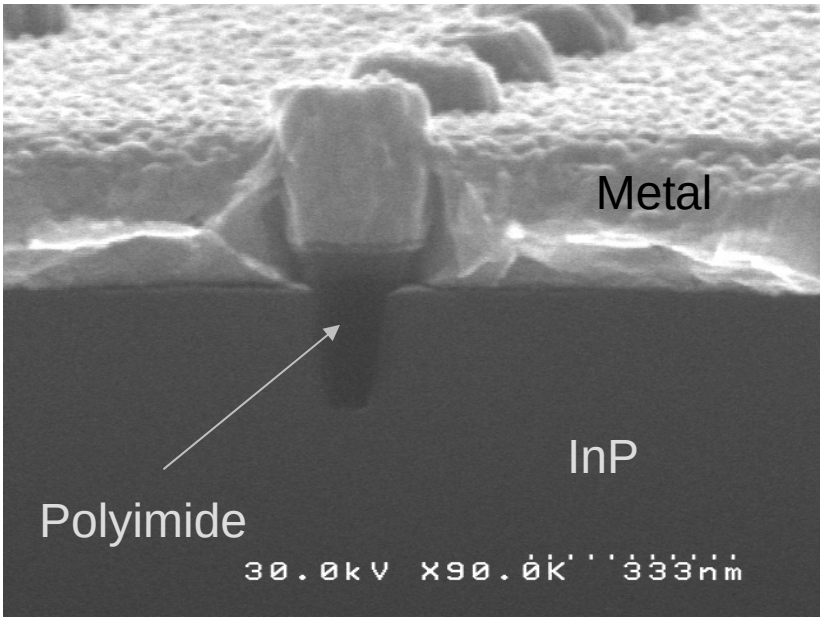

Figure 4.9: SEM image of the cross section of the laser after metallization

Chapter 5

Characterization of photonic crystal Bragg lasers

5.1 Introduction

In this chapter, we describe the characterization results of electrically pumped, large-area, edge emitting photonic crystal Bragg lasers with angled facets in the InGaAsP/InP semiconductor material at low and room temperatures. At low temperature (140 K to 180 K), semiconductor materials have higher optical gain due to the reduced rate of non-radiative, thermal transitions [3]. Thus it is easy to obtain the continuous wave (CW) operation with a relatively low lasing threshold at low temperature. At room temperature, we first try pulsed pumping without active cooling since we do not have thermal problems with the pulsed operation. However, under the CW room temperature operation, the laser generates a lot of heat due to the large size of the device. Thus, thermal engineering is a key factor to realize the CW room temperature operation of the PC Bragg laser.

Figure 5.1 shows two different setups for the low temperature and room temperature measurements, respectively. In Fig. 5.1(a), the laser is placed inside a cryostat to obtain the low temperature operation. We need to bond the laser to a C-mount. The inset in Fig. 5.1(a) shows the SEM image of a single laser die bonded a C-mount underneath. On the top of the laser die, the metal contact is wire bonded.

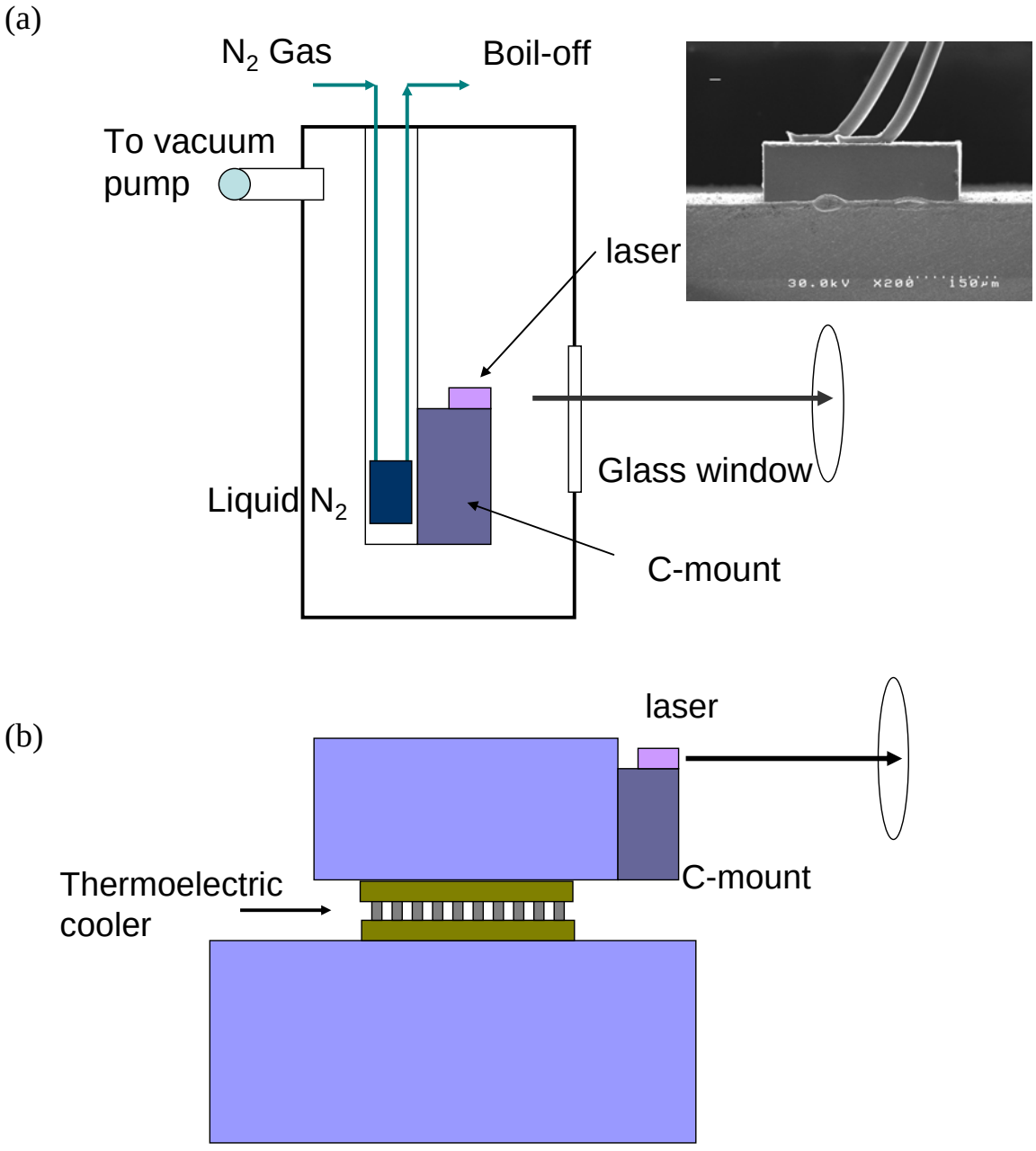

Figure 5.1: (a) Low temperature measurement setup and (b) room temperature measurement setup

In Fig. 5.1(b), a single laser or a laser bar can be bonded to the C-mount for the room temperature measurement. The top electrical contact is connected to the current source

through a metal needle. With the pulsed operation, we do not use any cooling device. With the CW operation, we have to actively cool the laser using a thermal-electric cooler (TEC), as shown in Fig 5.1(b).

For the characterization of the PC Bragg laser, we measure the output power versus the input current (L-I) curve, the optical spectrum, the near field, and the far field. From the L-I curve, we can obtain the laser threshold and the slope efficiency. From the optical spectrum, we can obtain the emission wavelength. For the near field and far field measurement, we use the setups shown in Fig. 5.2 [54]. In Fig. 5.2(a), we place a lens in front of the PC Bragg laser and put a camera at the imaging plane of the lens to measure the near field. Thus the near field is the image of the laser emitting facet. In Fig. 5.2(b), we directly put the camera in front of the laser to capture the far field image and the camera needs to be far away from the laser (> 1 mm). The far field is essentially the spatial profile of the laser output beam. We usually use an angular coordinate for the far field measurement. The full-width half-maximum (FWHM) angle is defined as the divergence angle of the laser.

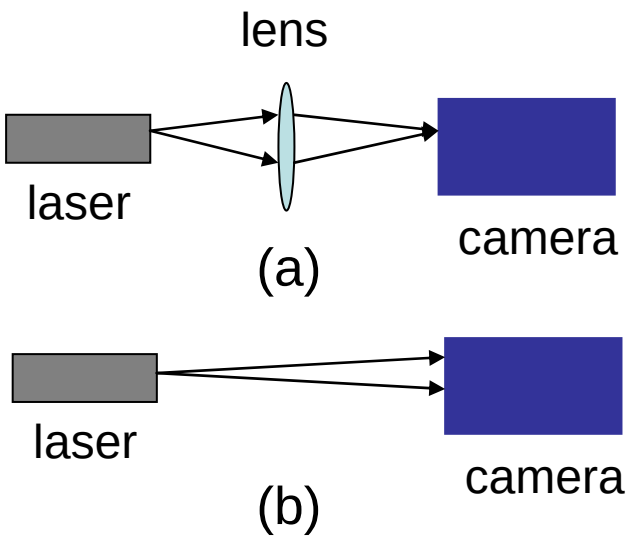

Figure 5.2: (a) The near field measurement setup and (b) the far field measurement setup

5.2 Low temperature measurement

In this section, we measure the L-I curves of the PC laser at different temperatures. We compare the laser threshold current and slope efficiency of the PC laser with those of a straight facet broad-area (BA) laser fabricated from the same wafer with the same size and under the same operating conditions. We show that the performance penalty in terms of threshold current and slope efficiency incurred by the presence of lasing in a photonic crystal mode is small. This is important for practical applications of our PC lasers. We also measure the laser spectra at different temperatures and obtain a temperature tuning sensitivity $d\lambda/dT$ of 0.09 nm/℃, which is similar to a regular distributed feedback (DFB) laser [3]. Finally, we measure the PC laser linewidth using an optical heterodyne approach [55] and show that the laser truly operates in a single mode.

The device structure is detailed in Chapter 3. We use a first order Bragg reflection (l = 1) for the transverse direction with a lattice constant of a = 1 μm, and a second order Bragg reflection (j = 2) for the longitudinal direction with a lattice constant of b = 470 nm. The design corresponds to a resonance wavelength of 1483 nm (n_{eff} is estimated to be 3.24). The metal contact width is about 100 μm and the facet tilt angle is 13.2°. The lasers are cleaved to lengths of about 450 μm and widths of about 400 μm. Each cleaved laser is then bonded to a C-mount and placed in a micro cryogenic refrigerator (MMR Tech.). We test the lasers in the temperature range of 140 K to 180 K to obtain the CW operation.

5.2.1 L-I curves and temperature tuning

The PC laser L-I curves at different temperatures are shown in Fig. 5.3(a). In the test temperature range, the threshold current varies from 47 mA to 88 mA. We optimize the measurement setup and make sure that the output light collection efficiency is the same

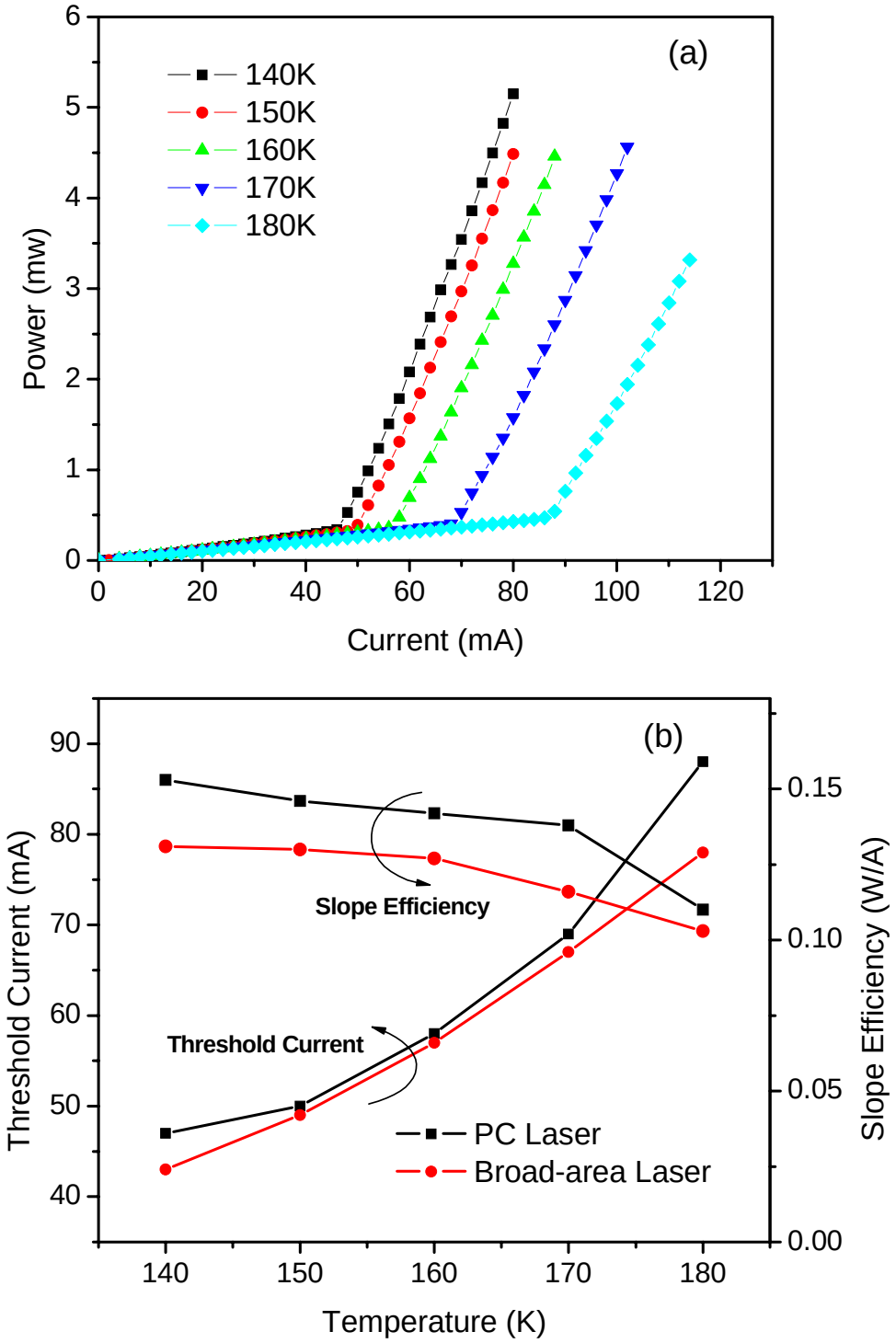

Figure 5.3: (a) L-I curves for the photonic crystal laser at different temperatures. (b) Comparison of the threshold current and slope efficiency between the photonic crystal laser and broad area laser

for different tests. Thus we can compare the threshold current and slope efficiency between the PC laser and the BA laser. The comparison results are shown in Fig. 5.3(b).

The PC laser is theoretically expected to have a lower threshold due to the gain enhancement at the band edge [56]. But the PC structure fabricated by dry etching technique causes extra losses due to the scattering and surface recombination, which lead to a higher threshold. In Fig. 5.3(b), the threshold current for the PC laser is slightly higher than the BA laser. As the temperature increases, the material gain decreases and gain peak shifts to longer wavelengths. The threshold of the BA laser is determined by the peak of the material gain spectrum and varies almost linearly with the temperature in our experiment. In contrast, the threshold of the PC laser is determined by the gain at the resonance wavelength. Thus, the threshold of the PC laser varies linearly with the temperature only when the peak of the material gain spectrum is well aligned with the resonance wavelength (150 K to 170 K). In Fig. 5.3(b), the PC laser exhibits higher slope efficiency than the BA laser despite of the extra losses induced by the PC structure. This is mainly due to the fact that the PC structure has a wide optical mode and prevents the formation of filamentation [38]. The comparison results show that our PC lasers can perform similarly to or better than the BA laser fabricated from the same material in terms of the threshold current and slope efficiency and these PC lasers are suitable for practical applications.

Figure 5.4(a) shows the lasing spectra at the pump current I = 1.6 Ith when the temperature changes from 140 K to 170 K. The side mode suppression ratios of the spectra at different temperatures are all greater than 30 dB. The lasing wavelength changes from 1483.95 nm to 1486.80 nm as the temperature changes from 140 K to 170 K. This corresponds to a temperature tuning sensitivity $d\lambda/dT$ of 0.09 nm/℃. Figure 5.4(b) compares the temperature tuning sensitivity of the lasing wavelength between the PC laser and BA laser. For the BA laser, the temperature tuning sensitivity is 0.5 nm/℃.

(a)

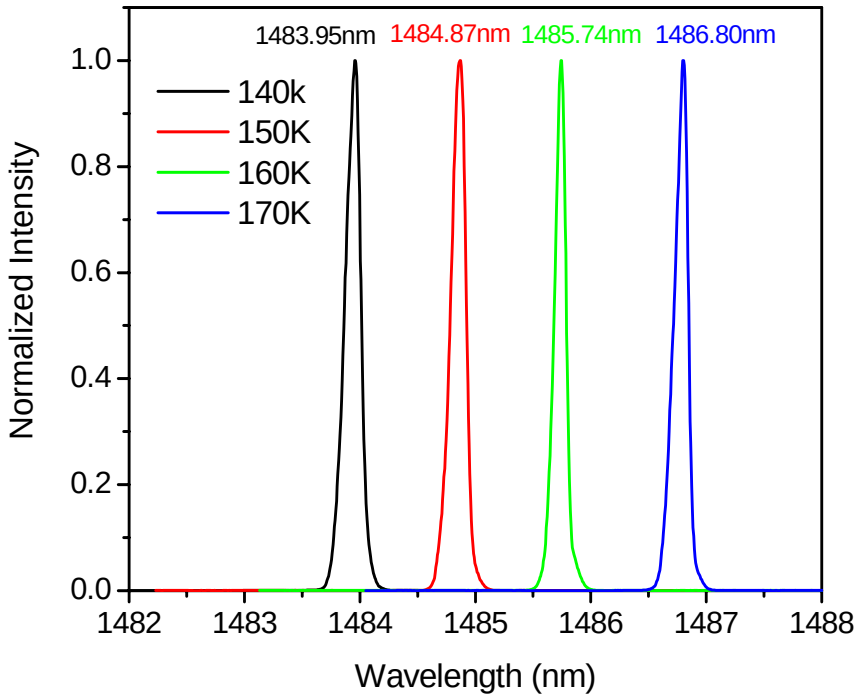

(b)

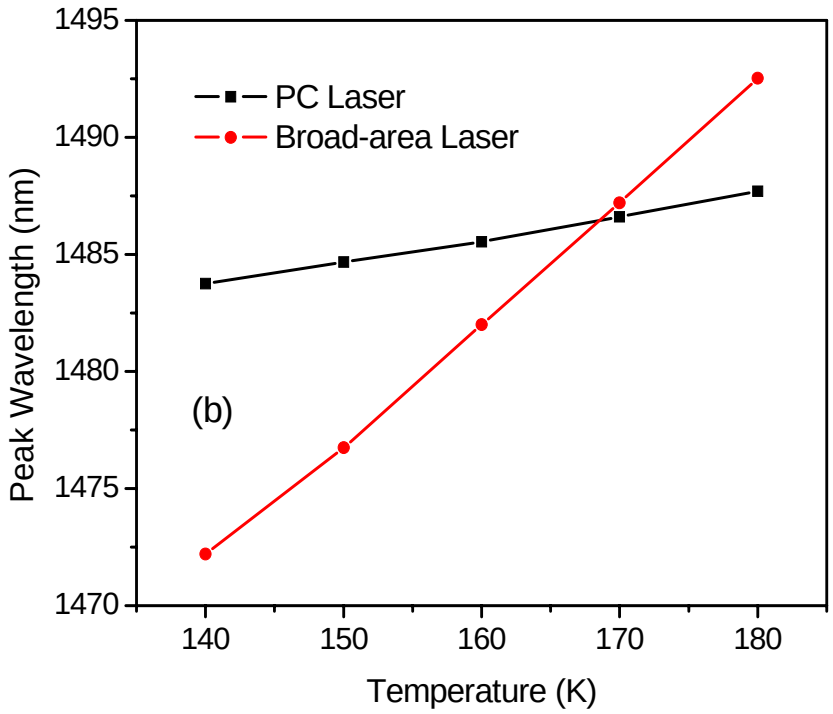

Figure 5.4: (a) Lasing spectra of the PC laser at different temperatures (1.6 Ith). (b) The laser peak wavelength as a function of the temperature for the PC laser and BA laser

When the temperature changes, there are two reasons that can lead to the change of the lasing wavelength. First, the refractive index of semiconductor materials changes; second, the gain spectrum of the semiconductor material, especially the peak position of the gain spectrum, changes. If the lasing mode is selected by the photonic crystal, the change of the lasing wavelength should only correspond to the change of the refractive index, not to the change of the material gain. For a broad area laser, it is similar to a free running oscillator. Its peak lasing wavelength always matches the peak position of the material gain spectrum as the temperature varies. In Fig. 5.4(b), it is clear that the temperature tuning sensitivity of the PC Bragg laser is different from the BA laser. This implies that the lasing mode of the PC Bragg laser is not selected by the material gain. We also compare the temperature tuning sensitivity of the PC Bragg laser with a temperature tuned DFB laser operated under similar conditions and obtain very similar results. This indicates that the lasing mode of the PC Bragg laser is indeed selected by the photonic crystal lattice.

5.2.2 Single mode operation

Figure 5.5 shows the lasing spectrum at the pump current I = 1.3 Ith and the temperature T = 150 K. The spectrum has a single lobe and the side mode suppression ratio is about 32 dB. The FWHM linewidth (3 dB linewidth) is 0.15 nm. Optical spectrum analyzers usually have limited resolution; in our case, it is 0.08 nm. Thus we are not sure if there is more than one peak inside the single lobe in Fig. 5.5. In order to determine if the laser operates in a true single mode, we have to resolve the lasing spectrum with a higher resolution.

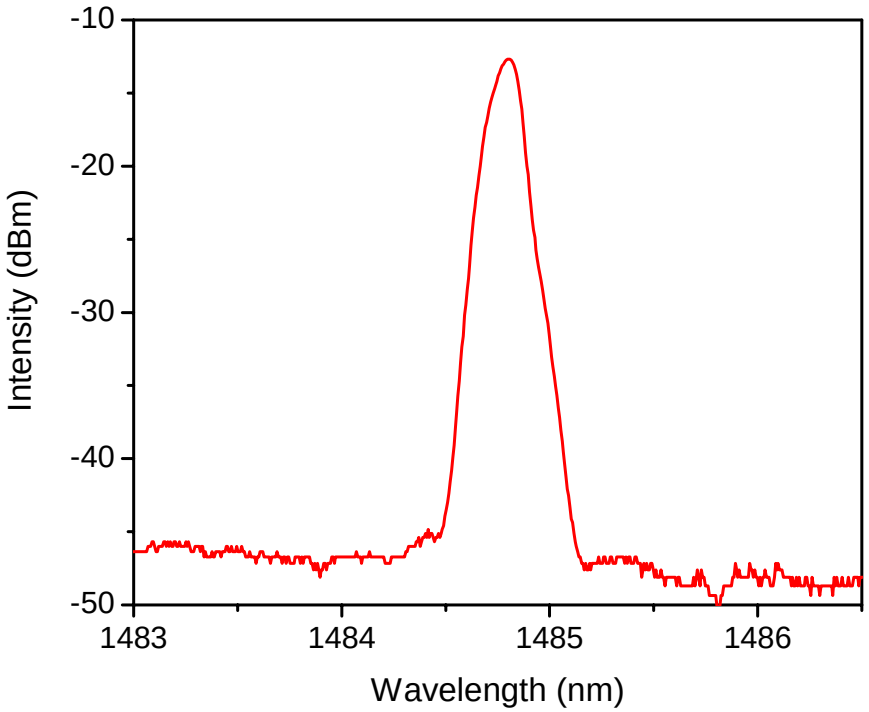

Figure 5.5: The lasing spectrum of the PC laser at 1.3 Ith (150 K)

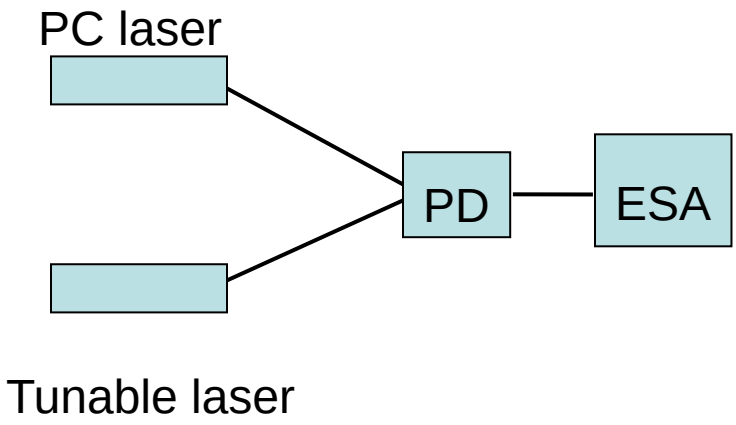

Figure 5.6: The optical heterodyne detection measurement setup

We use an optical heterodyne detection approach to resolve the fine features of the lasing spectrum, as shown in Fig. 5.6. We couple the light from the PC laser into a single mode fiber and combine it with the light from a tunable laser using a 3 dB fiber coupler.

The optical beating signal is then photodetected by a 25 GHz photodiode. The spectrum of the electrical current is measured on a 50 GHz RF spectrum analyzer. We set the wavelength of the tunable laser output light to be the same as the PC laser and sweep the wavelength in a range of 0.2 nm with a step of 0.001 nm. A single-peaked electrical spectrum is always observed during the measurement and is shown in Fig. 5.7. This proves that the PC laser operates in a single mode and the linewidth of the PC laser is estimated to be 110 MHz from Fig. 5.7 This linewidth is broader compared to a commercial DFB laser, mainly due to the large size of the laser and the temperature variation inside the refrigerator.

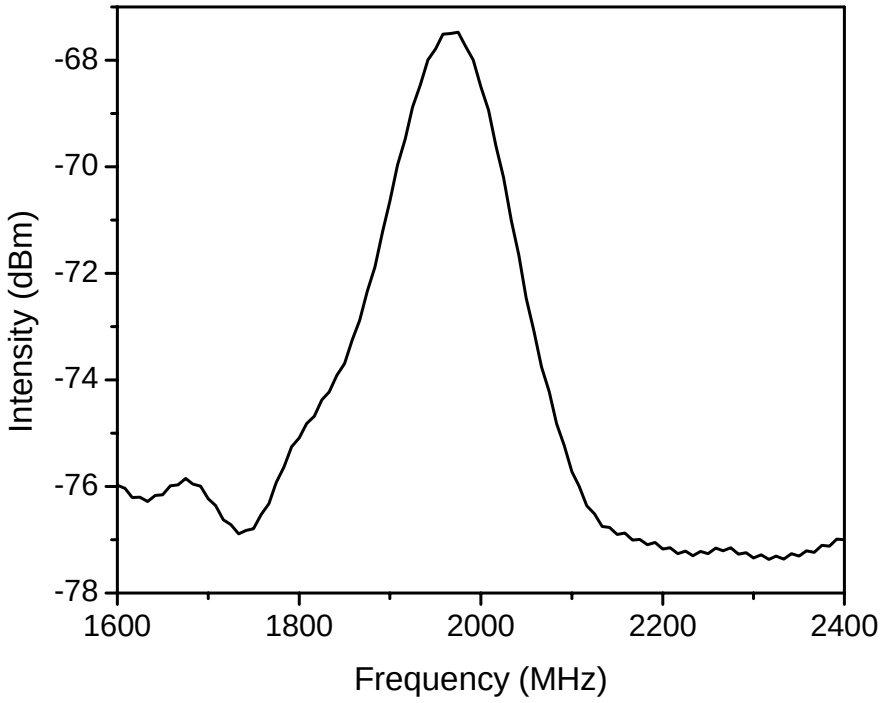

Figure 5.7: The electrical spectrum of the beating signal between the PC laser and a tunable laser

5.3 Room temperature measurement

5.3.1 Pulsed operation

At room temperature, the peak of our semiconductor material gain spectrum is around 1550 nm. Thus, we use a first order Bragg reflection (l = 1) for the transverse direction with a lattice constant of a = 1 μm and a second order Bragg reflection (j = 2) for the longitudinal direction with a lattice constant of of b = 490 nm. The hole radius is 100 nm and the etch depth is about 430 nm.The metal contact width is about 100 μm and the tilt angle is 13.8° .The laser bars are cleaved to lengths of about 480 μm and are tested in pulsed operation at room temperature with no active cooling. Current pulses with a duration of 100 ns and a period of 10 μs are injected to drive the lasers.

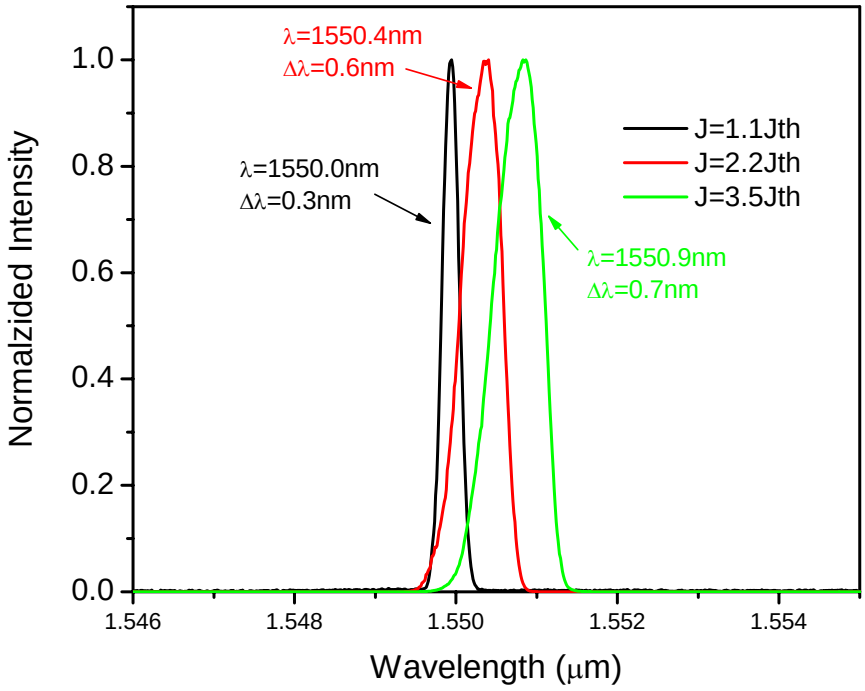

Figure 5.8: The lasing spectra at different pump currents (1.1×, 2.2×, and 3.5× threshold)

Figure 5.8 shows the lasing spectra with different pumping currents. We can still obtain

the single mode operation under pulsed operation, which shows the performance of the laser is stable. Due to pulsed excitation, the spectra are obtained under transient conditions with the attendant broadening. As the pumping current increases, the lasing spectrum shifts to longer wavelengths and the linewidth increases due to excessive heating. We can keep the single mode operation up to four times above the threshold. Further increase of the pump current is limited by the current source we have. We believe the single mode operation can be maintained higher than this pump current.

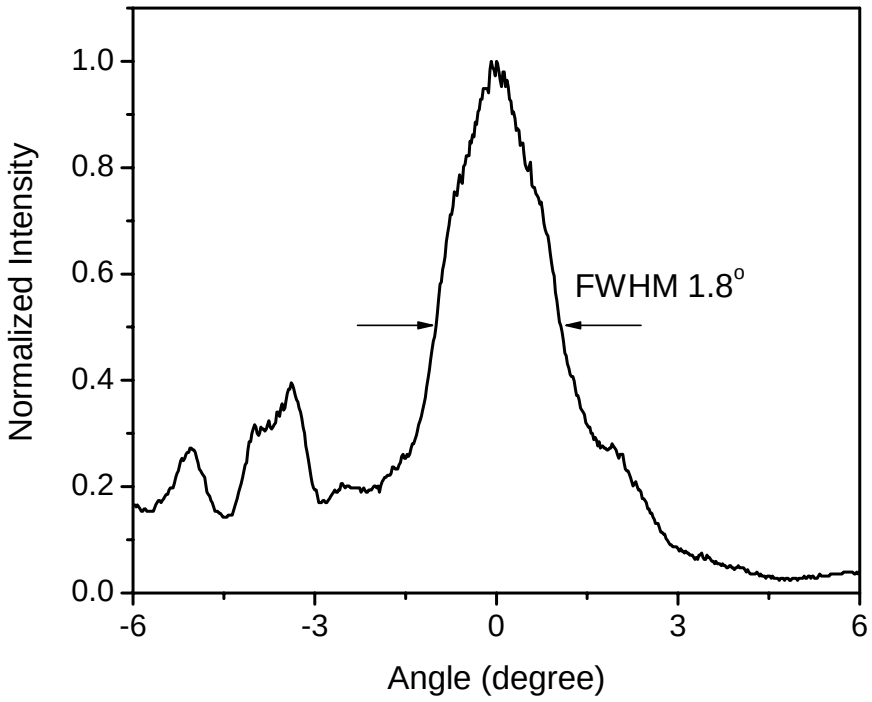

Figure 5.9: The far field profile of the PC Bragg laser at 3.5× threshold

The far field profile at 3.5× threshold is shown in Fig. 5.9. It has a 1.7× diffraction-limited divergence angle of 1.8° and two parasitic side peaks. We assume the emitting aperture of the laser is about 100 μm when we calculate the diffraction limited divergence angle of the laser [54]. Four possible reasons account for the non-diffraction-limited divergence angle and two side peaks: pulsed pump currents, current leakage outside the contact region, high order transverse modes and unwanted Bragg

reflection due to fabrication errors. Detailed discussion of the spatial modal control of the PC Bragg laser is in Section 5.5.

5.3.2 Continuous Wave operation

One important application of the PC Bragg laser is to provide high power, single mode light sources. Thus it is important to demonstrate the room temperature CW operation of the PC Bragg laser. In order to obtain the room temperature CW operation, we have to improve the performance of the laser and effectively dissipate the heat through good thermal engineering.

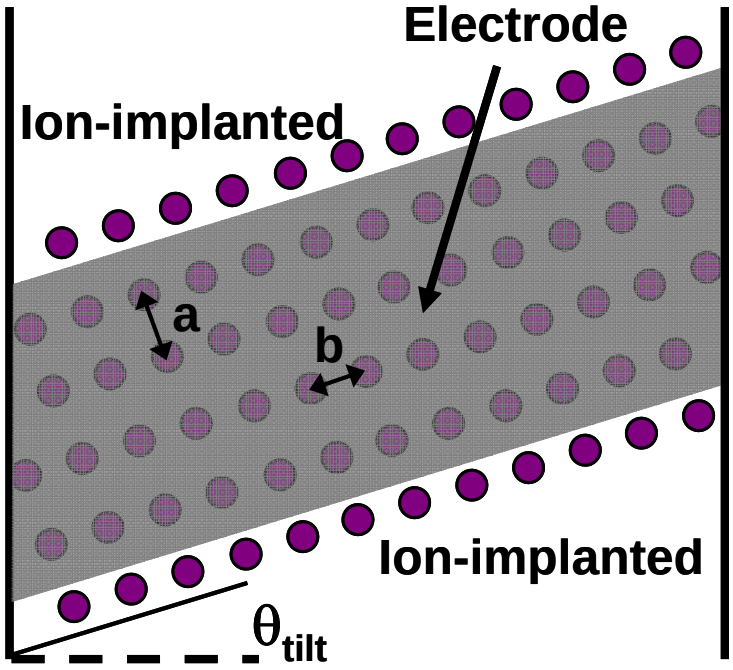

Figure 5.10: The PC Bragg laser design with the ion implantation

The first step we try is an ion implantation process. As shown in Fig. 5.10, outside the metal contact region, the lasers are implanted with protons. The implantation process can create a high resistance layer in the implanted region. There are two main reasons to use

this process: First, since the resistance is higher outside the metal contact stripe, the current is confined under the metal contact region, preventing current leakage. In this way, the laser could have a lower threshold. A low threshold is important for the room temperature CW operation; second, there is no gain outside the electrode due to the confinement of the current. Then gain-guided modes outside the laser will be suppressed. Thus this implantation process can make the performance of the laser more stable with high pump currents.

In Fig. 5.11, we compare two samples with and without the ion implantation. When there is no implantation, we can see the light outside the contact stripe, as shown in Fig. 5.11(a). This is mainly due to the current leakage. In Fig. 5.11(b), although we pump this implanted sample with higher pump currents, there is no light outside the electrode.

(a) (b)

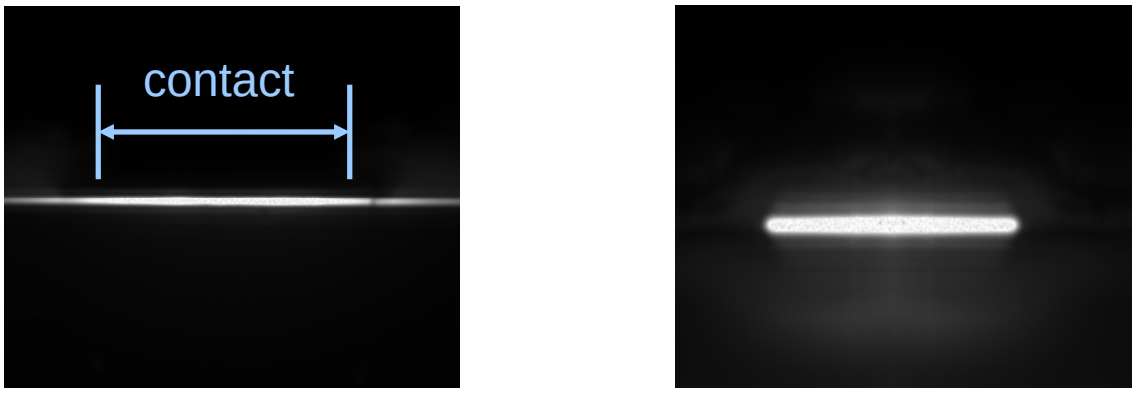

Figure 5.11: The comparison between samples (a) without the implantation and (b) with the implantation

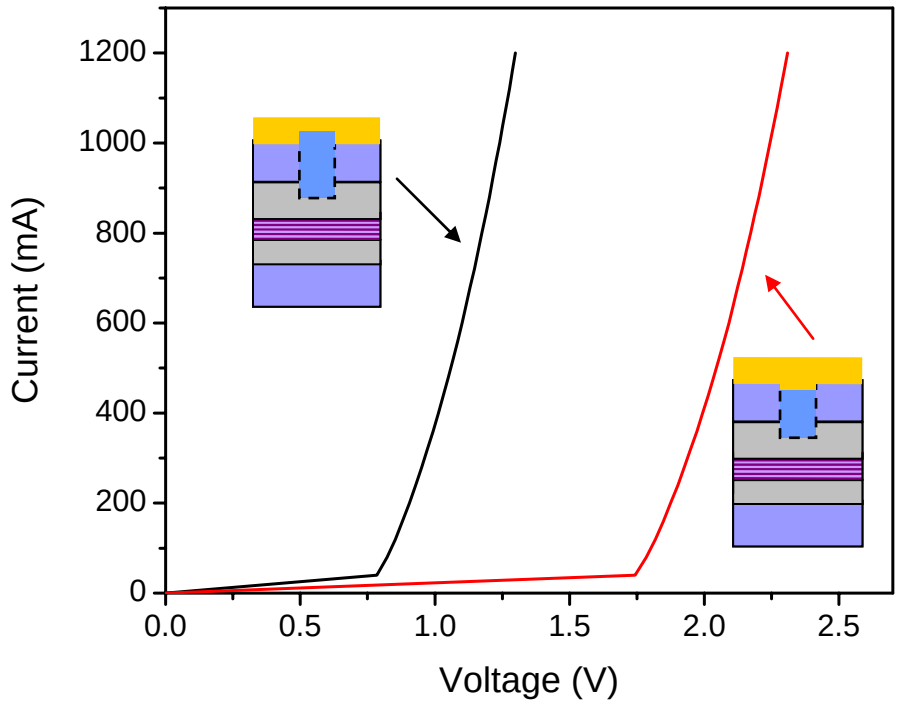

Figure 5.12: The IV curves of the PC Bragg lasers with different planarization structures

The turn-on voltage of the PC Bragg lasers depends on the relative height of the planarization polymer inside the photonic crystal to the semiconductor surface, as shown in Fig. 5.12. When the polymer inside the etched hole is higher than the semiconductor wafer surface, the turn-on voltage of the laser is much smaller. We believe this is mainly due to the surface state of the etched semiconductor. The metal layer is in direct contact with the etched semiconductor if the polymer post is lower than the wafer surface; while the metal layer only contacts with the highly doped, unetched semiconductor if the polymer post is higher. A small turn-on voltage is important for the room temperature CW operation since it reduces the heat generation a lot. Thus in our fabrication process, we intentionally make the polymer post higher then the semiconductor wafer surface, as shown in Fig 5.13.

(a)

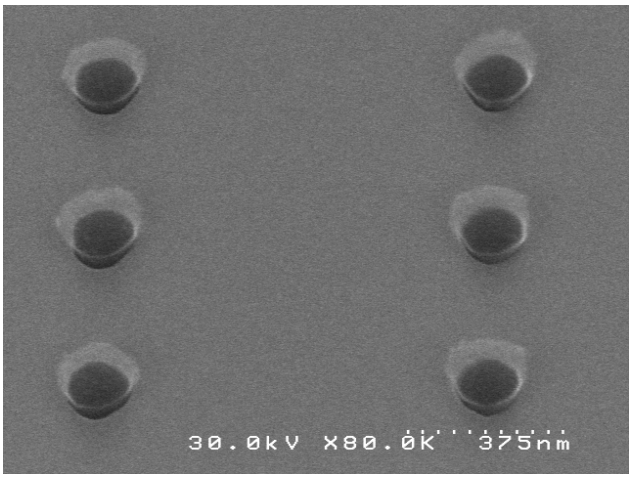

(b)

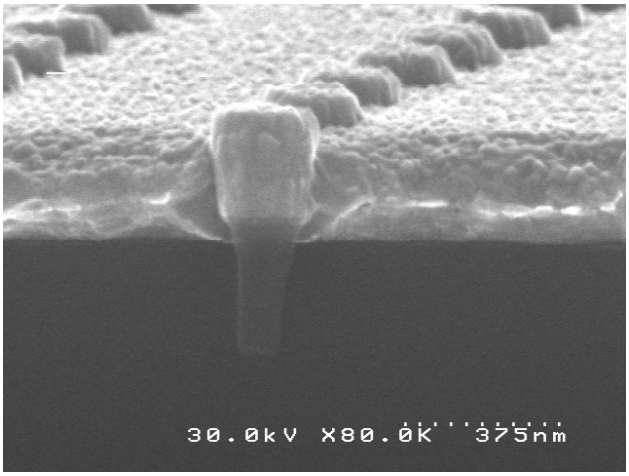

Figure 5.13: SEM images of the planarization polymer with and without the metal contact

We also try other methods to improve the thermal performance of the bonded laser, such as using thin and uniform indium solder, increasing the size of the laser die, and annealing the metal contact. By combining all these efforts, we finally obtain the first room temperature CW operation of two dimensional, single mode, edge emitting, photonic crystal Bragg lasers. These lasers break the limit of index guiding for designing edge emitting, single mode semiconductor lasers using distributed feedback structures. Our results constitute the most critical step toward broad area, single mode, high beam quality, high power semiconductor lasers with multiple available wavelengths.

We use a first order Bragg reflection for the transverse direction with a lattice constant of a = 1.04 μm and a second order Bragg reflection for the longitudinal direction with a lattice constant of b = 490 nm. The design corresponds to a resonance wavelength of 1553 nm (The effective index n_{eff} is estimated to be 3.257). The hole radius is 100 nm and the etch depth is about 400nm. The metal contact width is 100 μm and the tilt angle is 13.8° . The lasers are cleaved to lengths of about 550 μm and are p-side up bonded to a C-mount using indium solder. The C-mount is then screwed on a thermoelectric cooling (TEC) stage and the temperature is set at 13 ℃.We measure the light current (L-I) curve, spectrum, near field and far field of the laser. Despite the non-uniform intensity distribution in the near field, the far field is single lobed and diffraction limited. This proves that the photonic crystal Bragg structure can prevent the filamentation and ensure the single mode operation.

(a)

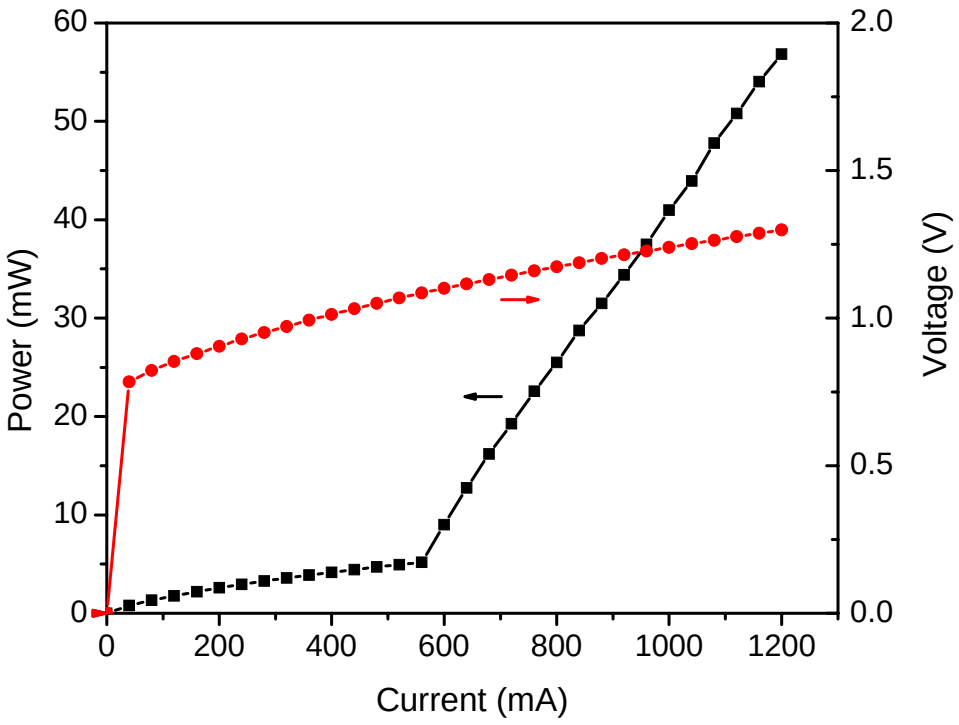

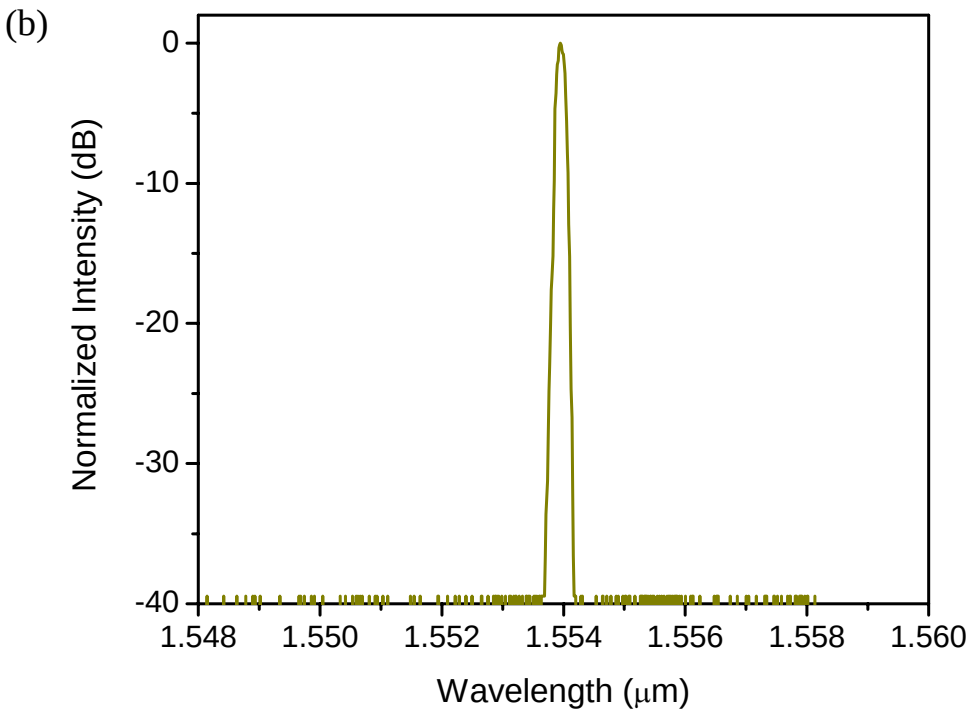

Fig. 5.14: (a) L-I and I-V curves for the photonic crystal Bragg laser. The turn-on voltage is 0.75 V and the resistance is 0.68 Ω. The threshold is 560 mA. (b) The emission spectrum at the injection current I = 1.2 A

Figure 5.14 shows the photonic crystal Bragg laser characteristics of the output power versus the input current (L-I) and the voltage versus the input current (I-V). In the I-V curve, the turn-on voltage of 0.75 V is much lower compared to our previous devices (~ 1.5 V) since we make the planarization polymer slightly higher than the wafer surface. In the L-I curve, the laser has a clear threshold at 560 mA. The device can be operated up to ~ 2.5x threshold and further increase of the pumping current leads to thermal rollover. The slope efficiency is 0.08 W/A, which is similar to the broad area lasers fabricated from the same wafer under the same test conditions. This efficiency is mainly limited by the wafer material and the thermal management. Although p-side down bonding provides much better thermal performance, we use p-side up bonding since the metal contacts are relatively thin (~ 250 nm). Figure 5.14(b) shows the emission spectrum at an injection

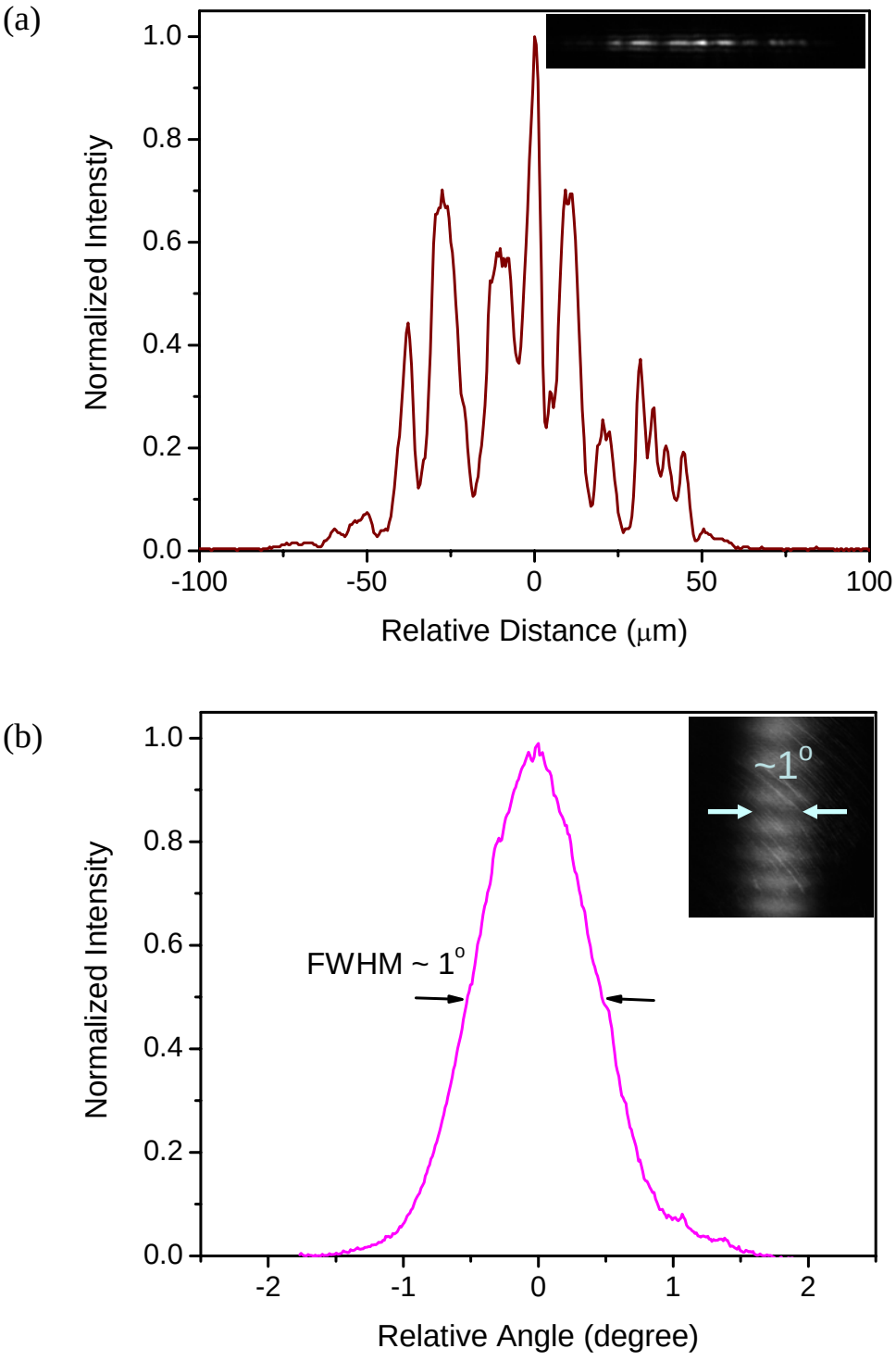

Fig. 5.15: (a) Near field and (b) far field profiles of the photonic crystal Bragg laser (I = 1.2 A). The insets are direct images captured by an infrared camera.

current of 1.2 A. The single mode operation is obtained with the side mode suppression ratio (SMSR) higher than 30 dB. The laser also maintains the single mode operation under different pumping currents.

The photonic crystal Bragg laser, by limiting the operation to a single transverse mode, prevents filamentation, which leads to spatial coherence over a large emitting aperture. This results in a single lobe diffraction limited far field with small beam divergence. Figure 5.15 shows the near field and far field profiles of the test laser when the pumping current is 1.2 A. As shown in Fig. 5.15(a), the laser has a multi-lobe near field. This is mainly due to the material gain non-uniformity over a large width (100 μm). This kind of non-uniformity generally leads to filamentation for a typical broad area laser or a ridge waveguide laser, resulting in multi-lobe far fields and big beam divergence. However, the far field of the photonic crystal Bragg laser is single lobed and possesses a small beam divergence angle of 1°, as shown in Fig. 5.15(b). (In the far field image, the fringes in the vertical direction are due to unwanted interferences in the measurement.) The emitting aperture of the laser is about 100 μm, corresponding to a theoretical diffraction limited far field FWHM width of 0.99° [54]. This shows that the photonic crystal Bragg laser can operate with a single lobe, diffraction limited far field.

5.4 Two dimensional wavelength tuning

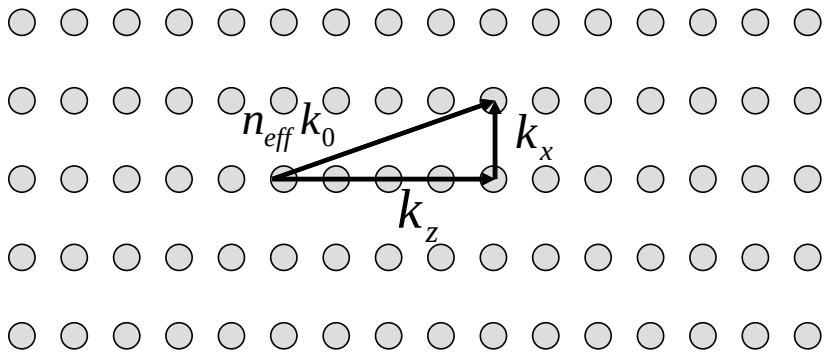

Fig. 5.16: The phase matching conditions of the PC Bragg structure

Transverse and longitudinal Bragg conditions need to be satisfied simultaneously for the PC Bragg laser

$$k_x = l\frac{\pi}{a}, k_z = m\frac{\pi}{b} \tag{5.1}$$

$$k_x^2 + k_z^2 = n_{eff}^2 k_0^2 . \tag{5.2}$$

In other words, we can tune the lasing wavelength by changing either the transverse lattice constant or the longitudinal lattice constant

$$\lambda = 2n_{eff}(l^2/a^2 + m^2/b^2)^{-1/2} . \tag{5.3}$$

We then calculate the tuning sensitivity for both the longitudinal and transverse directions from Eq. (5.3)

$$\begin{aligned} d\lambda/da &= 2n_{eff}(l^2/a^2 + j^2/b^2)^{-3/2}(l^2/a^3) \\ d\lambda/db &= 2n_{eff}(l^2/a^2 + j^2/b^2)^{-3/2}(j^2/b^3) \end{aligned} . \tag{5.4}$$

If we design the transverse wavevector much smaller than the longitudinal wavevector, the transverse wavevector only contributes a little to the lasing wavelength. In this way, the lasing wavelength changes a small amount when we change the transverse lattice constant. This means that we can finely tune the lasing wavelength with a relatively large step of the transverse lattice constant.

We first use a first order Bragg reflection (l = 1) for the transverse direction with a lattice constant of a = 1 μm and a second order Bragg reflection (j = 2) for the longitudinal direction with three different lattice constants of b = 480 nm, 490 nm and 500 nm. With the pulsed current injection, lasing is obtained for the b = 490 nm and 500 nm designs with different threshold current densities of Jth = 1.10 kA/cm2 and 1.33 kA/cm2, respectively. Figure 5.17(a) shows the optical spectra for all the three designs at the same pump current density J = 1.40 kA/cm2. While lasing is not obtained for the device with b = 480nm, the resonance peak at 1523.1 nm is evident in the spectrum.

The reason that the b = 480 nm design does not lase is due to the fact that the resonance peak wavelength for this design is far away from the peak wavelength of the gain spectrum and intrinsic losses at short wavelengths are high. Since the resonance wavelength of the 490 nm design is closer to the gain spectrum peak, the threshold of this design is lower.

In all the three designs, the experimental resonance wavelengths of 1523.1 nm, 1550.3 nm, and 1575.9 nm are close to the theoretical predictions of 1520.2 nm, 1550.1 nm and 1579.9 nm calculated from Eq. (5.3). n_{eff} is chosen to be 3.257 in the calculation and it is numerically calculated by a mode solver at the wavelength of 1550 nm. The slight difference at 1523.1 nm and 1575.9 nm is mainly due to the dispersion. Tuning of the longitudinal lattice constant leads to a lasing wavelength tuning sensitivity of 2.6, which is similar to that of regular second order DFB lasers and photonic crystal lasers with large index contrasts [57–59].

(a)

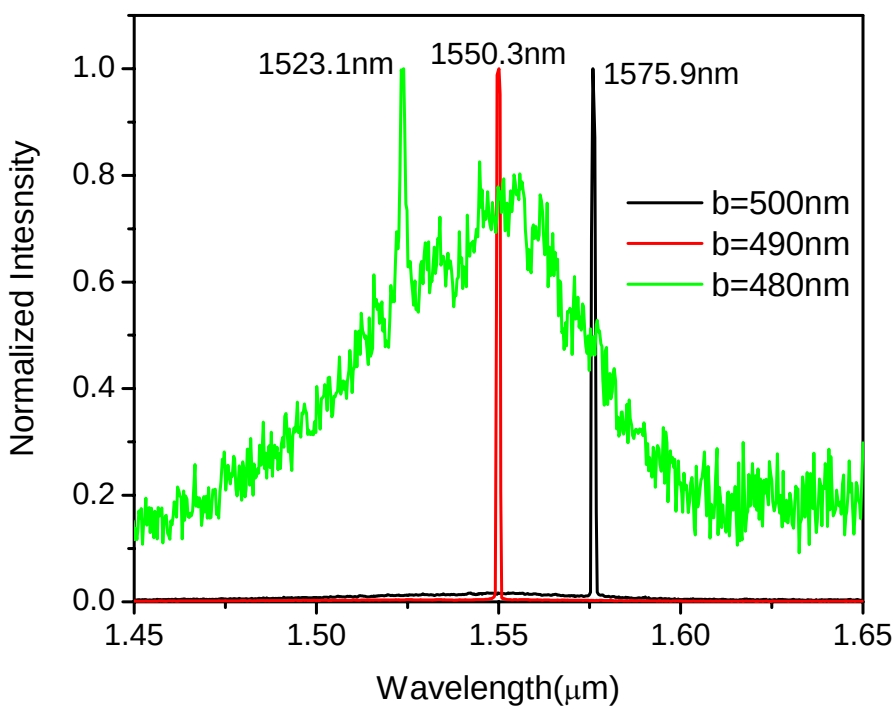

(b)

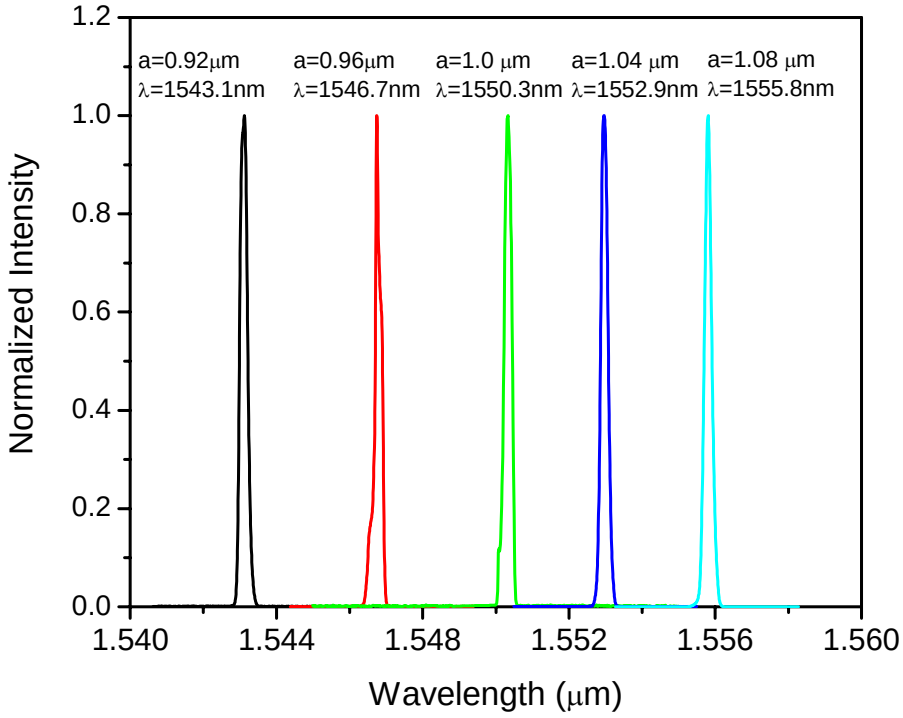

Figure 5.17: (a) Optical spectra for the lasers with the same transverse lattice constant a = 1 μm but different longitudinal lattice contants b = 480 nm, 490 nm and 500 nm at J = 1.40 kA/cm2. (b) Lasing spectra for the lasers with the same longitudinal lattice constant b = 490 nm but different transverse lattice contants a = 0.92 μm, 0.96 μm, 1.0 μm, 1.04 μm, and 1.08 μm at ~ 1.5× threshold

We then fabricate the lasers with the same longitudinal constant of b = 490 nm and five different transverse lattice constants of a = 0.92 μm, 0.96 μm, 1.0 μm, 1.04 μm, and 1.08 μm on the same chip. Other fabrication parameters are the same as the previous examples. Figure 5.17(b) shows the lasing spectra at ~ 1.5× threshold for all the five lasers. We also show the lasing wavelength as a function of the transverse lattice constant and corresponding theoretical calculations in Fig. 5.18. As the transverse lattice constant changes from 0.92 μm to 1.08 μm, the lasing wavelength shifts 12.7 nm. This corresponds to a transverse tuning sensitivity of 0.08, eighty times smaller than a regular first order DFB laser. The small tuning sensitivity is important for the accurate control of the lasing wavelength. If we only need the same control accuracy, the fabrication tolerance can be much bigger.

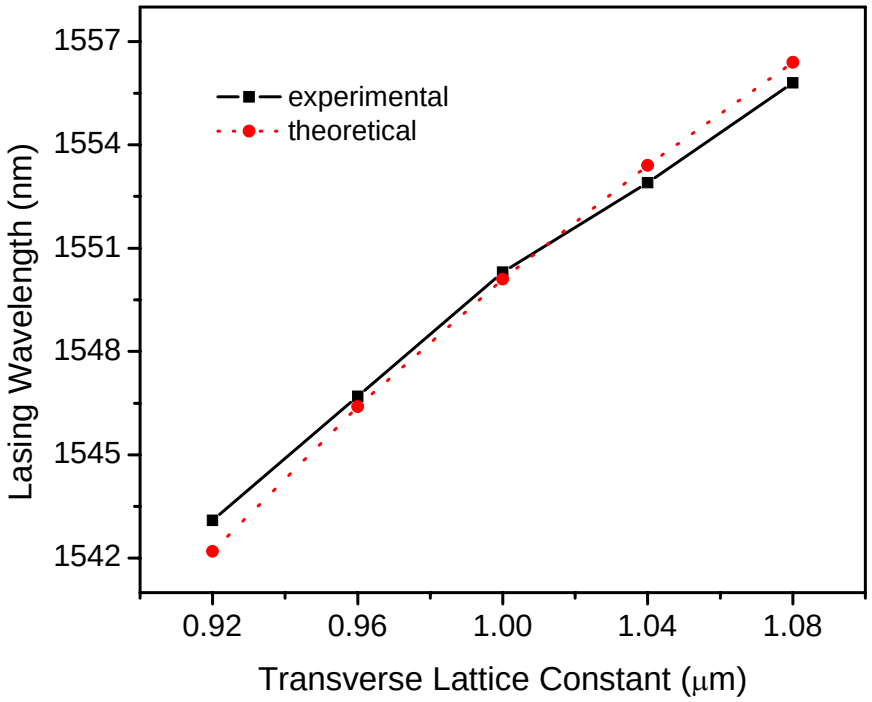

Figure 5.18: Comparison between the experimental and theoretical results for the lasing wavelength. Good match is obtained and the slight difference is mainly due to the dispersion.

5.5 Spatial modal control

To understand the spatial modal distribution of the PC Bragg laser, we first look at a simple structure—a slab waveguide. As shown in Fig. 5.19(a), the Eigen mode of the slab waveguide is the slab mode. In Fig. 5.19(b), we put down the metal contact on the slab waveguide and provide the gain to make a laser. The lasing modes are gain-guided modes. The spatial modal profiles of gain-guided modes are illustrated using the blue lines. We have the first order mode, the second order mode, and other high order modes. As we know, the Eigen mode of the photonic crystal is the Bloch mode. In Fig. 5.19(c), the blue line shows the spatial distribution of the Bloch mode. Similarly, we provide the gain for the photonic crystal structure to make a laser. The angled facet here is used to suppress

the gain-guided modes. We would expect that the lasing mode is the Bloch mode modulated by the gain-guided mode profile, as shown in Fig. 5.19(d). We also have the first order mode, the second order mode, and other high order modes. This is just our initial estimation of the spatial modal profiles of the PC Bragg laser.

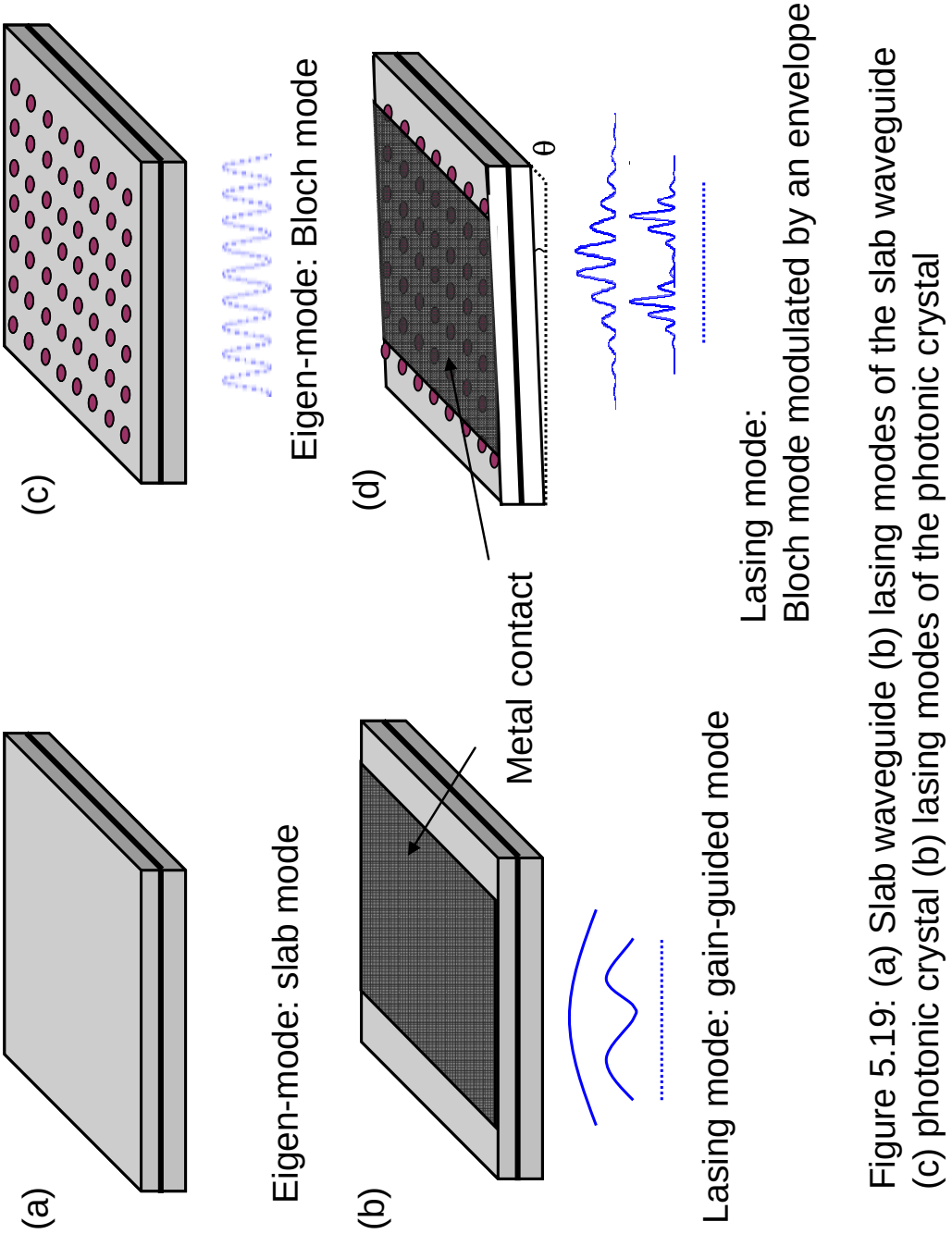

Figure 5.19: (a) Slab waveguide (b) lasing modes of the slab waveguide (c) photonic crystal (b) lasing modes of the photonic crystal

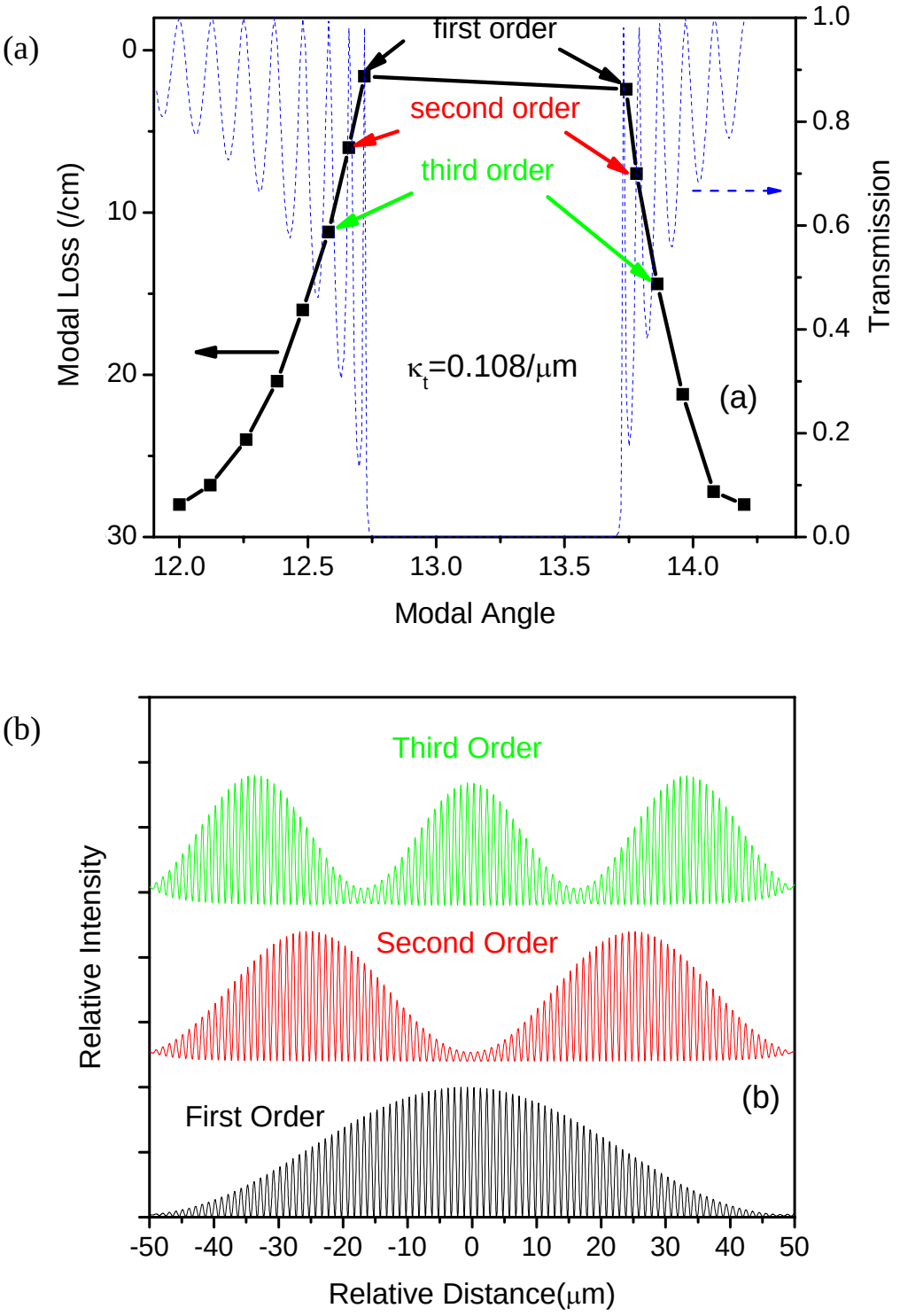

Figure 5.20: (a) Modal losses for different order TBR modes as a function of the modal angle (the solid line) and the grating transmission spectrum (the dashed line). (b) The electrical field distributions for the three lowest order TBR modes

Using the transfer matrix model in Chapter 2, we analyze different order transverse modes for the PC Bragg structure and calculate different modal profiles in the transverse direction. We define the modal angle as $\theta = \cos^{-1}(\mathrm{Re}(\beta)/(2\pi n_{eff}/\lambda))$. Figure 5.20(a) shows the modal angles and modal losses for different order TBR modes and Fig. 5.20(b) shows the electrical field distributions for the three lowest order TBR modes. The transverse coupling coefficient κ_t, which is proportional to the index contrast/the etch depth, is 0.108/μm. The transverse coupling coefficient is calculated using Eq. (3.29).

All the TBR modes in Fig. 5.20(a) are supported by the same order (first order) Bragg reflection. In Fig. 5.20(a), we also calculate the transmission spectrum of the passive grating to illustrate the origin of high order TBR modes. In Fig. 5.20(b), only the first order mode has a single lobe, near field profile and thus a single lobe. far field profile due to the angled facet design. Thus, the first order mode is the only preferred lasing mode since a single lobe. far field profile is necessary for most applications.

There are two important facts we can obtain from Fig. 5.20. First, it is clear that each TBR mode corresponds to one peak in the grating transmission spectrum. Indeed, these modes are guided by the photonic crystal structure. The finite device width (metal contact width) imposes a second transverse resonance condition and thus leads to the mode splitting. This is consistent with the fact that multiple peaks in the grating transmission spectrum are due to the finite width of the grating. Second, we define the modal loss difference between the lowest loss TBR mode and the next lowest loss TBR mode as the intermodal discrimination. A large intermodal discrimination is the key to keep the lasing in the first order mode. This can be understood as this: we provide the gain for the PC Bragg structure and when the gain compensates the loss of the first order TBR mode, the first order TBR mode starts to lase; but due to the large intermodal discrimination, the second order TBR mode will not lase. From the analysis in Chapter 2, we know the large intermodal discrimination is an advantage of using the PC Bragg structures to control the lasing modes of large-area semiconductor lasers.

However, if the etch depth of the photonic crystal, essentially the strength of the photonic crystal, is not properly designed, the intermodal discrimination could be small and this can lead to lasing in the high order transverse mode or multiple transverse modes. In Fig. 5.21, we calculate the intermodal discrimination between the first and second order TBR modes with different transverse coupling coefficients (the dashed line). We also calculate the modal loss of the first order TBR mode as a function of the transverse coupling coefficient in Fig. 5.21 (the solid line).

In Fig. 5.21, it is clear that a smaller transverse coupling coefficient corresponds to a larger intermodal discrimination against high order TBR modes. But this does not mean that we have to design the transverse coupling coefficient/the etch depth of the photonic crystal as small as possible, because the modal loss for the first order TBR mode increases as the transverse coupling coefficient decreases. This is due to the decrease of the grating reflectivity. Thus, we have to select a suitable transverse coupling coefficient (etch depth) of the photonic crystal to balance between the intermodal discrimination and the modal loss. Since the lasing threshold depends on the modal loss, this also means that there exists a trade-off between obtaining a single lobe, diffraction limited far field (ensuring the lasing in the first order mode) and reducing the threshold for a given device width. From Fig. 5.21, we expect the optimum transverse coupling coefficient to be in the range of $0.02/\mu m < \kappa_t < 0.08/\mu m$ to obtain the lasing in the first order mode combined with a relatively low threshold. Since the modal waveguiding loss is only one of a number of loss mechanisms such as scattering, absorption, and output coupling, which in total are comparable in magnitude to the modal loss, we expect a relatively small variation of the laser threshold over the range of $0.02/\mu m < \kappa_t < 0.08/\mu m$.

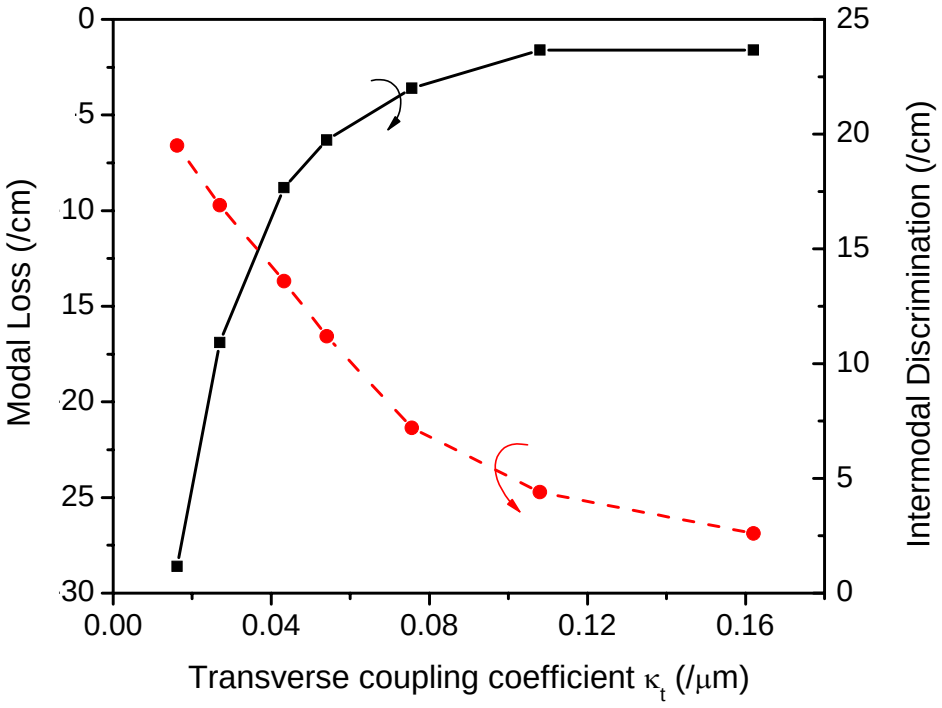

Figure 5.21: Modal losses for the first order TBR mode (the solid line) and intermodal discrimination between the first order TBR mode and second order TBR mode (the dashed line) as a function of the transverse coupling coefficient

Relying on the theoretical analysis, we fabricate the PC Bragg lasers with three different etch depths of 250 nm, 305 nm, and 430 nm. The corresponding transverse coupling coefficients are 0.012 /μm, 0.024 /μm, and 0.122 /μm, respectively. These lasers are tested at 150 K to obtain the CW lasing. Fig. 5.22 shows the L-I curve of these three lasers. The laser with etch depth of 250 nm does not lase due to the high modal loss (we injected the current up to 300 mA). The threshold currents for the lasers with etch depths of 305 nm and 430 nm are 120 mA and 58 mA, respectively. These experimental results match well with the analysis of the modal losses of the PC Bragg lasers with different transverse coupling coefficients.

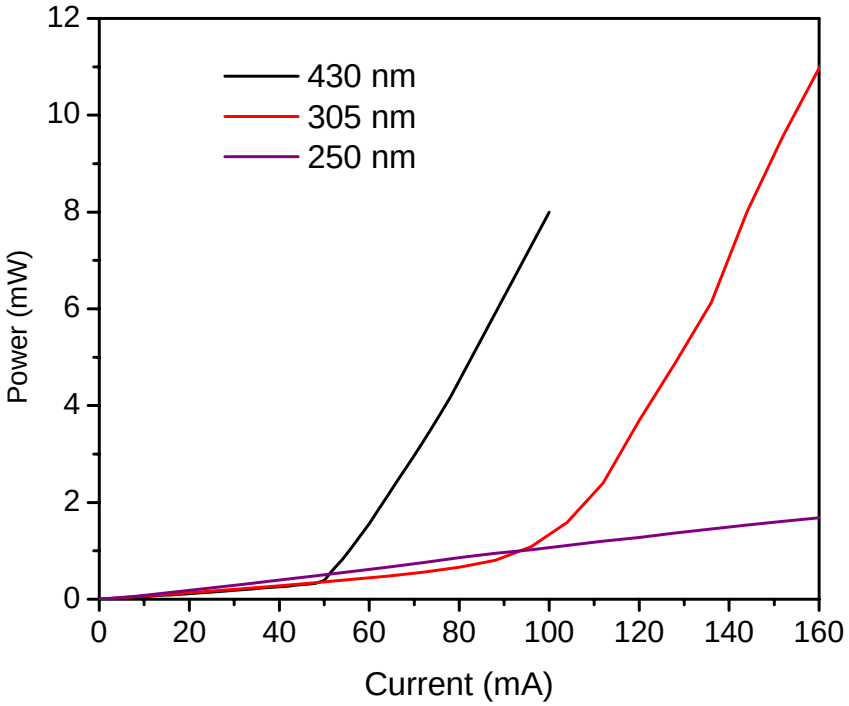

Figure 5.22: L-I curves of the three lasers with different etch depths: 250 nm, 305 nm and 430 nm

The measurement results of the spectra, near fields and far fields for the two lasers with 305 nm and 430 nm etch depths are shown in Fig. 5.23. The single mode lasing is obtained for both lasers with more than 30 dB side mode suppression ratios, as shown in Fig. 5.23(a-1) and (b-1). In Fig. 5.23 (a-2) and (a-3), the laser with 305 nm etch depth has a single lobe near field and a single lobe far field. The FWHM width of the near field profile is about 50 μm, corresponding to a theoretical diffraction limited far field FWHM width of 1.97° [54]. The measured FWHM width of the laser far field profile is about 2°, which proves that the single lobe, diffraction limited far field is obtained for this single mode laser. In Fig. 4 (b-2) and (b-3), the near field and far field of the laser with 430 nm etch depth both have three lobes, which corresponds to the lasing in the third order TBR mode. These measurement results agree well with the theoretical predictions and they prove that it is important to select a suitable etch depth (transverse coupling coefficient) to obtain the single lobe far field and maintain the single mode operation.

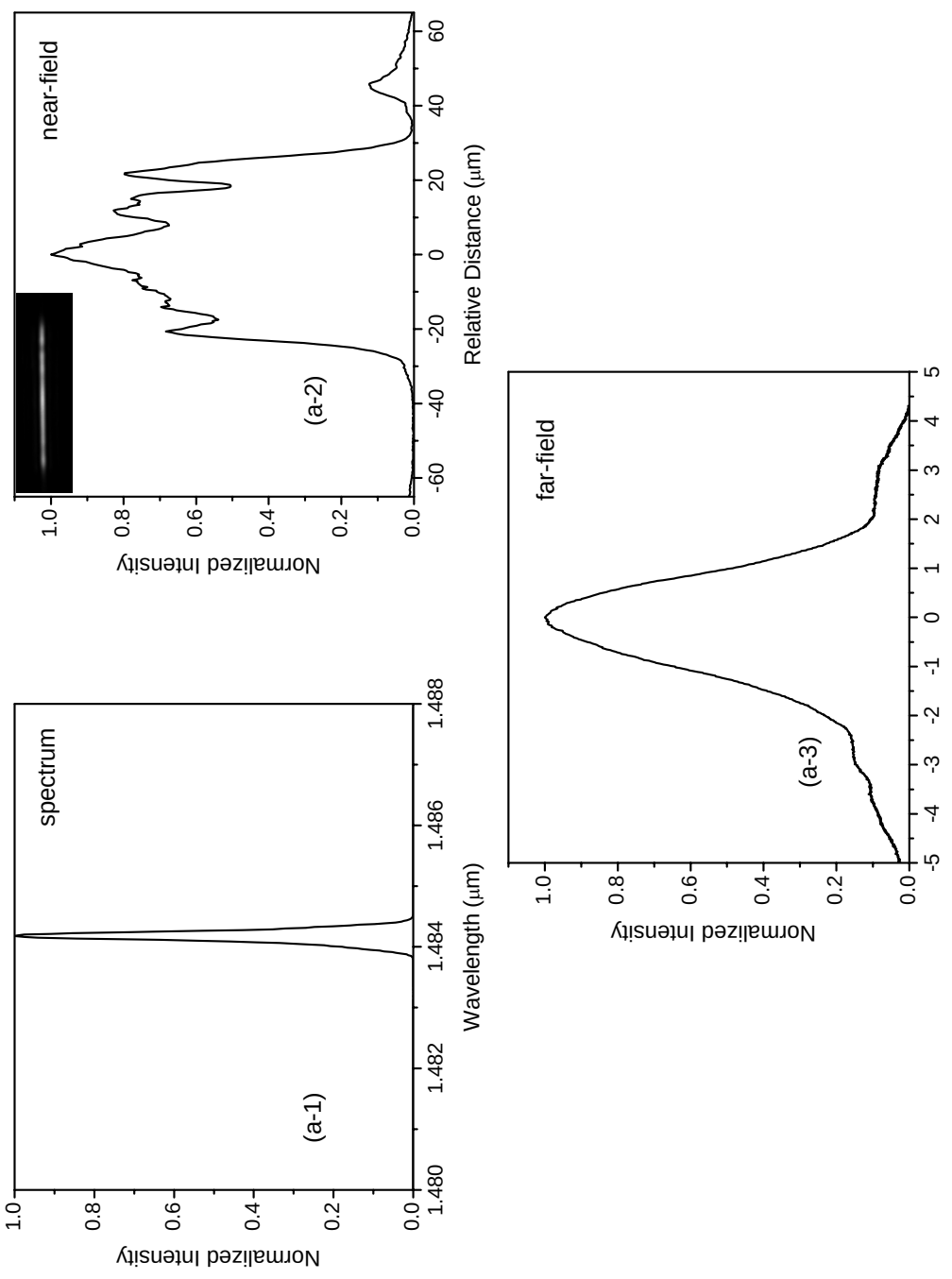

Figure 5.23: (a.1-a.3) The spectrum, near-field and far-field of the PC Bragg laser with 305nm etch depth. The inset in (a-2) is the infrared image of the laser facet.

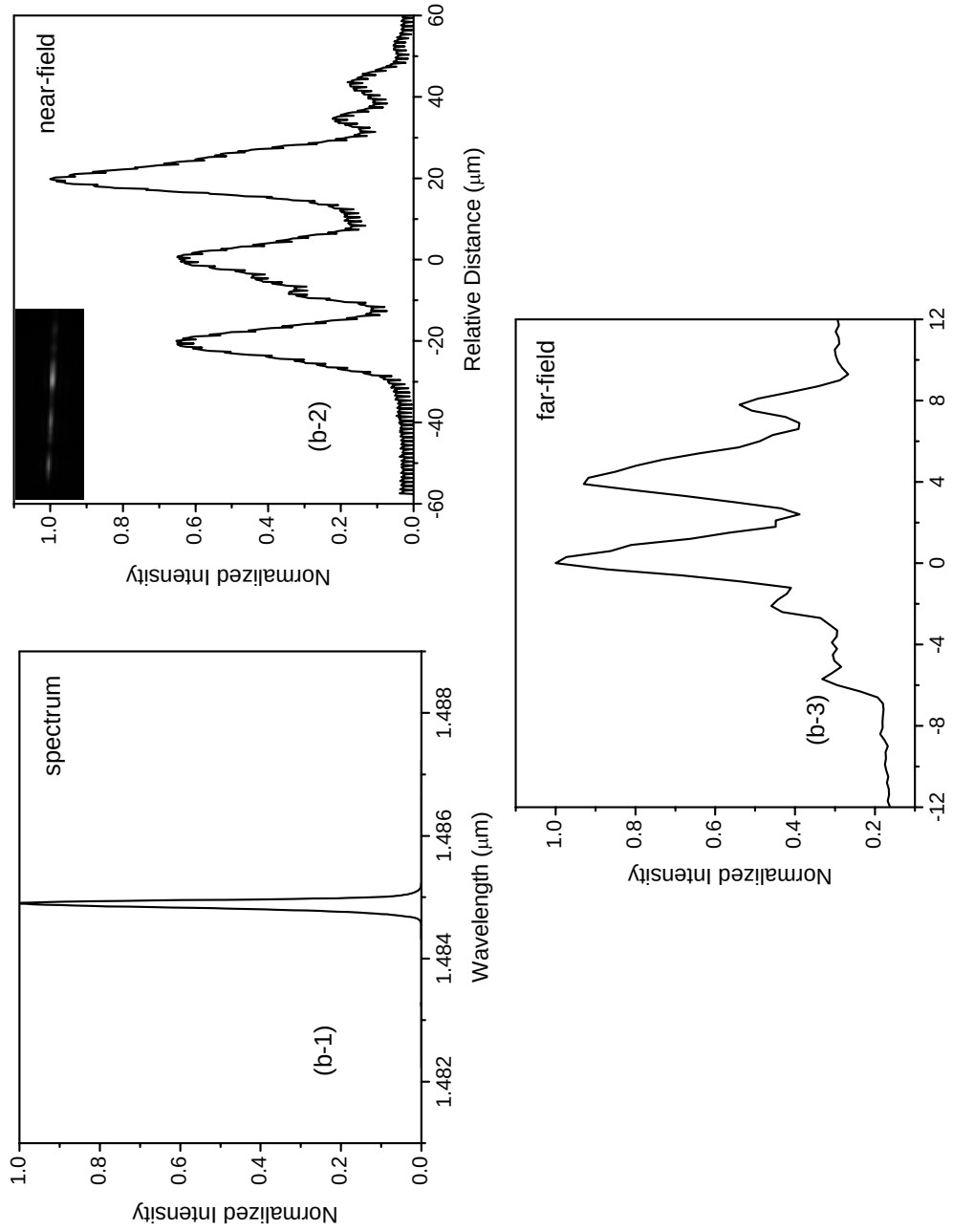

Figure 5.23: (b.1-b.3) The spectrum, near-field and far-field of the PC Bragg laser with 305nm etch depth. The inset in (b-2) is the infrared image of the laser facet.

It should be pointed that our theoretical calculations assume a uniform material gain (loss) distribution. Thus, the first order mode always has a lower threshold compared to high order modes [44]. In the fabricated devices, however if the transverse coupling coefficient is large, high order modes may possess a lower threshold depending on the actual gain distribution. This explains why the single mode lasing in the third order TBR mode is obtained for the device shown in Fig. 5.23 (b).

Chapter 6

Effective index guided photonic crystal lasers

6.1 Introduction

For more than three decades, structures with spatially periodic dielectric constants have played a crucial role in engineering the propagation and confinement of optical waves [31]. Photonic crystals, which typically refer to structures with periodicities in two or more dimensions, have garnered significant interest [60，61]. Based on the index contrast of the photonic crystal, we can divide the photonic crystal into two categories: strong index contrast photonic crystal and weak index contrast photonic crystal.

Chip scale photonic crystals with strong refractive index contrast (e.g., suspended semiconductor with air holes) can be used for the tight confinement of the optical field beyond the limits of total internal reflection. In particular, photonic crystal defect cavity lasers have been demonstrated as highly compact, coherent sources of light [11]. However, to achieve the large index contrast required by these devices, suspended membranes are often required, making these lasers structurally less robust and raising the problem of heat dissipation. In consequence, there have been relatively few reports of electrically driven photonic crystal lasers with strong index contrast [43, 62], something essential for the optoelectronic integration of photonic crystal devices.

Photonic crystals with weak refractive index contrasts can be used for the modal control of large-area semiconductor lasers. In general, these photonic crystal structures

can support two different kinds of modes: Bragg-guided and effective index-guided. For Bragg-guided modes, light is confined by Bragg reflections of the photonic crystal [63]. Since the index contrast is weak, these photonic crystals are essentially two dimensional distributed feedback structures. The idea of using two dimensional distributed feedback in lasers dates back to 1973 [64]. There are two different approaches to design two dimensional distributed feedback structures: surface emitting [65–68] and edge emitting [18, 27, 69–72]. For surface emitting lasers, light has to satisfy the Bragg conditions to diffract out of the plane. Two dimensional distributed feedback surface emitting lasers have been demonstrated in both semiconductor and polymer materials. Room temperature CW operation has been obtained for a 50 μm*50 μm single mode surface emitting semiconductor laser [67]. For edge emitting lasers, the design has to include discrimination mechanisms to suppress gain-guided modes. Photonic crystal distributed feedback structures with angled facets have been proposed to overcome this problem [69]. In the previous chapters, we report the first room temperature continuous wave (CW) operation of two dimensional distributed feedback (photonic crystal Bragg), single mode, edge emitting semiconductor lasers [72].

Effective index-guided modes are only useful for edge emitting structures. The confinement in the transverse direction is due to the index difference between the core and the effective medium formed by the periodic structure in the cladding. In photonic crystal fibers, the effective index guiding mechanism can be used to design single mode fibers with large modal areas over a wide range of wavelengths [21]. In this chapter, we describe the photonic crystal lasers with weak index contrast using the effective index-guiding mechanism. These are edge emitting devices and are well suited for planar integration. We show that it is possible to find a regime where effective index guiding and Bragg reflection strongly couple together, resulting in a hybrid mode with a large volume and reduced group velocity and thus an enhanced gain. In contrast to the photonic crystal Bragg lasers, the lasing mode frequency is away from the Brillouin zone edge of the

photonic crystal [73, 74].

6.2 Laser design and fabrication

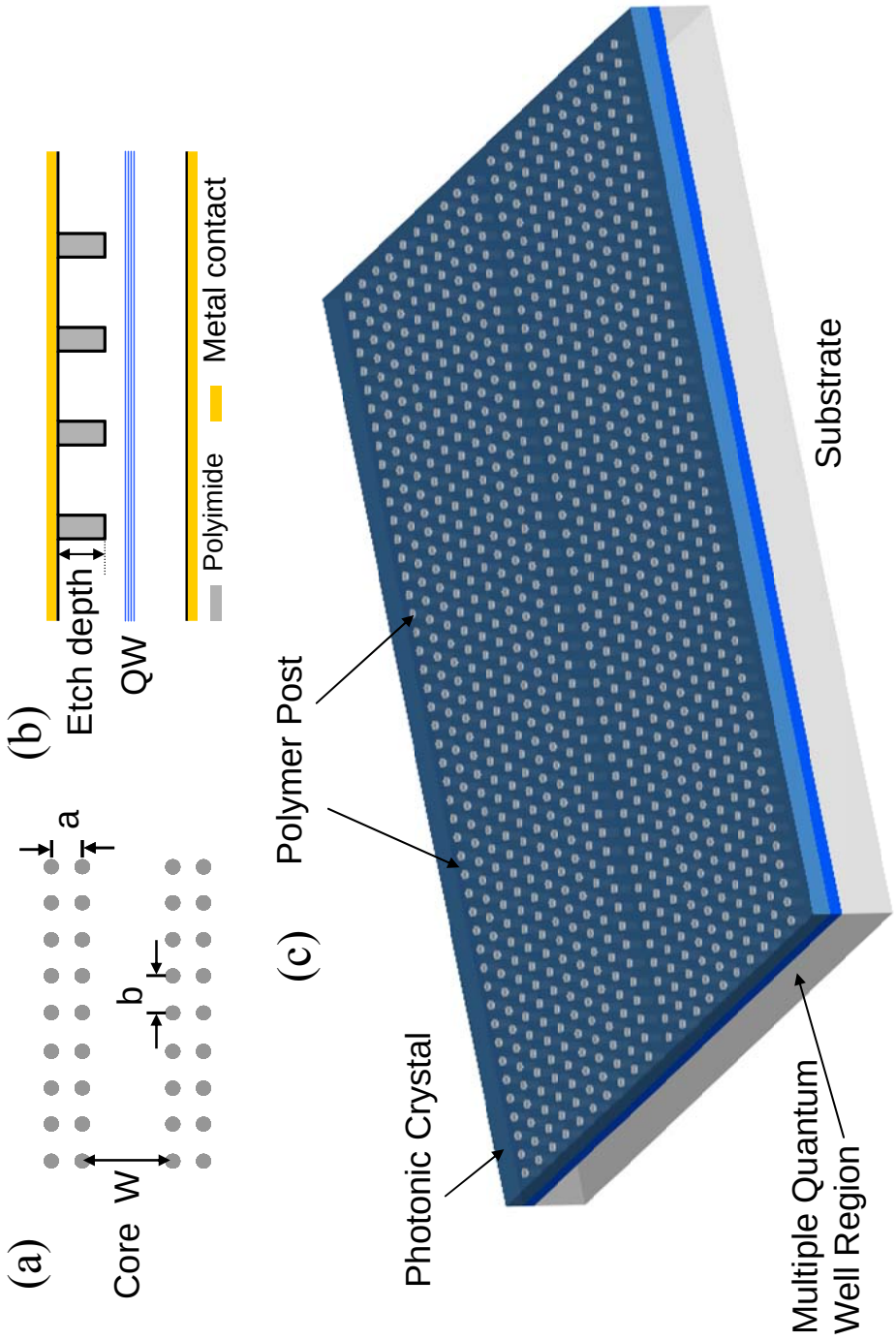

Figure 6.1: (a) a is the transverse lattice constant, b is the longitudinal lattice constant, and W is the core width. (b) The cross section structure. (c) Planar geometry of the photonic crystal lasers.

Figure 6.1 shows the schematic of our two dimensional photonic crystal laser. The surface structure consists of a rectangular lattice array of polymer filled holes with a waveguide core on the wafer surface. The active multiple-quantum-well layers are underneath the photonic crystal layer. The photonic crystal lattice consists of about 10^6 nanoscale holes each with a radius of 100 nm. Light is confined in the vertical direction by total internal reflection. The size of the electrical contact is 600 μm×160 μm (length × width). The refractive index contrast between the etched hole and unetched region is on the order of 10^{-2}, which is about two orders of magnitude smaller than conventional photonic crystals but also two orders of magnitude larger than a single mode step-index waveguide of comparable dimensions.

The fabrication procedure consists of a series of lithography, etching, planarization, and metallization steps (see also Chapter 4). First, the photonic crystal lattice is defined using electron-beam lithography and etched into the surface of the wafer. The wafer design details are in Table 3.1. The etch depth of 410 nm is chosen to obtain the desired refractive index contrast and avoid etching through the quantum wells. Next, we planarize the structure by depositing a layer of polyimide and etching it back until the device surface is exposed. The planarization is necessary to reduce the optical losses from the metallic contacts and to obtain good contact quality. The top (p-side) contact is then deposited onto the lasers by metal evaporation and lift-off. The devices are then mechanically thinned, and the n-side contact is deposited. Finally the laser bars are separated from the wafer by cleaving. Figure 6.2 shows the SEM image of a photonic crystal laser after the polyimide planarization.

We fabricate lasers with various lattice constants and core widths and test them at room temperature in pulsed operation without active cooling. Current pulses from a HP 8114A pulse generator with a duration of 100 ns and a period of 10 μs are injected to drive the lasers. The output optical signal from the device is first collected by a 50× microscope lens from the cleaved facet and is coupled into a multimode fiber. The optical spectrum is

then measured by a HP 70951B optical spectrum analyzer with a maximum resolution of 0.08 nm.

We take the near field image of the test laser diode using the same 50× microscope lens and a SUI SU640SDV InGaAs room temperature solid-state camera. We use a micrometer stage to adjust the position of the lens between the laser and the camera. We directly measure the far field pattern by putting the camera in front of the laser without any imaging optics. The distance between the laser facet and the camera sensor plane is 8 cm. The center of the acquired image represents the optical intensity at 0^o relative to the optical axis.

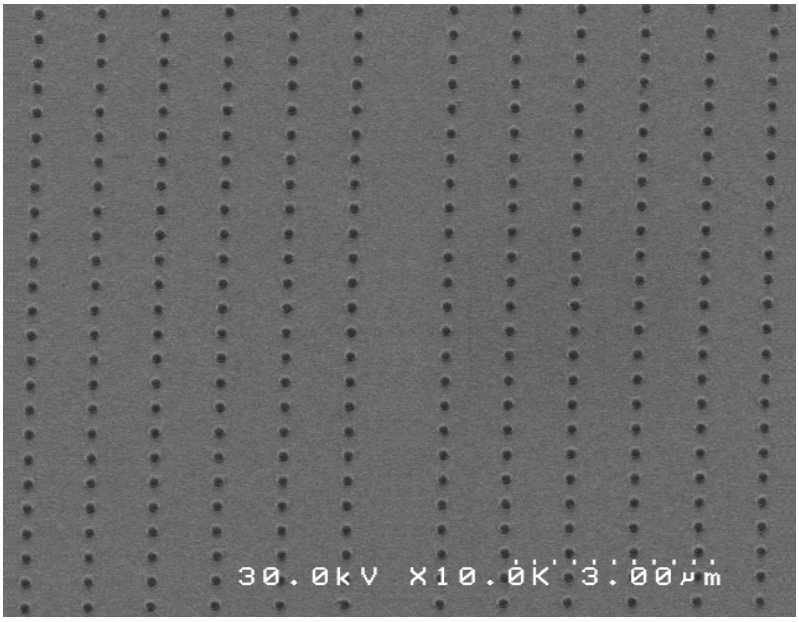

Figure 6.2: SEM image of a polymer planarized photonic crystal laser, showing rectangular array of etched holes with a waveguide core

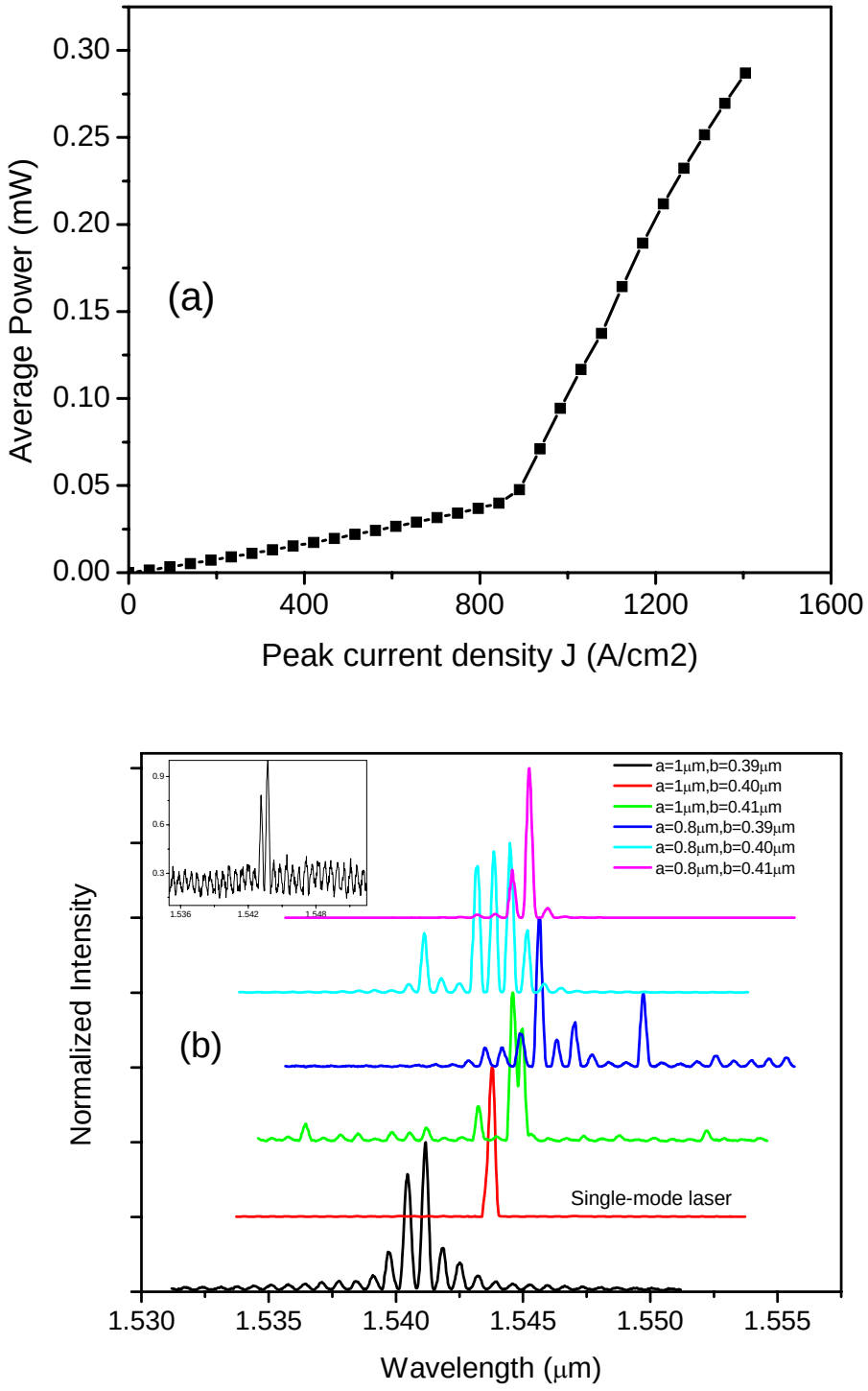

Figure 6.3: (a)The L-I curve of the structure with a = 1.0 μm and b = 400 nm. (b)Lasing spectra above the threshold (with J = 1.1 Jth) for structures with different lattice constants. Single mode operation is observed for the structure with a = 400 nm and b = 1.0 μm. The inset shows the spectrum for the single mode laser near threshold.

6.3 Measurement results

Single mode lasing, with a single peak in the spectrum, a single lobe in the near field profile, and a diffraction limited far field pattern, is achieved. First, we test a set of lasers with a transverse lattice constant, a, of 1 μm, core width of 1.5 μm, and longitudinal lattice constant, b, ranging from 400 nm to 500 nm in 20 nm steps. Single-mode lasing is observed for b = 400 nm. To explore this effect in greater detail, we next test two sets of lasers with a = 1 μm and a = 0.8 μm, with waveguide core widths of 1.5 μm and 1.2 μm, respectively. For each set of lasers, b is varied from 390 nm to 410 nm in 10 nm steps.

Figure 6.3(a) shows the light current density curve (average power verse peak current density) for the PC laser with a = 1.0 μm and b = 400 nm. It has a clear threshold around 890 A/cm2. Using the fact that light is only collected from one facet and the duty cycle of the current pulse is 0.01, we calculate a slope efficiency of 0.1 W/A (average power versus average current). Other lasers with different lattice constants have similar L-I curves with clear thresholds.

Figure 6.3(b) shows the measured optical spectra for different photonic crystal lattices. These spectra are obtained for devices on the same cleaved bar under the identical pump current density level J = 1.1 Jth. The laser with a = 1 μm and b = 400 nm shows a single peak in the lasing spectrum, while the other lasers exhibit multiple peaks. The side mode suppression ratio for the single mode laser is about 30 dB. We have also measured the single mode lasing spectrum at different positions along the emitting facets and obtained the same results. For the multimode lasers, the free spectral range (FSR) is about 0.6nm, in agreement with the laser length of 600 μm. The FSR suggests that these emission peaks arise from the longitudinal modes of the laser defined by end facets. The lasing wavelength for the single mode laser is near 1543.8 nm, while the highest lasing peaks for other two lasers with the same transverse periodicity but a different longitudinal

period are around 1541.2 nm and 1544.8 nm respectively. This indicates the lasing wavelength is determined by the lattice geometry of the photonic crystal rather than the material gain spectrum. The spectrum of the single mode laser has two very closely spaced peaks near threshold, similar to a DFB laser. As the pump current increases, the mode at the longer wavelength (1543.8 nm) dominates. The single mode behavior is maintained until J = 1.5 Jth.

Figure 6.4(a) shows near field profiles for some tested devices above the threshold. As shown in Fig. 6.4(a), the near field of the single mode laser has a clear single lobe centered at the core in the middle of the metal contact, which suggests that only one transverse mode exists. The $1/e^2$ modal width from the near field profile is about 25 μm. In contrast, the multimode lasers have multiple lobes along the cleaved facet including the lobe at the core. Multi-lobed near field profiles are always accompanied by a multi-peaked laser spectra, which indicates that more than one transverse mode can oscillate in the multimode lasers.

In addition to the single lasing peak and the single lobe near field, the single mode laser also possesses a diffraction-limited single lobe far field pattern with a divergence angle of 2.9^o. The measured far field profile for this laser is shown in Fig. 6.4(b) and it is similar to that of a large-area index-guided ridge waveguide mode. This implies effective index guiding, rather than Bragg reflection is the main waveguiding mechanism for the lasing mode.

Since the contact width is bigger than the lasing modal width, there are some tails in both the near field and far field profiles. We also expect more robust and efficient single mode output if we match the contact with the lasing modal width.

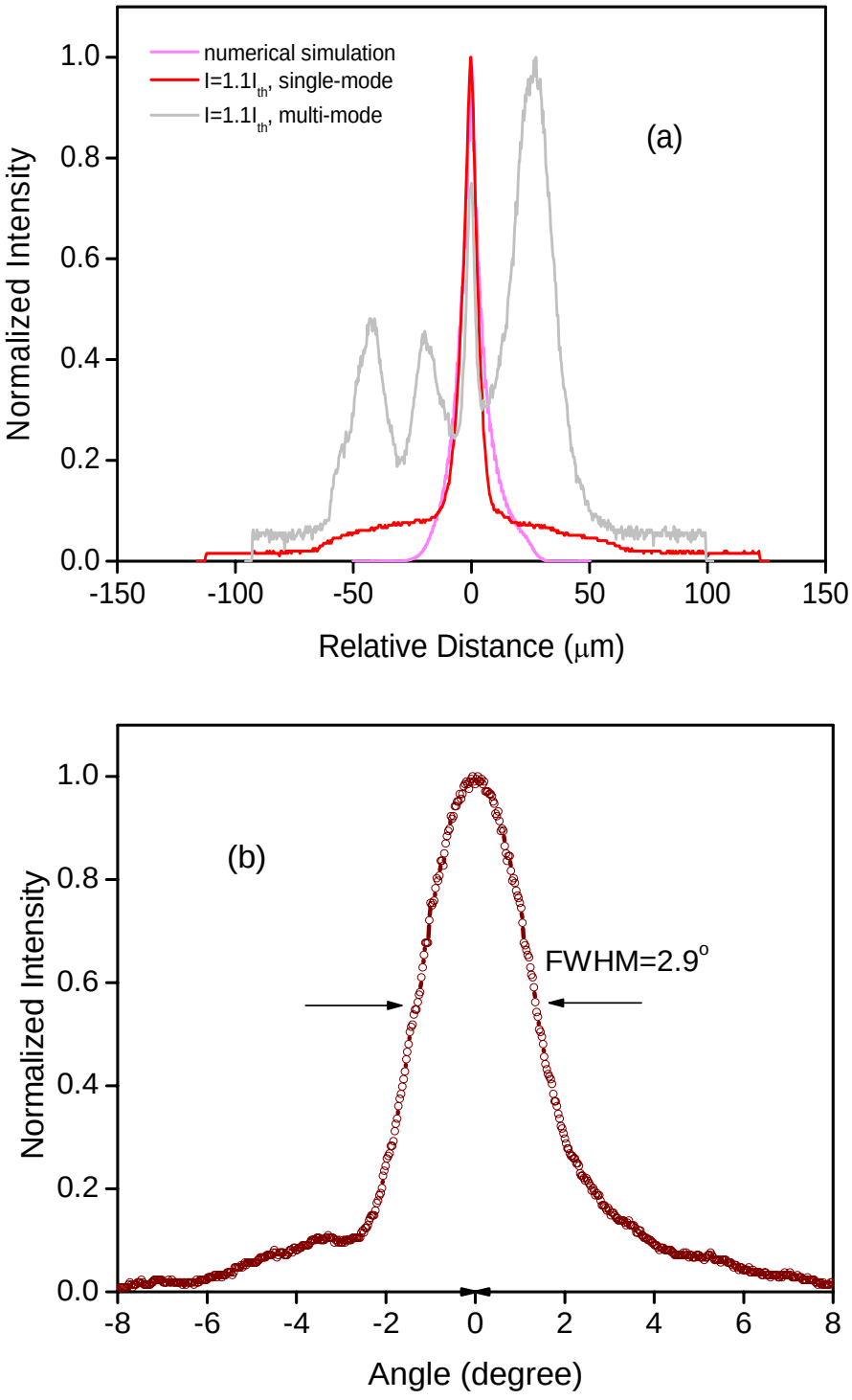

Figure 6.4: Near and far field profiles for the measured photonic crystal lasers. (a) Experimentally observed near field profiles for the single mode (red line) and a multimode structure (gray line) above threshold. For comparison, a numerically calculated near field profile is also shown (purple line). For this simulated mode, the $1/e^2$

modal width is approximately 26 μm, which matches closely with the experimentally observed value of 25 μm (b) Experimentally observed far field pattern. The far field single lobe has a FWHM of 2.9^{o}.

6.4 Numerical simulations and discussions

In general, the effective index guiding mechanism alone does not guarantee the single mode operation since all of the tested laser geometries support effective index-guided modes. To explain quantitatively the single mode lasing spectrum in Fig. 6.3, we employ a two dimensional frequency domain supercell method [75] and numerically solve for modes that are localized in the core. Our supercell consists of 50 photonic crystal unit cells on each side of the core, with the same geometry as the single mode laser. Since the multi-layer quantum well structures give preferential gain to TE modes of our system, we restrict ourselves to TE modes (H-field out-of-plane) in the simulation.

The results from the simulation are summarized in Fig. 6.5. The dispersion curve of index-guided modes is shown in Fig. 6.5(a) (red circle). It has a mini-bandgap, with details shown in the inset, in close vicinity of $b/\lambda \approx 0.2535$, which is approximately corresponding to the lasing wavelength of the single-mode laser. The black dotted lines in Fig. 5 (a) represent the band structure of the photonic crystal cladding (the photonic crystal structure without the defect core). Fig. 6.5(b) and (c) show the associated H-fields at various points of the dispersion curve. Around the mini-gap the field is delocalized (Fig. 6.5(c)) and the group velocity is reduced (Fig. 6.5(d)). It is the reduction of group velocity around the mini-bandgap that contributes to the single mode lasing observed in Fig. 6.3.

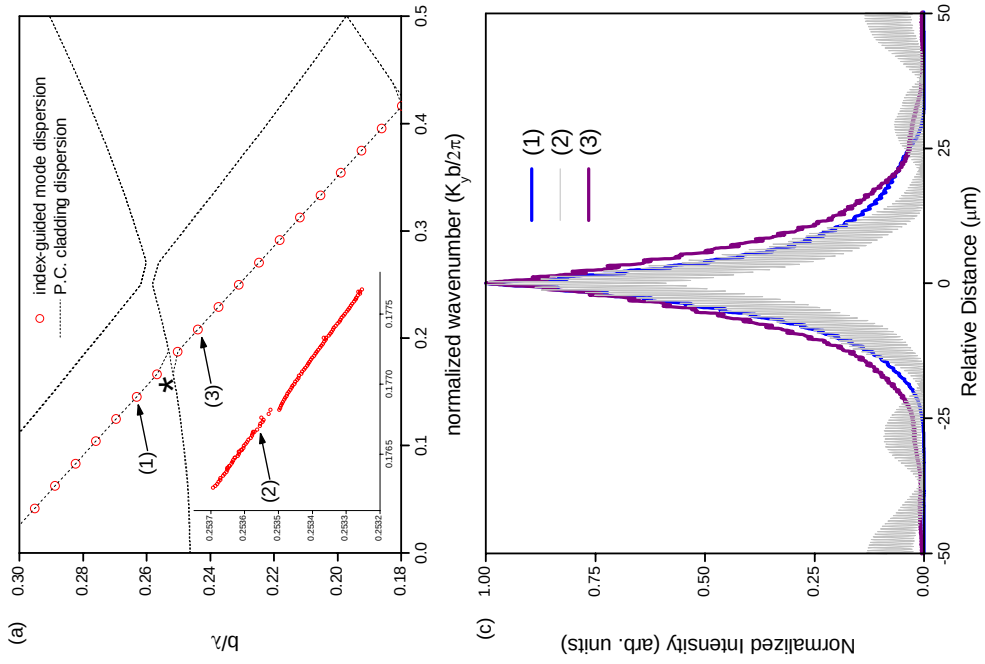

Figure 6.5: (a) Dispersion relation of effective-index guided modes (circles) superimposed on dispersion relation of the cladding photonic crystal (dotted lines). The inset shows the detail around the bandgap of the dispersion of index guided modes (b),(c)The out of plane component of the magnetic field profiles at various points of the dispersion curve (d) Group velocity of the effective index-guided modes

The origin of the mini-bandgap of the dispersion curve of index-guided modes is the coupling between effective index-guided modes and a particular order of Bragg reflection from the cladding photonic crystal. For modes away from the mini-bandgap in Fig. 6.5(a), such as at points (1) and (3), the field profiles have a main lobe slowly varying on the scale of the unit cell and thus resemble fundamental ridge waveguide modes. Within the simplest approximation, these modes can be described as plane waves with no transverse components. In the vicinity of the mini-bandgap, this plane wave is scattered by the photonic crystal cladding. The scattering process is best illustrated using the band structure of the cladding photonic crystal. At the Bloch wavenumber $K_x = 0$, the dispersion relation of the photonic crystal cladding (dotted lines in Fig. 6.5(a)) shows that near the frequency of the mini-bandgap of the photonic crystal waveguide dispersion relation, there is an anti-crossing between the photonic crystal bands. Physically, this anti-crossing corresponds to the situation where the forward/backward propagating plane wave is scattered sideways.

The mode coupling described here can be best illustrated using the band structure of a two dimensional photonic crystal with infinitesimally small index variation. The dispersion relation for an empty rectangular lattice (along the Γ−M direction, $K_x = 0$) is shown in Fig. 6.6. The band structure consists of lines with:

$$\omega(K_y) = \frac{c}{n_{avg}} \left| \left(\frac{2\pi p}{a}\right) \vec{x} + \left(\frac{2\pi q}{b} + K_y\right) \vec{y} \right| = \frac{c}{n_{avg}} \sqrt{\left(\frac{2\pi p}{a}\right)^2 + \left(\frac{2\pi q}{b} + K_y\right)^2} \,. \qquad (6.1)$$

Kx and Ky are Bloch wavenumbers. In Eq. (6.1), c is light speed in vacuum, n_{avg} is the average refractive index for the photonic crystal, a is the transverse lattice constant, b is the longitudinal lattice constant, and p and q are integers. Each line in Fig. 6.6 is associated with a particular pair of (p,q), and they represent plane waves with different wavevectors propagating inside the structure. For example, when (p,q) = (0,0) we have

$\omega = (c/n_{avg})|K_y|$, which represents plane waves propagating in the $\pm\vec{y}$ direction; when (p,q) = (±1,0) we have $\omega = (c/n_{avg})\sqrt{(2\pi/a)^2 + K_y^2}$, which represents plane waves with both forward ($\vec{y}$) and transverse ($\vec{x}$) components. At the crossing points of the dispersion relation, two (or more) modes with different wavevectors are coupled together, and phase matching conditions in space and time are satisfied simultaneously.

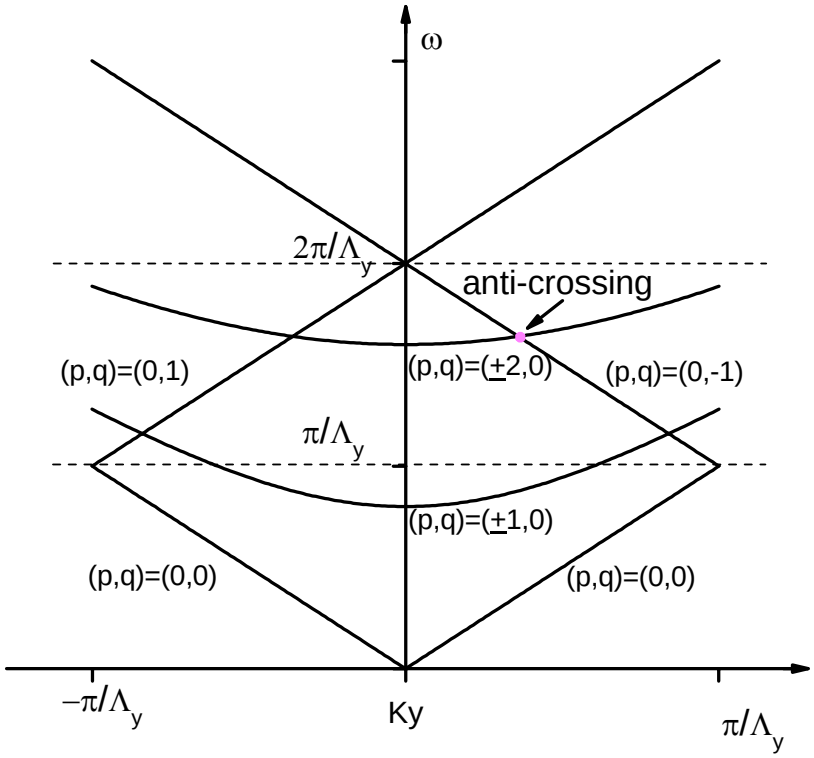

Figure 6.6: Photonic crystal dispersion relation with the Bloch wavenumber $K_x = 0$

Of particular interest is the crossing denoted by the purple dot in Fig. 6.6, where plane waves with no transverse components (with $\omega = (c/n_{avg})(2\pi/b - K_y)$) are coupled to plane waves propagating sideways (with $\omega = (c/n_{avg})\sqrt{(4\pi/a)^2 + K_y^2}$). This coupling is mediated by the lattice vectors $\vec{G} = (\pm 4\pi/a)\vec{x} \pm (2\pi/b)\vec{y}$. We illustrate this coupling

with the wavevector diagram shown in Fig. 6.7. This coupling is the origin of the mini-bandgap in Fig. 6.5(a).

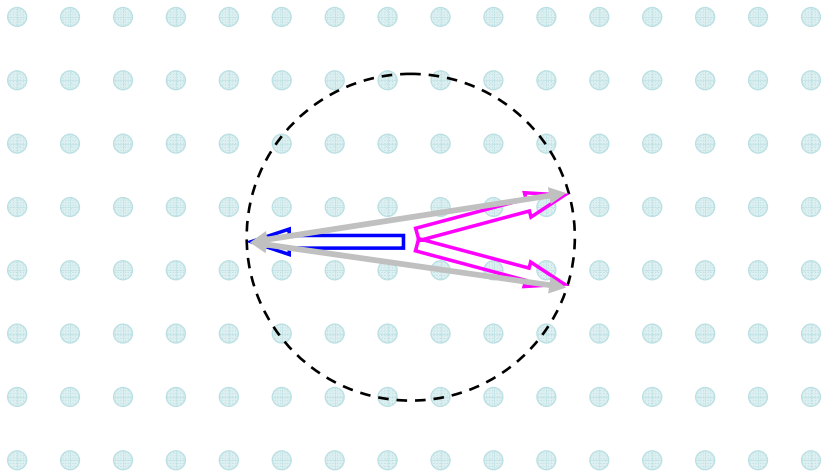

Figure 6.7: Schematic of the coupling between different wavevectors. The backward propagating field (blue arrow) is coupled to the sideways propagating fields (purple arrows) by the reciprocal lattice vectors (gray arrows).

For the structures with different geometries in Fig. 6.3, the location of the mini-gap will be at a different frequency. As a result, the reduction in group velocity will be at a frequency that is far away from the peak of the gain spectrum of the laser material. Thus, a single mode is not necessarily preferred for laser oscillation.

The feedback effect we have described differs from a conventional DFB laser. In a DFB, a grating couples a forward propagating index-guided mode couples to its backward propagating counterpart without adding any transverse component and the laser oscillates at the Brillouin zone edge ($K_y = \pi / b$). Operation at λ_0 = 1.54 μm corresponds to a photonic crystal lattice with b = 480 nm and a = 1.0 μm when the second order Bragg reflection condition in the longitudinal direction is satisfied. However, single mode lasing is not observed in that case, which may be attributed to multiple modes with similar gain at that Brillouin zone edge and the increased vertical out-of-plane loss accompanying the

second order Bragg reflection [76, 77]. To achieve single mode operation using conventional DFB feedback, first order Bragg gratings, which possess a shorter period and are thus more difficult to define lithographically, are necessary.

Chapter 7

Conclusion

In the preceding chapters, the design, fabrication, and characterization of two different photonic crystal structures based on the InGaAsP-InP material system have been described for the modal control of large-area semiconductor lasers.

First, the photonic crystal Bragg laser, in which the transverse guiding and longitudinal feedback are both provided by the Bragg reflection from two dimensional periodic structures, are described and demonstrated. In contrast to the DFB structure, the photonic crystal Bragg laser breaks the limit of index guiding, allowing for the single-mode operation of large-area semiconductor lasers.

In Chapter 2, a transfer matrix method is presented to analyze the waveguiding mechanisms in the transverse periodic structures, and is used to show that both TBR modes and SMA modes are supported by these structures. TBR modes are guided by the transverse grating and the large modal discrimination of TBR modes is ideal for the design of single mode, large-area semiconductor lasers. SMA modes include effective index-guided modes and leaky modes with small modal angles, and they always exist in large-area waveguide structures. The angled facet design is proposed to suppress the SMA modes. In Chapter 3, a longitudinal Bragg grating is incorporated into the one dimensional TBR waveguide, resulting in the photonic crystal Bragg structure, to obtain both the single transverse and the single longitudinal mode. A two dimensional coupled mode approach is used to design the photonic crystal. In Chapter 4, a versatile process for

the fabrication of the photonic crystal Bragg laser is presented. This process makes use of electron beam lithography, several reactive ion etching steps, and a planarization step to pattern the photonic crystal on an InGaAsP-InP active substrate. The electrodes are subsequently deposited, and the laser die is cleaved and bonded for test. In Chapter 5, the single mode photonic crystal Bragg laser with the single lobe, diffraction limited far field is experimentally demonstrated in both CW and pulsed conditions. The lasing wavelength is lithographically tuned by changing either the transverse or the longitudinal lattice constant. Through the transverse tuning, a wavelength tuning sensitivity of 0.08 is obtained, about 80 times smaller than a regular DFB laser.

Second, the photonic crystal laser using effective index guiding is described and demonstrated. In this structure, the confinement in the transverse direction is due to the index difference between the core and the effective medium formed by the periodic structure in the cladding. Single mode operation is achieved by combining the transverse confinement provided by an effective index-guiding mechanism with the longitudinal mode selection provided by the Bragg reflection from the photonic crystal cladding. Further investigation of the effective index guided photonic crystal laser should improve the single mode operation stability high above threshold. One possible solution is to match the width of the metal contact with the width of the optical mode.

Bibliography

[1] A. Yariv. *Optical Electronics in Modern Communications.* Oxford University Press, Inc., 5th edition, 1997.

[2] L. A. Coldren and S. W. Corzine. *Diode Lasers and Photonic Integrated Circuits*. Wiley Interscience, 1995.

[3] G. P. Agrawal and N. K. Dutta. *Long-wavelength Semiconductor Lasers*. Van Nostrand Reinhold, 1986.

[4] A. E. Siegman. *Lasers*. University Science Books, Mill Valley, 1986.

[5] M. B. Panish, H. C. Casey, S. Sumski, and P. W. Foy. Reduction of threshold current-density in GaAs-Al(x)Ga(1-x)As heterostructure lasers by separate optical and carrier confinement. *Appl. Phys. Lett.* , 22:590–591, 1973.

[6] T. Tsukada. GaAs-Ga(1-x)Al(x)As buried-heterostructure injection lasers. *J. Appl. Phys.* , 45:4899–4906, 1974.

[7] M. Nakamura and A. Yariv. Optically pumped GaAs surface laser with corrugation feedback. *Appl. Phys. Lett.* , 22:515–516, 1973.

[8] D. R. Scifres, R. D. Burnham, and W. Steier. Distributed-feedback single heterojunction GaAs diode laser. *Appl. Phys. Lett.* , 25:203–206, 1974.

[9] H. Soda, K. Iga, C. Kitahara, and Y. Suematsu. GaInAsP/InP Surface Emitting Injection Lasers. *Jpn. J. Appl. Phys.* , 18:2329–2330, 1979.

[10] K, Iga. Surface-emitting laser—Its birth and generation of new optoelectronics field. *IEEE J. Select. Topics Quantum Electron.* , 6:1201–1215, 2000

[11] O. Painter, R. K. Lee, A. Scherer, A. Yariv, J. D. O'Brien, P. D. Dapkus, and I. Kim.

Two-dimensional photonic band-gap defect mode laser. *Science,* 284:1819–1821, 1999.

[12] P. Yeh and A. Yariv. Bragg reflection waveguides. *Opt. Commun.* , 19:427–430, 1976.

[13] A. Yariv. Coupled-wave formalism for optical waveguiding by transverse Bragg reflection. *Opt. Lett.* , 27:936–938, 2002.

[14] R. J. Lang, K. D. Zurko, A. Hardy, S. Demars, A. Schoenfelder, and D. Welch. Theory of grating-confined broad-area lasers. *IEEE J. Quantum Electron.*, 34:2196–2210, 1998.

[15] S. J. Sweeney, L. J. Lyons, A. R. Adams, and D. A. Lock. Direct measurement of facet temperature up to melting point and COD in high-power 980-nm semiconductor diode lasers. *IEEE J. Select. Topics Quantum Electron.*, 9:1325–1332, 2003.

[16] A. H. Paxton and G. C. Dente. Filament formation in semiconductor-laser gain regions. *J. Appl. Phys.* , 70:2921–2925, 1991.

[17] W. Liang, Y. Xu, J. M. Choi, and A. Yariv. Engineering transverse Bragg resonance waveguides for large modal volume lasers. *Opt. Lett.* , 28:2079–2081, 2003.

[18] L. Zhu, G. A. DeRose, A. Scherer, and A. Yariv. Electrically-pumped, edge-emitting photonic crystal lasers with angled facets. *Opt. Lett.*, 32:1256-1258, 2007.

[19] P. Yeh, A. Yariv, and E. Marom. Theory of Bragg fiber. *J. Opt. Soc. Am.* , 68:1196–1201, 1978.

[20] J. C. Knight, T. A. Birks, P. S. Russell, and D. M. Atkin. All-silica single-mode optical fiber with photonic crystal cladding. *Opt. Lett.*, 21:1547–1549, 1996.

[21] T. A. Birks, J. C. Knight, and P. S. Russell. Endlessly single-mode photonic crystal fiber. *Opt. Lett.*, 22:961–963, 1997.

[22] A. Chutinan and S. Noda. Waveguides and waveguide bends in two-dimensional photonic crystal slabs. *Phys. Rev. B*, 62:4488–4492, 2000.

[23] R. F. Cregan, B. J. Mangan, J. C. Knight, T. A. Birks, P. S. Russell, P. J. Roberts, and D. C. Allan. Single-mode photonic band gap guidance of light in air. *Science*, 285:1537–1539, 1999.

[24] M. Tokushima, H. Kosaka, A. Tomita, and H. Yamada. Lightwave propagation through a 120 degrees sharply bent single-line-defect photonic crystal waveguide. *Appl. Phys. Lett.* , 76:952–954, 2000.

[25] A. Yariv, Y. Xu, and S. Mookherjea. Transverse Bragg resonance (TBR) laser amplifier. *Opt. Lett.* , 28:176–178, 2003.

[26] A. M. Sarangan, M. W. Wright, J. Marciante, and D. J. Bossert. Spectral properties of angles-grating high-power semiconductor lasers. *IEEE J. Quantum Electron.* , 35: 1220-1230, 1999.

[27] C. S. Kim, W. W. Bewley, C. L. Canedy, I. Vurgaftman, M. Kim, and J. R. Meyer. Broad-stripe near-diffraction-limited mid-infrared laser with a second-order photonic-crystal distributed feedback grating. *IEEE Photon. Tech. Lett.* , 16: 1250–1252, 2004.

[28] L. Zhu, J. M. Choi, G. A. DeRose, A. Yariv, and A. Scherer. Electrically pumped two-dimensional Bragg grating lasers. *Opt. Lett.* , 31:1863–1865 , 2006.

[29] W. W. Bewley, I. Vurgaftman, R. E. Bartolo, M. J. Jurkovic, C. L. Felix, J. R. Meyer, H. Lee, R. U. Martinelli, G. W. Tuner, and M. Manfra. Limitations to beam quality of mid-IR angled-grating distributed feedback lasers. *IEEE J. Select. Topics Quantum Electron.* , 7:96–101, 2001.

[30] K. Paschke, A. Bogatov, F. Bugge, A. E. Drakin, J. Fricke, R. Guther, A. A. Stratonnikov, H. Wenzel, and G. Erbert. Properties of ion-implanted high-power anged-grating distributed-feedback lasers. *IEEE J. Select. Topics Quantum Electron.* , 9:1172–1178, 2003.

[31] A. Yariv and P. Yeh. *Optical waves in crystals.* Wiley Interscience, 2003.

[32] H. A. Haus and C. V. Shank. Antisymmetric taper of distributed feedback lasers.

IEEE J. Quantum Electron. , 12:532–539, 1976.

[33] H. Kogelnik and C. V. Shank. Coupled-wave theory of distributed feedback lasers. *J. Appl. Phys.* , 43:2327–2335, 1971.

[34] D. Marcuse. Reflection loss of laser mode from tilted end mirror. *J. Lightwave Technol.* , 7:336–339, 1989.

[35] G. R. Fowles. *Introduction to Modern Optics*. Dover Publications, 1989.

[36] K. M. Dzurko, A. Hardy, D. R. Scifres, D. F. Welch, R. Waarts, and R. Lang, Distributed Bragg reflector ring oscillators: A large aperture source of high single-mode optical power. *IEEE J. Quantum Electron.* , 29:895–1905, 1993.

[37] C. S. Kim, W. W. Bewley, C. L. Canedy, I. Vurgaftman, M. Kim, and J. R. Meyer. Broad-stripe near-diffraction-limited mid-infrared laser with a second-order photonic-crystal distributed feedback grating. *IEEE Photon. Tech. Lett.* , 16: 1250–1252, 2004.

[38] I. Vurgaftman and J. R. Meyer. Photonic-crystal distributed-feedback quantum cascade lasers. *IEEE J. Quantum Electron.* , 38:592–602, 2002..

[39] R. E. Bartolo, W. W. Bewley, I. Vurgaftman, C. L. Felix, J. R. Meyer, and M. J. Yang. Mid-infrared angled-grating distributed-feedback laser. *Appl. Phys. Lett.* , 76:3164–3166, 2000.

[40] I. Vurgaftman, W. W. Bewley, R. E. Bartolo, C. L. Felix, M. J. Jurkovic, J. R. Meyer, M. J. Yang, H. Lee, and R. U. Martinelli. Far-field characteristics of mid-infrared angled-grating distributed-feedback lasers. *J. Appl. Phys.* , 88:6997–7005, 2000.

[41] R. E. Bartolo, W. W. Bewley, C. L. Felix, I. Vurgaftman, J. R. Lindle, J. R. Meyer, D. L. Knies, K. S. Grabowski, G.W. Turner, and M. J. Manfra. Virtual-mesa and spoiler mid-IR angled-grating distributed feedback lasers fabricated by ion bombardment. *Appl. Phys. Lett.* , 78:3394–3396, 2001.

[42] M. Loncar, T. Yoshie, A. Scherer, P. Gogna, and Y. Qiu. Low-threshold photonic crystal laser. *Appl. Phys. Lett.* , 81:2680–2682, 2002.

[43] H. G. Park, S. H. Kim, S. H. Kwon, Y. G. Ju, J. K. Yang, J. H. Baek, S. B. Kim, and Y. H. Lee. Electrically driven single-cell photonic crystal laser. *Science*, 305: 1444–1447, 2004.

[44] L. Zhu, A. Scherer, and A. Yariv. Modal gain analysis of transverse Bragg resonance waveguide lasers with and without transverse defects. *IEEE J. Quantum Electron.* , 43: 934–940, 2007.

[45] J. D. Joannopoulos, S. G.. Johnson, J. N. Winn, and R. D. Meade. *Photonic Crystals: Molding the Flow of Light.* Princeton University Press, 2008.

[46] J. K. S. Poon, L. Zhu, J. M. Choi, G. A. DeRose, A. Scherer, and A. Yariv. Active coupled-resonator optical waveguides—Part II: current injection InP-InGaAsP Fabry-Perot resonator arrays. *J. Opt. Soc. Am. B*, 24: 2389–2393, 2007

[47] G. A. DeRose, L. Zhu, J. M. Choi, J. K. S. Poon, A. Yariv, and A. Scherer. Two-dimensional Bragg grating lasers defined by electron-beam lithography. *J. Vac. Sci. Technol. B*, 24:2926–2930, 2006.

[48] H. G. Craighead, R. E. Howard, L. D. Jackel, and P. M. Mankiewich. 10-nm linewidth electron-beam lithography on GaAs. *Appl. Phys. Lett.*, 42:38–40, 1983.

[49] C.Vieu, F. Carcenac, A. Pepin, Y. Chen, M. Mejias, A. Lebib, L. Manin-Ferlazzo, L. Couraud, and H. Launois. Electron beam lithography: resolution limits and applications. *Appl. Surf. Sci.* , 78:111–117, 2000.

[50] T. H. P. Chang. Proximity effect in electron beam lithography. *J. Vac. Sci. Technol.* , 12:1271–1275, 1975.

[51] M. Parikh. Corrections to proximity effect in electron beam lithography.1. theory. *J. Appl. Phys.* , 50:4371–4377, 1979.

[52] H. Toyoda, H. Komiya, and H. Itakura. Etching characteristics of SiO2 in CHF3 gas plasma. *J. of Electron. Mat.* , 9:569–584, 1980.

[53] W. Green, J. Scheuer, G. A. DeRose, and A. Yariv. Vertically emitting annular Bragg lasers using polymer epitaxial transfer. *Appl.Phys. Lett.* , 85:3669–3671, 2004.

[54] D. Botez and D. R. Scifres. *Diode Laser Arrays.* Cambridge University Press, 1986

[55] D. Derickson. *Fiber Optic Test and Measurement.* Upper Saddle River, NJ, Prentice-Hall, 1998.

[56] J. P. Dowling, M. Scalora, M. J. Bloemer, and C. M. Bowden. The photonic band edge laser: A new approach to gain enhancement. *J. Appl. Phys.* , 75:1896–1899, 1994.

[57] M. Nakamura, H.W. Yen, A. Yariv, E. Garmire, S. Somekh, and H.L. Garvin. Laser oscillation in epitaxial GaAs waveguides with corrugation feedback. *Appl. Phys. Lett.* , 23:224–225, 1973.

[58] O. Painter, A. Husain, A. Scherer, P. T. Lee, I. Kim, J. D. O'Brien, and P. D. Dapkus. Lithographic tuning of a two-dimensional photonic crystal laser array. *IEEE Photon. Tech. Lett.* , 12:1126–1128, 2000.

[59] J. R. Cao, P. T. Lee, S. J. Choi, J. D. O'Brien, and P. D. Dapkus. Lithographic fine-tuning of vertical cavity surface emitting laser-pumped two-Dimensional photonic crystal lasers. *J. Nanosci. Nanotech.* , 2:313–315, 2002.

[60] S. John. Strong localization of photons in certain disordered dielectric superlattices. *Phys. Rev. Lett.* , 58:2486–2489, 1987.

[61] E. Yablonovitch. Inhibited spontaneous emission in solid-state physics and electronics. *Phys. Rev. Lett.* , 58:2059–2062, 1987.

[62] R. Colombelli, K. Srinivasan, M. Troccoli, O. Painter, C. F. Gmachl, D. M. Tennant, A. M. Sergent, D. L. Sivco, A. Y. Cho, and F. Capasso. Quantum cascade surface-emitting photonic crystal laser. *Science*, 302:1374–1377, 2003.

[63] J. C. Knight and P. J. Russell. New ways to guide light. *Science*, 296:276–277, 2002.

[64] S. Wang and S. Sheem. Two-dimensional distributed-feedback lasers and their applications. *Appl. Phys. Lett.* , 22:460–462, 1973.

[65] M. Imada, S. Noda, A. Chutinan, T. Tokuda, M. Murata, and G.. Sasaki. Coherent

two dimensional lasing action in surface-emitting laser with triangular lattice photonic crystal structure. *Appl. Phys. Lett.* ,75:316–318, 1999.

[66] S. Noda, M. Yokoyama, M. Imada, A. Chutinan, and M. Mochizuki. Polarization mode control of two-dimensional photonic crystal laser by unit cell structure design. *Science* , 293:1123–1125, 2001

[67] D. Ohnishi, T. Okano, M. Imada, and S. Noda. Room temperature continuous wave operation of a surface-emitting two-dimensional photonic crystal diode laser. *Opt. Express*, 12:1562–1568, 2004.

[68] M. Meier, A. Mekis, A. Dodabalapur, A. Timko, R. E. Slusher, J. D. Joannopoulos and O. Nalamasu. Laser action from two dimensional distributed feedback in photonic crystals. *Appl. Phys. Lett.* , 74:7–9, 1999.

[69] I. Vurgaftman and J.R. Meyer. Photonic-crystal distributed-feedback lasers. *Appl. Phys. Lett.* , 78:147–1477, 2001.

[70] L. Zhu, X. K. Sun, G. A. DeRose, A. Scherer, and A. Yariv. Continuous-wave operation of electrically pumped, single-mode, edge-emitting photonic crystal Bragg lasers, *Appl. Phys. Lett.* , 90: 261116, 2007.

[71] L. Zhu, X. K. Sun, G. A. DeRose, A. Scherer, and A. Yariv. Spatial modal control of two dimensional photonic crystal Bragg lasers, *Opt. Lett.* , 32: 2273–2275, 2007.

[72] L. Zhu, X. K. Sun, G. A. DeRose, A. Scherer, and A. Yariv. Room temperature continuous wave operation of single-mode, edge-emitting photonic crystal Bragg lasers, *Opt. Express*, 16:502–506, 2008.

[73] E. Schwoob, H. Benisty, C. Weisbuch, C. Cuisin, E. Derouin, O. Drisse, G. H. Duan, L. Legouezigou, O. Legouezigou, and F. Pommereau. Enhanced gain measurement at mode singularities in InP-based photonic crystal waveguides. *Opt. Express*, 8: 1569–1574, 2004.

[74] T. D. Happ, M. Kamp, A. Forchel, J .L. Gentner, and L. Goldstein. Two-dimensional photonic crystal coupled defect laser diode. *Appl. Phys. Lett.* ,

82:4–6, 2003.

[75] S. G. Johnson and J. D. Joannopoulos. Block-iterative frequency-domain methods for Maxwell's equations in a planewave basis. *Opt. Express*, 8:173–190, 2004.

[76] R. F. Kazarinov and C. H. Henry. Second-order distributed feedback lasers with mode selection provided by first-order radiation losses. *IEEE J. Quantum Electron.* , 21:144–150, 1985.

[77] H.Wenzel, R. Guther, A.M. Shams-Zadeh-Amis, and P. Biensturan. A comparative study of higher order Bragg gratings: couple-mode theory versus mode expansion modeling. *IEEE J. Quantum Electron.*, 46:64–70, 2006.